THE UNIVERSITY OF WARWICK

Library Declaration and Deposit Agreement

1. **STUDENT DETAILS**

   Yihe Lu
   1351752

2. **THESIS DEPOSIT**

   2.1 I understand that under my registration at the University, I am required to deposit my thesis with the University in BOTH hard copy and in digital format. The digital version should normally be saved as a single pdf file.

   2.2 The hard copy will be housed in the University Library. The digital version will be deposited in the Universitys Institutional Repository (WRAP). Unless otherwise indicated (see 2.3 below) this will be made openly accessible on the Internet and will be supplied to the British Library to be made available online via its Electronic Theses Online Service (EThOS) service. [At present, theses submitted for a Masters degree by Research (MA, MSc, LLM, MS or MMedSci) are not being deposited in WRAP and not being made available via EthOS. This may change in future.]

   2.3 In exceptional circumstances, the Chair of the Board of Graduate Studies may grant permission for an embargo to be placed on public access to the hard copy thesis for a limited period. It is also possible to apply separately for an embargo on the digital version. (Further information is available in the Guide to Examinations for Higher Degrees by Research.)

   2.4 (a) Hard Copy I hereby deposit a hard copy of my thesis in the University Library to be made publicly available to readers immediately.
   I agree that my thesis may be photocopied.

   (b) Digital Copy I hereby deposit a digital copy of my thesis to be held in WRAP and made available via EThOS.
   My thesis can be made publicly available online.

3. **GRANTING OF NON-EXCLUSIVE RIGHTS**
   Whether I deposit my Work personally or through an assistant or other agent, I agree to the following: Rights granted to the University of Warwick and the British Library and the user of the thesis through this agreement are non-exclusive. I retain all rights in the thesis in its present version or future versions. I agree that the institutional repository administrators and the British Library or their agents may, without changing content, digitise and migrate the thesis to any medium or format for the purpose of future preservation and accessibility.

4. **DECLARATIONS**

(a) I DECLARE THAT:

- I am the author and owner of the copyright in the thesis and/or I have the authority of the authors and owners of the copyright in the thesis to make this agreement. Reproduction of any part of this thesis for teaching or in academic or other forms of publication is subject to the normal limitations on the use of copyrighted materials and to the proper and full acknowledgement of its source.
- The digital version of the thesis I am supplying is the same version as the final, hardbound copy submitted in completion of my degree, once any minor corrections have been completed.
- I have exercised reasonable care to ensure that the thesis is original, and does not to the best of my knowledge break any UK law or other Intellectual Property Right, or contain any confidential material.
- I understand that, through the medium of the Internet, files will be available to automated agents, and may be searched and copied by, for example, text mining and plagiarism detection software.

(b) IF I HAVE AGREED (in Section 2 above) TO MAKE MY THESIS PUBLICLY AVAILABLE DIGITALLY, I ALSO DECLARE THAT:

- I grant the University of Warwick and the British Library a licence to make available on the Internet the thesis in digitised format through the Institutional Repository and through the British Library via the EThOS service.
- If my thesis does include any substantial subsidiary material owned by third-party copyright holders, I have sought and obtained permission to include it in any version of my thesis available in digital format and that this permission encompasses the rights that I have granted to the University of Warwick and to the British Library.

5. **LEGAL INFRINGEMENTS**

I understand that neither the University of Warwick nor the British Library have any obligation to take legal action on behalf of myself, or other rights holders, in the event of infringement of intellectual property rights, breach of contract or of any other right, in the thesis.

Please sign this agreement and return it to the Graduate School Office when you submit your thesis.

Student's signature: ....Date: ....

Functional Morphologies of Neuronal Dendrites

by

Yihe Lu

Thesis

Submitted to the University of Warwick

for the degree of

Doctor of Philosophy

Centre for Complexity Science

August 2018

THE UNIVERSITY OF WARWICK

Contents

Acknowledgments

First of all, I would like to express my most sincere gratitude to my supervisor, Dr. Yulia Timofeeva. I started my Ph.D. project with passionate curiosity in nature and science but mere preparation in the direction of research. She has been since then the most supportive and encouraging person. Discussions with her have always been enjoyable and pedagogic. My Ph.D. work, as well as my Ph.D. life, has benefitted considerably from her guidance and assistance.

Second, I want to thank Dr. Hugo van den Berg and Dr. Magnus Richardson, who brought me the initial insight and interest into the field of neuroscience during my postgraduate study.

Next, I would also like to thank Dr. Nicolangelo Iannella for inspiring discussions over dendritic resonance and tapering, and Dr. Tom Rother for constructive suggestions on Green's functions in general cases, and all the staff at the Centre for Complexity Science for their ardent support.

Last but not least, I am grateful to my families and friends. To borrow some words from Isaac Newton, I have been playing on the seashore, looking for pretty shells, and knowing nothing about the great ocean of truth. Nevertheless, I do know I can see stars at nights, and they are my families and friends.

Declarations

I declare this thesis is my original work, and I gratefully credit all the authors of the literature that form the foundation of my work.

The development of the method of local point matching (in Chapter 3) and its applications (in Chapter 5) are published in Biological Cybernetics, entitled as, *Response functions for electrically coupled neuronal network: a method of local point matching and its applications.*

The derivation of the framework of sum-over-trips for tapering (in Chapter 4) and its applications (in Chapter 5) have been also written up, entitled as, *Branching and tapering dendrites: a 'sum-over-trips' approach*, and submitted to PLOS Computational Biology.

Both the papers are co-authored with my supervisor, Yulia Timofeeva. She has invested great effort and time in polishing the figures and the texts.

This thesis has not been submitted to other institutions.

Abstract

Neurons are the basic units in nervous systems. They transmit electric signals along neurites and at synapses. The morphology of neurites, mainly dendrites, is famous for its anatomical diversity, and many neuronal types are named after their morphologies. As well as distributions of ion channels on cell membranes, dendritic morphologies contribute significantly to distinct behaviours of different types of neurons in signal filtration and integration (even in the situation of receiving same inputs *in vitro*).

In this thesis, we mainly address the importance of the morphology, by investigating its effects on dendritic functions via mathematical and computational approaches. By 'morphology', we consider both the global dendritic branching structure and the single dendritic tapering geometry.

We build the mathematical model of dendritic electro-physiology by generalising the classical cable theory, which allows us to study resonant membranes and tapered branches. We also develop a novel method to solve cable equations on an arbitrary branching structure that permits solutions in the form of compact algebraic expressions. We can therefore analyse a neuronal system with complex morphology theoretically and heuristically, and simulate such models accurately and efficiently.

By investigating some explicit examples that are simplified but representative, we find the tapered dendrite is better at propogating current signals than the non-tapered one, and this property is merely affected by the global morphology. We also use the method to investigate the effects of gap junctional strength and location in a neuronal circuit.

In addition, our approach is perfectly compatible with other existing methods, that makes it straightforward to recruit stochasticity and non-linearity into the framework. Future works of large neural networks could easily adapt this work to improve computational efficiency, while preserving biophysical details at the same time.

Chapter 1

Preface

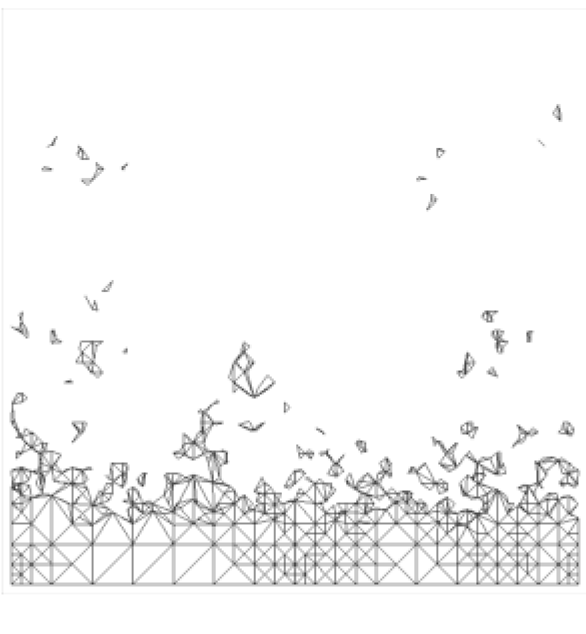

1.1 Overview of neuroscience

Amongst a few ultimate questions that we have striven to find answers, '*What makes us human?*' ranks top since, if not earlier than, the twilight of civilisations. The famous Ancient Greek aphorism '*know thyself*' could be more than a pedagogic phrase to individuals as expounded by Socrates and other philosophers, but an evidence of our curiosity in ourselves as *homo sapiens*; the phrase may actually have been adopted from an Ancient Egyptian proverb, saying '*Man, know thyself and you are going to know the gods.*' [De Lubicz, 1978].

I consider the name of our species, *homo sapiens*, or literaly *wise man*, as the first attempt in modern science to answer the question. We are different from other species, because we are superbly intelligent comparing to them, and we could be the only species being consciously aware of the fact, even though this 'fact' might merely be a belief, as we have neither a consensus on the definitions of intelligence and consciousness, nor established methods to test or prove them.

Neuroscience is our scientific frontier where we attack this very problem, as we have found the nervous system the most essential in controlling human behaviours and being responsible for intelligence and consciousness. Since there are no other ways for us to know and react to the world than 'straining' our nerves, on principle, almost every human activity can be investigated as a direct result or some indirect consequence of nervous functions.

Nonetheless, before finding our brains in a vat [Harman, 1973] or diving into a virtual reality with some neural interface [Coates, 2008], that would potentially allow our brains to connect to one another directly (perhaps via a computer), we may want to leave the study of collective human behaviours to social scientists and science fictionists, and concentrate on individual nervous systems.

However, we are still facing huge complexity since a human brain consists of approximately 10[illegible] nerve cells. The monstrous number is of the same order as that of the stars in our galaxy, but the interactions among nerve cells are not dominated by the single force of gravity. Information in the nervous system travels mainly in the form of electric signals along neurites, and often transmits from cell to cell with the assistance of chemical messengers at synapses. Both the processes occur at the level of molecules, and they are highly affected by their kinetic and electric potential energy.

An average nerve cell connects to thousands of other cells, locally and distantly, forming small neuronal circuits, large neural networks and eventually an entire nervous system. Models with biophysical details, e.g. the Blue Brain Project [Markram, 2006], trying to construct neuronal circuits bottom-up from the molecule level, are effective but inefficient; even running on some of the most powerful computers in the world, the project had simulated a column of 10^4 neocortical cells by 2008, and 100 such columns by 2011, only a tiny fraction of an average human brain.

In order to investigate larger nervous systems, models can be simplified by reducing the complexity of individual cells. For instance, a computational brain of exactly 10^{11} nerve cells with almost 10^{15} synapses was simulated on the neuronal level [Izhikevich and Edelman, 2008]. Whereas the model was able to exhibit brainwaves, it still took fifty days to produce the data of one second in the brain's real time.

An alternative approach in model reduction is to ignore the individuality of cells, and to consider a nervous system, typically a human brain, consisting of different regions. Whereas such brain regions and their connectivity are conventionally found and named in neuroanatomy, modern neuroimaging techniques have revealed the differences (and correlations) between the structural and functional connectivity. By imaging, recording and measuring dozens of brain regions (a tiny number comparing to a billion nerve cells), these models could be efficient enough for clinical usage, e.g. diagnosis of brain diseases or disorders. However, the models are phenomenological (at the macroscopic level) and thus unable to explain fundamental biological mechanisms of the brain functions.

Although neuroscience in general has to be studied with a multi-disciplinary methodology due to its complex nature at all levels, this thesis studies only structures and functions of dendrites via mathematical and computational approaches. It will be shown that the dendritic electro-physiology in a morphologically realistic nerve cell can be modelled analytically based on molecule activities, and therefore we can investigate directly how dendritic structures influence functions, and simulations can run on more realistic nerve cells but at a lower computational cost.

1.2 Outline of thesis

In §175 of Chapter I, the problems of morphology, The Principles of Biology Volume 2 [Spencer, 1884], Herbert Spencer composed, '*Everywhere structures in great measure determine functions; and everywhere functions are incessantly modifying structures.*'

Whereas the interplay between anatomy and physiology in nervous systems is evidently vital, the core question to be addressed in this thesis is '*How dendritic morphology influences electro-physiology?*', only the first half of the quote, because the time scale of any structural changes is much larger than the scale of signal propagation on dendrites considered by us.

In Chapter 2, dendritic morphology and electro-physiology are to be introduced respectively in the content of neuroscience in general. The two aspects of dendrites are then brought together and synthesised in the mathematical formalism of dendritic cable theory [Rall, 1962]. Some general results are also discussed in preparation for analytical deductions in the later chapters.

Chapter 3 and 4 are to deal with arbitrary dendritic morphology via purely mathematical approaches. Based on the path integral formulation, the framework of sum-over-trips is derived [Abbott et al., 1991] and extended [Coombes et al., 2007; Timofeeva et al., 2013], and we develop the method of local point matching. The framework of sum-over-trips is further generalised in Chapter 4 from cylindrical models to tapered ones.

Chapter 5 is the last chapter, where the analytical results are applied in special dendritic morphologies. The generalised sum-over-trips framework and the method of local point matching enable us to investigate the problems analytically with solutions in compact algebraic forms and compute the results accurately and efficiently. The morphological effects on functions can therefore be discussed on a valid quantative basis. Finally, we finish by proposing several possible future directions of the current work.

Chapter 2

Dendritic Morphology and Electro-physiology

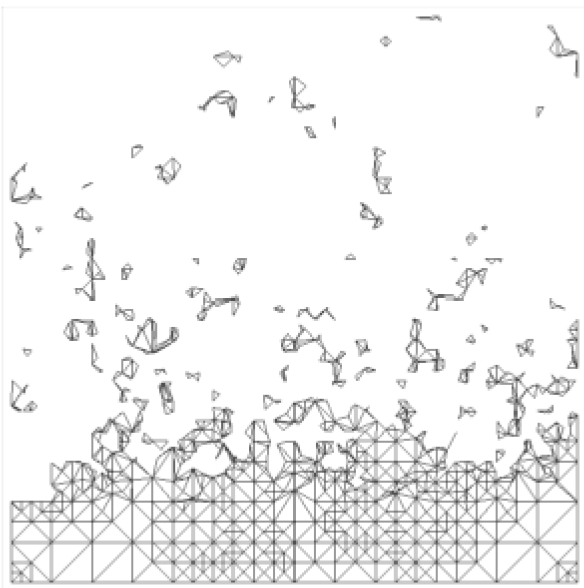

2.1 Dendritic trees

The term *dendrite*, coined by Wilhelm His in 1889 [Finger, 2001], like *neuron*, origins from Greek, which literally means *a tree*, or *a tree-like form* [Hoad, 1993]. Scientists have been fascinated by these complex structures since the exemplary work of Ramón y Cajal [1891], and the classification of neurons in accordance with their distinct morphologies is one of the most common and conventional perspectives, e.g. pyramidal neurons (see Fig. 2.1 for more examples).
Such anatomical varieties can directly lead to functional differences. Simulations have shown that, with identical ion channel types and distributions, different mor-

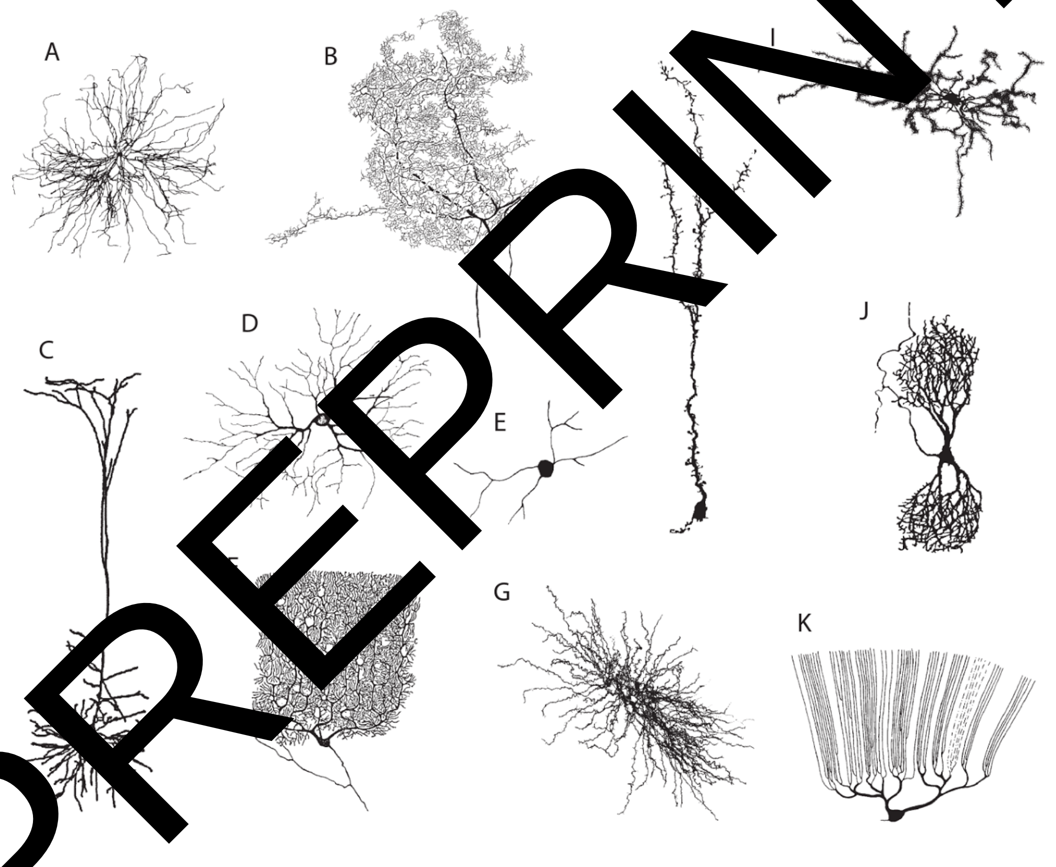

Figure 2.1: Neurons have distinct morphologies. (A) Cat motoneuron. (B) Locust mesothoracic ganglion spiking neuron. (C) Rat neocortical layer 5 pyramidal neuron. (D) Cat retinal ganglion neuron. (E) Salamander retinal amacrine neuron. (F) Human cerebellar Purkinje neuron. (G) Rat thalamic relay neuron. (H) Mouse olfactory granule neuron. (I) Rat striatal spiny projection neuron. (J) Human nucleus of Burdach neuron. (K) Fish Purkinje neuron. Modified from Mel [1994] [Stuart et al., 2016].

phologies present distinct signal propagation and firing patterns (see Fig. 2.2) [Vetter et al., 2001; Mainen and Sejnowski, 1996].
However, due to the natural heterogeneous distributions of ion channels on dendrites (and axons) [Lai and Jan, 2006], it is difficult to perform experiments with the distributions as control variables on neurons of different morphologies. Thus, in order to deepen our understanding of neuronal functions in practice, theoretical analysis, as this thesis addresses, shall help shed light on the functional properties of dendritic trees.

2.1.1 Reconstructions

To obtain the morphological model of a real neuron, *neuron tracing*, or digital neuron reconstruction, is one of the most fundamental tasks in (particularly computational) neuroscience [Ascoli, 2002], as these neuron reconstructions can be used for simulations to study neuronal electro-physiological behaviours.
Glaser and Van der Loos [1965] is one of the very first attempts on automation in neuron tracing. They used computers to interact with the microscope and to store point coordinates, which were manually indicated by a human operator. In spite of many attempts to reduce the amount of human labour [Capowski and Sedivec, 1981; Ford-Holevinski et al., 1986], neuron tracing had remained as a difficult problem (see Fig. 2.3) [Capowski, 1983, 2012] until recent years, since the fields of computer science and computer vision have advanced tremendously over the past half century [Meijering, 2010].
Instead of directly recording neuronal morphologies by some automatic process, nowadays it is preferred to acquire the entire image data first. They are initially refined by several image preprocessing techniques so that segmentation methods could be effectively applied. Segmenting usually starts with identifying soma, especially in the case when multiple neurons are present, neurites are the next to be tracked, and finally spines are detected [Meijering, 2010]. The processing order is not only heuristic but also insightful, because a successive step can utilise or even rely on the results of its proceeding steps. After measuring parameters for all segments identified, automatic tracing is thus complete but proof-editing is needed, since structural errors in reconstructions could potentially consume researchers more time to find out than conducting manual tracing [Peng et al., 2011].
One may thereby run realistic simulations on such neuron reconstructions (e.g. Fig. 2.4) [Coombes et al., 2007], or perform experiments that are nearly impossible in reality but insightful in theory [Mainen and Sejnowski, 1996; Vetter et al., 2001]. For scientists or projects that are not directly working with neuron tracing, there

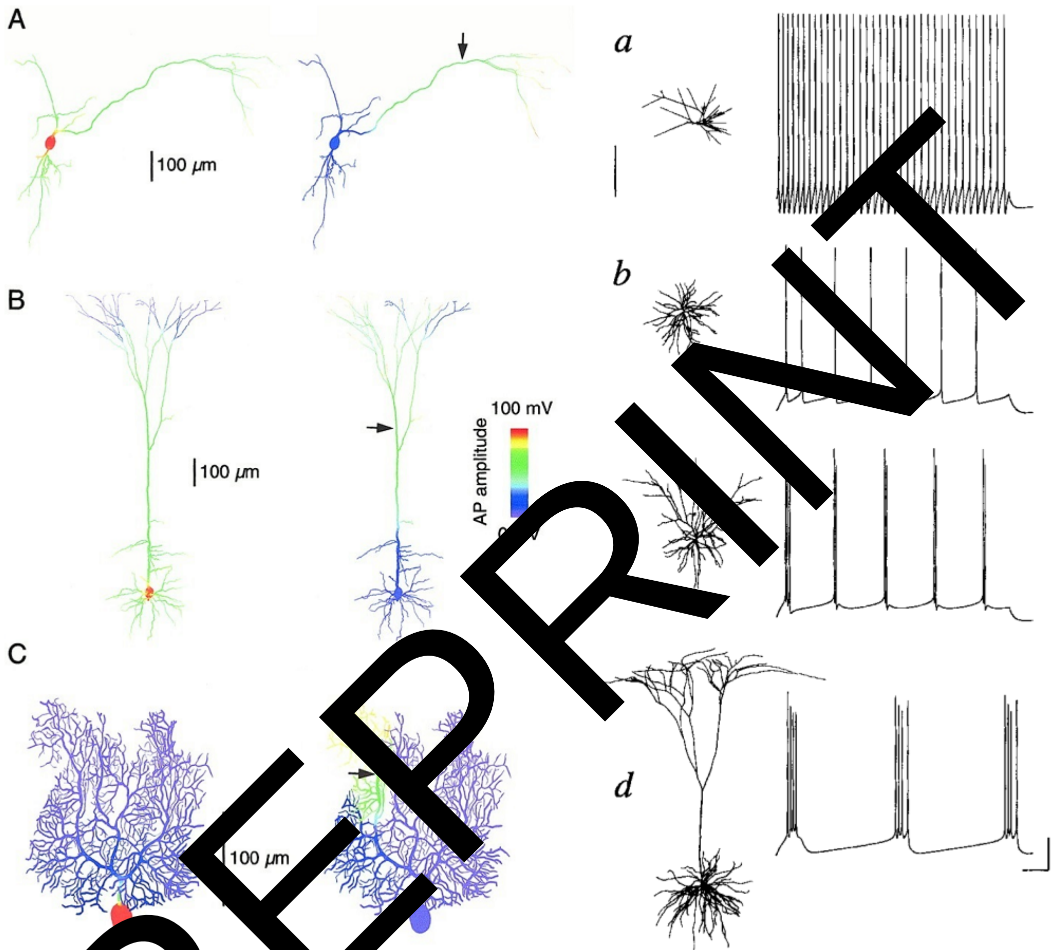

Figure 2.2: Different morphologies with identical ion channel types and distributions have distinct responses. (A) - (C): Backpropagation (from soma) and forward propogation (from location at →) of action potentials. (a) - (d): Firing patterns evoked by somatic current injection. All neurons are two-dimensional projections of three-dimensional digital reconstructions from rat brains. (A) Substantia nigra dopamine neuron. (B) Neocortical layer 5 pyramidal cell. (C) Cerebellar Purkinje cell. (a) Layer 3 aspiny stellate. (b) Layer 4 spiny stellate. (c) Layer 3 pyramid. (d) Layer 5 pyramid. (A) - (C) modified from Vetter et al. [2001] and (a) - (d) from Mainen and Sejnowski [1996].

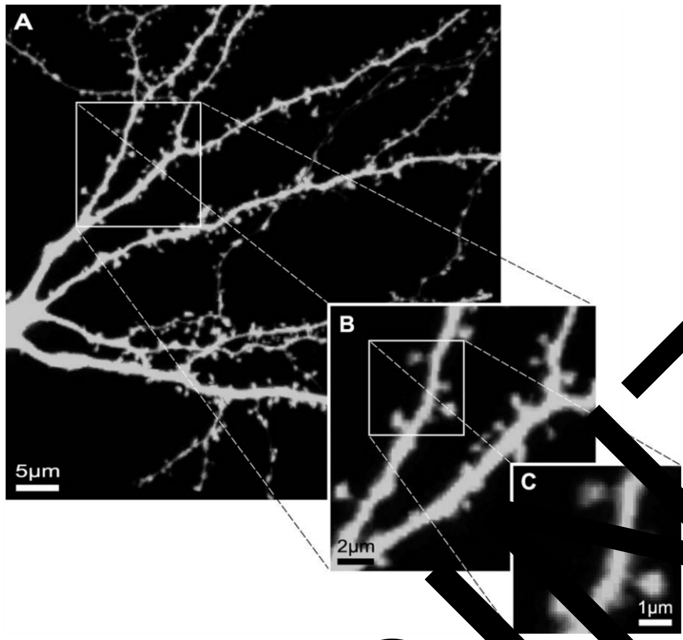

Figure 2.3: The multiscale nature of a dendritic treem: (A) from the level of a individual neuron, (B) through the level of dendritic branches and bifurcations, (C) to the level of individual spines. While this is a fairly high-quality data set, several branches are still poorly stained in (A) and spines in (C) are usually poorly imaged due to the limited resolution and can be further blurred by noises, in particular in live-cell imaging experiments, thereby causing visual ambiguities and enhancing the complexity of the problem [Meijering, 2010].

are online databases where neuron reconstructions are available for use, e.g. Neuromorpho.org [Ascoli et al., 2007].
As these three-dimensional models preserves the most comprehensive morphological information, simulations on them are computationally expensive and theoretical analysis becomes extremely difficult. Thus, there are very few but grand projects, e.g. the Blue Brain Project [Markram, 2006], that does simulate a 'large' network with such biologically detailed neurons, in the hope of shedding light on biological consciousness and intelligence. Whereas the Blue Brain Project project was running on some of the most powerful computers in the world, it had by 2011 simulated a network of 10^6 neurons, only a tiny fraction of an average human brain that consists of 10^{11} neurons.

2.1.2 Weighted graphs

In order to draw theoretical insights and to save computational expenses, reconstructed neurons (e.g. Fig. 2.4) can often be simplified as multi-compartment

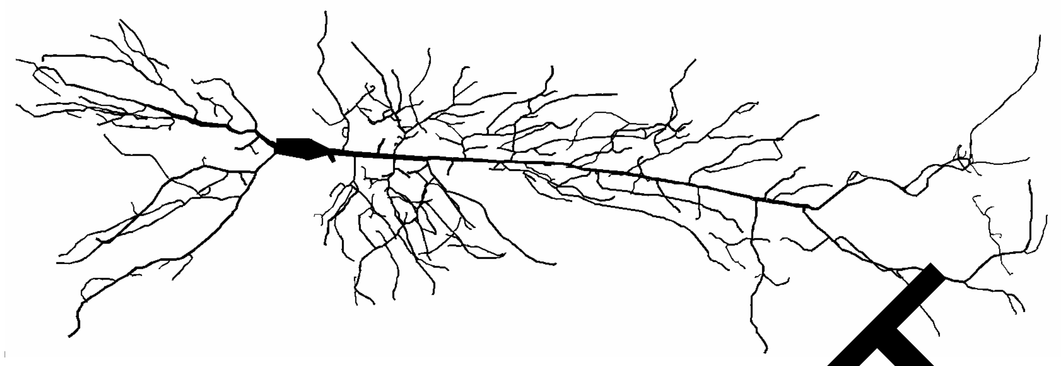

Figure 2.4: A reconstructed neuron from a rat CA1 hippocampal pyramidal cell. The reconstruction consists of 396 branches and a soma and is compartmentalised into 3961 cylindrical segments. Modified from [Coombes et al., 2007].

models that are virtually spanning in a two-dimensional plane (see Fig. 2.5).
To study such simplified models is practical and reasonable not only because we can obtain useful results given our limited computational power, but essentially due to the motility of dendritic spines, which elucidates the fact that a dendritic tree is constantly changing its shape [Bonhoeffer and Yuste, 2002]. Hence, we cannot acquire 'perfect' details of dendritic morphology by simply increasing imaging resolution or reconstruction accuracy. In addition, fixed dendritic spines are not too bad an assumption (for reasons see §2.2.3).
While schematic diagrams appear more often in theoretical works, a *dendrogram* is conventionally used to represent reconstructed neurons, which is firstly introduced by Sholl [1953] and thus known as a Sholl diagram as well (see Fig. 2.6).
Either way, a neuron is considered to be a weighted graph whose nodes are soma and branching points, connected by edges representing dendritic segments. Since such models satisfy the mathematical definition of a graph, or more specifically, a tree, one may apply graph theoretical techniques in investigating dendritic morphologies [Cherniak et al., 1999; Cuntz et al., 2007].
Since we can easily control the complexity of such a model by modifying its graph structure, representing the dendritic morphology, and parameters of nodes and edges, encoding electro-physiological properties, our invetigation will be focused on these models.

2.1.3 Point neurons

The most simplified morphology is no morphology, that is, representing a neuron by a single point. We can consider it as the most extremly reduced compartmental

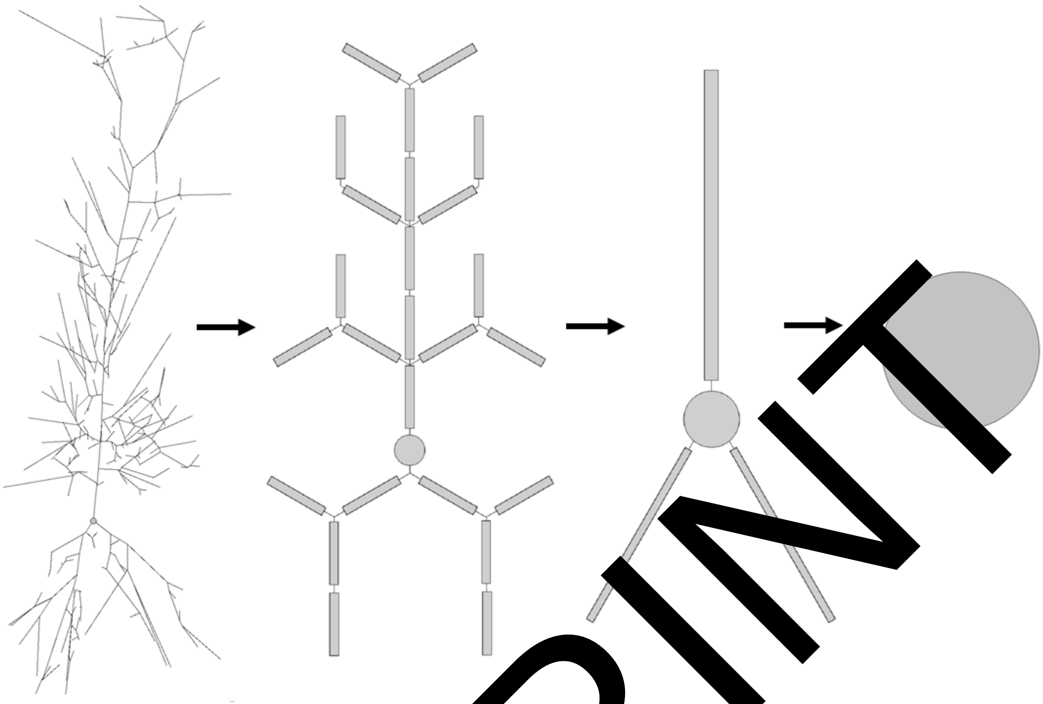

Figure 2.5: Schematic diagrams of compartmental models of the same pyramidal cell as in Fig. 2.4 (up to rotation) on different levels of morphological simplification, from 397 compartments (leftmost) down to 26, 4 and only 1 compartment (rightmost). Note that the soma (represented by a disc) in each model here is an isopotential compartment, which is not necessarily the case, e.g. the soma of the reconstruction in Fig. 2.4 consists of 3 segments.

model with only one compartment (see Fig. 2.5) or an isopotential neuron whose dendrites and axon are funtioning with instant signal propagation, communicating with other point neurons via metaphysical synapses.

Such models are useful in studying the fundamental electro-physiological models, e.g. Hodgkin-Huxley model and Integrate-and-fire model (see §2.2.2), but eclucide no insights for us since dendrites virtually do not exist. Nevertheless, we can implant the same models into dendritic trees (see §2.3).

Furthermore, it has become applicable, efficient and powerful in artificial neural networks, since the groundbreaking work of McCulloch and Pitts [1943], especially in the recent decade, e.g. the digitalisation and automation of neural tracing have largely benefited from the field of machine learning, as mentioned in §2.1.1.

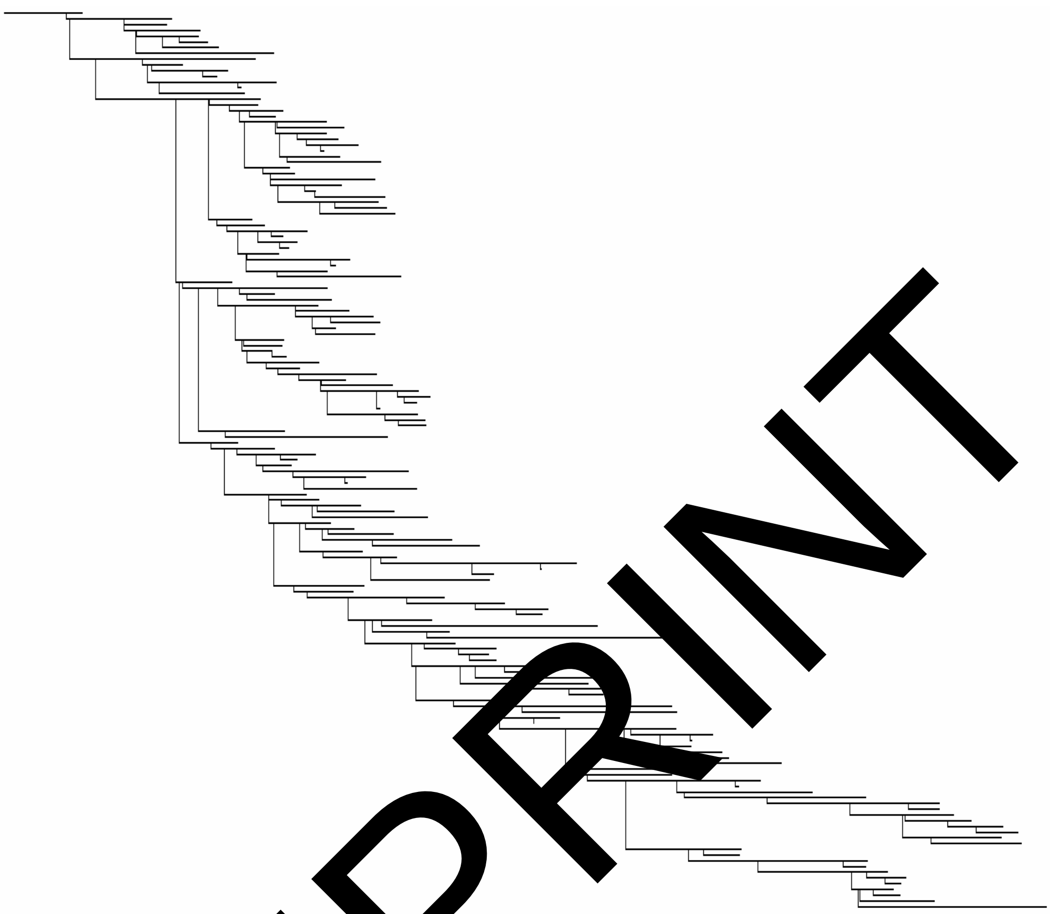

Figure 2.6: Dendrogram of the same pyramidal cell as in Fig. 2.4. Each horizontal segment represents a dendritic segment with its physical length and each vertical segment is corresponding to a branching point. Generated in NEURON [Carnevale and Hines, 2006].

2.3 Membrane potentials

Neurons are equipped with these branching structures so that they can directly communicate with more and distal cells, comparing to other types of cells. The communication is mainly excuted by *action potentials*, or *spikes*, which are essentially fast and notable changes of membrane potentials (e.g. Fig. 2.2a-d). The seemingly 'all-or-none' property of neuronal activities inspired McCulloch and Pitts [1943] to apply propositional logic in the study of neural networks, and thus an artificial neuron could be modelled by only two states, firing (occurence of spikes) and resting.

Nonetheless, membrane potentials in real neurons are not binary but continuous.

At equilibrium, they are maintained at approximately −70 mV. When a neuron is hyper- or de-polarised, the electrical change propogates along the neurites, and if the change is large enough (about +15 mV) a spike could occur, which causes the membrane potentials to rise rapidly by around 100 mV, following by an undershooting drop to approximately −90 mV in a short time (about 1 ms).

2.2.1 Electrical circuits

Cell membranes separates intracellular plasma from the extracellular environment in order to maintain homeostasis. Neuronal membranes, in particular, modulate the flows of charged ions selectively by its pore-forming membrane proteins, so that there are differences in ionic densities at the two sides of membrane, which create the membrane potentials.
Before investigating membrane potentials on a neuron with morphology, here we assume an isopotential neuron so that it is easier to study the basic electro-physiology. From now on, we start to build quantative models based on the analogy of electrical circuits (see Fig. 2.7) and thus adopt the notations and terms from control theory (see §?? for the complete list).

Capacitors: lipid bilayer

The cell membrane is a lipid bilayer, which prevents ions at the both sides moving freely. Hence, it behaves as a capacitor, that is, it can be charged up by an injection of a current I_m (generally varying with respect to time t) into the plasma, or mathematically,

$$I_m(t) = C_m A_m \frac{\partial V}{\partial t}, \tag{2.1}$$

where C_m is the capacitance per unit area, A_m is the surface area of the membrane, and the membrane potential V is the difference between extra- and intra-cellular potentials. Note that extra-cellular potentials are often assumed zero, which makes intra-cellular potentials equal to membrane potentials.

Resistors: leakage channels

However, the lipid bilayer of the cell membrane is not perfectly dielectric, and at the same time there are *leakage* ion channels that allow selective ionic species to travel across the membrane. Together they permit the leakage current, which can be written as,

$$I_l(t) = \sum_k g_l^k A_m (V - E_l^k), \tag{2.2}$$

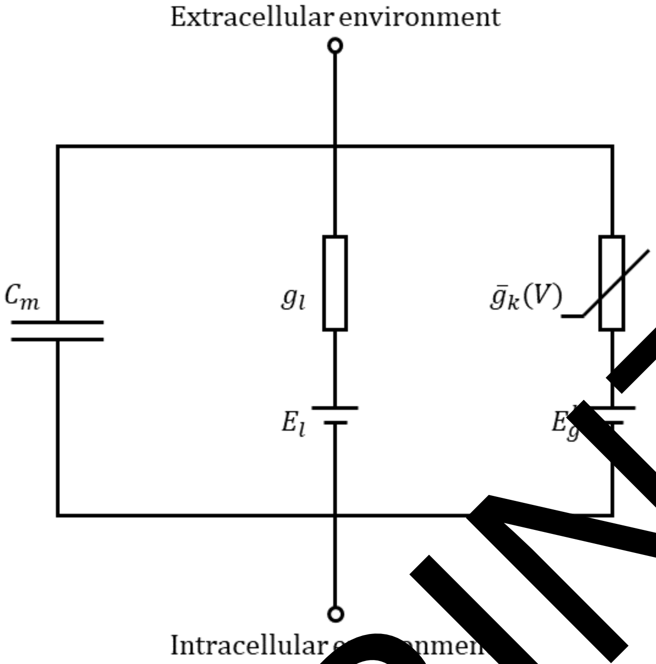

Figure 2.7: A circuit diagram of a general conductance-based model. The membrane potential V is the voltage difference between the intra- and extra-cellular potentials, which is measured at the lipid bilayer, represented by a capacitor. The membrane leakage is analogous to the series circuit of a resistor g_l and a battery E_l, and a voltage-gated ion channel is the series circuit of a non-linear voltage-dependent conductor and a battery E_g. If the ionic species of k are not of a single type, we can extend the model by adding similar series of conductors and batteries as parrallel circuits onto the circuit diagram.

where g_l^k is the leakage conductance per unit area and E_l^k is the reversal potential of ionic species k. Note that actually most of leakage channels behave as rectifiers, that is, they conduct better in one fixed direction than the other, since membrane potentials are negative for most of the time, it is convenient to assume the leakage channels as resistors.

Since both g_l^k and E_l^k are constants predetermined by the ionic species k, we can therefore rewrite the leakage current in a simpler form,

$$I_l(t) = g_l A_m (V - E_l), \tag{2.3}$$

where

$$g_l = \sum_k g_l^k,$$

is the total leakage conductance per unit area, and

$$E_l = \frac{\sum_k g_l^k E_l^k}{g_l},$$

is the passive resting potential.
If the membrane potential of a point neuron is only determined by the currents (2.1) and (2.3), the neuron is purely *passive*. It is equivalent to a resistor-capacitor (RC) circuit, whose voltage is proportional to an exponential-filtered input current.

Non-linear conductors: voltage-gated channels

The other class of ion channels that contribute more to the non-linear behaviour of neurons are *voltage-gated* ion channels. They are generally described by,

$$I_g(t) = \sum_k g_{\max}^k w^k(V) A_m (V - E_g^k), \tag{2.4}$$

where, for each ionic species k, $g_{\max}^k$ is the maximal active conductance per unit area, E_g^k is the reversal potential, and the gating variables $w^k \in [0, 1]$ gives the fractions of channels that are open. Since w^k is non-linearly dependent on V, these channels are modelled as non-linear conductors.
Combining Eqs. (2.1), (2.3) and (2.4) we obtain a general conductance-based model, as resistors are simply linear conductors. Due to the non-linearity, the model is generally not analytically solvable, especially when many ionic species are considered. We therefore focus our model only in the sub-threshold regime and instead implant active properties as threshold behaviours to compensate the removal of non-linear ion channels. More details of models of spiking neurons will be discussed in §2.2.2. Nonetheless, within the subthreshold regime, the effects of voltage-gated ion channels are still important. For instance, many neurons are equipped with the I_h current, a hyperpoloarisation-activated depolarising current, that protect them from too strong hyperpolarisations. The I_h channels can be modelled as inductors, that is

$$\frac{L_{res}}{A_m} \frac{\partial I_h}{\partial t} = -\frac{r_{res}}{A_m} I_h + (V - E_l), \tag{2.5}$$

where L_{res} is the inductance and r_{res} the resistance per unit area. The neuron determined by Eqs. (2.1), (2.3) and (2.5) is analogous to an resistor-inductor-capacitor (RLC) circuit, which is therefore called *resonant*.
An alternative approach to obtain Eq. (2.5) is by linearising Eq. (2.4) near E_l and, since it is reduced from a truly active, i.e. non-linear, system, it is also termed as

quasi-active [Koch, 1984; Coombes et al., 2007]. This approach gives a sum of many quasi-active currents in the same form as Eq. (2.5) but the entire entire system becomes linear in V. Hence, even though the number of partial differential equations has not be decreased, the entire system becomes considerably easier and analytically solvable in the frequency domain (see §3.1.2).

Batteries: reversal potentials

Here we identify the reversal potentials in Eqs. (2.2) and (2.4) as the equivalence of batteries in the electrical circuit. A reversal potential of an ionic species is defined to be the membrane potential at which the net flow across membrane is zero. It can be derived directly from the definition and is explicitly given by the famous Nernst equation,

$$E = \frac{k_B T}{zq} \log\left(\frac{N^e}{N^i}\right),$$

where k_B the thermal energy in Joules per ion, T the body temperature in Kelvins and q the charge of an electron in Coulomb are constants [Richardson]. As z the algebraic charge and N^e, N^i the external and internal densities are completely predetermined by the intrinsic properties of the ion, E^k is specific for the ionic species k and thus we assume it constant from the beginning of our models.

2.2.2 Spiking neurons

When the membrane potential reaches −55 to −50 mV, a typical neuron will fire an action potential [Dayan and Abbott, 2001]. The mechanisms can be explained by Eq. (2.4) with certain non-linear conductors (not linearisable). Nonetheless, the change in voltage is so rapid during a short time, that we may want to model the two states independently. Both the approaches are well known in the neuroscience community but we prefer the second one due to its mathematical solvability.

Conductance-based models

The most famous conductance-based model of spiking neurons is the Nobel Prize winning *Hodgkin-Huxley model*, which was first presented in Hodgkin and Huxley [1952] to explain the initiation and propagation of action potentials in the squid giant axon.

There are two non-linear ion currents explicitly considered,

$$I_{\mathrm{Na}} = \bar{g}_{\mathrm{Na}} m^3 h (V - E_{\mathrm{Na}}), \tag{2.6}$$

$$I_{\mathrm{K}} = \bar{g}_{\mathrm{K}} n^4 (V - E_{\mathrm{K}}), \tag{2.7}$$

where $\bar{g}_k = g^k_{\max} A_m$ is the maximal conductance for ionic species $k \in \{\mathrm{K}, \mathrm{Na}\}$ (potassium and sodium), and $n, m, h \in [0, 1]$ are gating variables for the activation of potassium channels, fast activation and slow inactivation of sodium channels, respectively.
Note that there are two gating variables for the sodium current in the model and in general we could consider, for each ion species k,

$$w^k(V) = \prod_i n_i^{\alpha_i},$$

where $n_i \in [0, 1]$ models the ion channel activites of different time scales in response to V, and $\alpha_i > 0$ is usually obtained by fitting model with experimental data.
The Hodgkin-Huxley model has so many dependent variables and non-linear interactions that it is impossible to study analytically. Nevertheless, it can be reduced to the Fitzhugh-Nagumo model by certain assumptions and simplifications [Gerstner and Kistler, 2002]. The reduced model has only two dependent variables, and hence becomes easier to analyse mathematically and to simulate computationally.

Integrate-and-fire models

Instead of a continuous model, Integrate-and-fire (IF) models describe the two states of a neuron, firing and resting, independently by specifying the threshold voltage V_{th}, e.g. −55 mV. When the membrane potential eventually 'integrates' to V_{th}, it 'fires' an action potential and resets its value to V_{re}. Whereas IF models are mathematical idealizations and thus lack of biological details, they are useful because they are analytically solvable, even in cases of stochastic inputs, and therefore they have been widely used in analysis of emergent properties of neuronal circuits [Richardson].
Here we introduce the leaky IF model, whose subthreshold behavior is described simply by the passive membrane (2.1) and the leakage current (2.3), that is,

$$\tau \frac{\partial V}{\partial t} = E_l - V + \frac{I_0}{g_l}, \tag{2.8}$$

where

$$\tau = \frac{C}{g_l}. \tag{2.9}$$

In addition, once $V \geq V_{\text{th}}$, a spike arises and the voltage is instantly reset to V_{re}. For a constant I_0, if the right hand side of Eq. (2.8) is negative, the system has an equilibrium potential at $E_0 = E_l + I_0/g_l$ but is excitable by additional inputs. Otherwise, the potential keeps increasing but always reaches V_{th} before the equilibrium, that is, the neuron spontaneously fires, and the system becomes a non-linear oscillator.

Without loss of generality, we may choose $V(0) = V_{\text{re}}$ and write down the solution to Eq. (2.8) as

$$V(t) = E_0 + (V_{\text{re}} - E_0)e^{-t/\tau}, \tag{2.10}$$

which gives the duration for the potential to reach the threshold by $V(T) = V_{\text{th}}$, explicitly,

$$T = \tau \ln\left(\frac{E_0 - V_{\text{re}}}{E_0 - V_{\text{th}}}\right). \tag{2.11}$$

Since T is exactly the period of the oscillator, the firing rate can be easily found as T^{-1}.

To generalise this simple model, one could add non-linear currents (2.4) (or linearised ones) into Eq. (2.8), or define the spiking behaviour by some function h_s instead of the instant reset. The modifications of the subthreshold behaviour of the neuron (2.8) determines the solvability of the system and is to be discussed in §2.3.1.

The definition of $h_s(t - t_s^i)$ for $t \in [t_s^i, t_s^i + T_s]$ is to manually describe the potential variation during the i-th spike occuring at t_s^i with the spiking voltage profile specified by h_s and T_s the duration of the spike. After the spike, the system switches back to the subthreshold behaviour with effective reset potential $V_{\text{re}} = h_s(T_s)$.

It is straightforward to see that the original leaky IF model with the instant reset is a simplification of the new model with the limit $T_s \to 0$, and the new oscillator has a period of $T + T_s$, which implies the new neuron has a firing rate of $(T + T_s)^{-1}$.

Whereas the definition of h_s is, if not too, trivial, it becomes quite important and useful when we consider neurons with spatial extent, which is the main content of this thesis. Schwemmer and Lewis [2012] implants such extensions of the leaky IF model into the model of a soma and a single dendrite, and studies the dendritic influence on the firing patterns.

Since the soma is attached to one end of the dendrite, there is always a boundary condition for the dendritic membrane potential at this end that enforces it to be same as the somatic potential (i.e. the continuity of voltage, see §2.3.2). Hence, it would be problematic if the somatic potential became discontinuous in time due to the instant reset.

A less realitic but mathematically simpler modification is the quadratic IF model, taking the canonical form as,

$$\frac{dV}{dt} = qV^2 + I_0, \tag{2.12}$$

for $q > 0$. As it allows the voltage reaches infinity within finite time, it is reset to $-\infty$ from $+\infty$, which could produce oscillations and appear to release spikes [Gerstner and Kistler, 2002].

The neuron is excitable for negative I_0, but fires spontaneously only in the case of positive I_0. The model can be rewritten as

$$\frac{d\theta}{dt} = q(1 - \cos\theta) + I_0(1 + \cos\theta), \tag{2.13}$$

by the transformation,

$$V = \tan\left(\frac{\theta}{2}\right) \tag{2.14}$$

As the infinities can be avoided after the transformation and the solutions are analytically accessible, such neuron is used as a basic unit in building neuronal networks, which makes it more consistent and convenient to analyse the effects of microscopic variables on emergent properties of large networks [Latham et al., 2000; Coombes and Byrne, 2016].

2.2.3 Synaptic activities

A *synapse* is a structure of physiological connection between cells in the nervous system. They are essential because they are the means by which neurons transmit electrical signals from one to another. A typical neuron have several thousand synapses, and they mostly connect axons to dendrites. Synapses can be classified into two fundamentally different types, chemical and electrical.

Chemical synapses

At a chemical synapse, the pre-synaptic neuron releases neurotransmitters (typically due to an action potential) from synaptic vesicles into the synaptic cleft, and immediate opposite are the neurotransimitter receptors of the post-synaptic cell. Depending on whether the synapse is excitatory or inhibitory, the post-synaptic cell will produce two different types of transmembrane currents that result in either depolarisation, i.e. excitatory post-syaptic current (EPSC), or hyperpolarisation, i.e. inhibitory post-syaptic current (IPSC).

A common and convenient mathematical model of an EPSC is the alpha function,

$$I_{\text{EPSC}}(t) = A_0 t e^{-B_0 t}, \tag{2.15}$$

for $t = 0$ the time the post-synaptic neuron starts to depolarise. The function reaches the maximum value of $A_0(B_0 e)^{-1}$ at time $t = B_0^{-1}$.

Many chemical synapses can be found on *dendritic spines*, which are extensions on dendrites that directly touch pre-synaptic axons. Whereas S. Ramón y Cajal anticipated the movements of dendritic spines after discovering them, and recent works have verified the fact, they were conventionally considered stable [Bonhoeffer and Yuste, 2002]. In fact, their rapid mophological changes (from seconds to minutes) are still much slower than typical electro-physiological processes (milliseconds), and hence it is quite safe to assume that the dendritic spines are fixed. Furthermore, the size of a typical spine is much smaller than any dendritic branch (see Fig. 2.3) and thus the morphological changes could have little global effects.

As spines are closely related to action potentials, the classical models of spiking neurons introduced in Section 2.2.2 are applicable to them. For the spine head which is equipped with active properties, Baer and Rinzel [1991] assumes Hodgkin-Huxley dynamics and later Bressloff and Coombes [2000] simplifies it with the IF model, while they both treat the spine neck as a passive conductor that follows Ohm's law.

Electrical synapses

An electrical synapse, also known as a gap junction, is a mechanical coupling between adjacent neurons that permits direct ion flows between them. Having been first discovered at the giant motor synapses of the crayfish in the late 1950s, gap junctions are now known to be expressed in the majority of cell types in the brain [Söhl et al., 2005; Dere, 2012].

Unlike chemical synapses, since there is no biochemical process undergoing during the signal transmission between the coupled neurons, gap junctions are faster and metabolically cheaper in passing signals. In addition, there is no orientation preference in the ion flows and thus signals can propagate in either the direction.

We thereby consider a gap junction as a resistor whose conductance is $g_{\text{GJ}} = R_{\text{GJ}}^{-1}$ [Timofeeva et al., 2013]. This simple model is able to reflect the observations that the post-synaptic neuron always receives a signal smaller in amplitude than the source from the pre-synaptic neuron, and that there is almost no time delay in signal transmission.

Hebbian learning

The strength of a synapse varies based on its activities, which is known as the *synaptic plasticity.* Synaptic plasticity is believe to be one of the most basic adaptation processes occuring in the nervous system, that ultimately enables learning behaviours of any creature with a nervous system [Dayan and Abbott, 2001].
Hebbian theory [Hebb, 2005] offers the most well-known explanation for synaptic plasticity, which is often summarised roughly as '*cells that fire together wire together*', and its idea is also widely used in artifical neural networks, e.g. the Hopfield model [Hopfield, 1982].
Whereas the generalised Hebb's rule used in artificial neural networks is often as simple as a bilinear form in the activities of the pre- and post-synaptic neurons, that is,

$$\Delta w_{ij} = \eta x_i x_j,$$

in which x_i and x_j are the activities of neuron i, j, Δw_{ij} is the change in the synaptic strength between them, and η is the learning rate, the biological version, known as *spike-timing dependent plasticity* (STDP), is asymmetric and non-linear (see Fig. 2.8), which reveals the importance of temporal precedence in spikes.
Note these learning rules are usually concerned with chemical synapses and the funtion of STDP could in particular imply the casuality between spikes in pre- and post-synaptic neurons as the signal propagation is uni-directional. The strength of electrical synapses are often difficult to measure experimentally and had been poorly investigated until recently. Turecek et al. [2014] found a mechanism of coupling enhancement at the inferior olive electrical synapse.

2.3 Cable theory

The dendritic electro-physiology started to be revealed via intracellular recordings by using sharp micropipette electrodes in experiments, and was thoroughly studied theoretically by Wilfrid Rall, whose significant contribution to the topic is well summarised in the book of Segev et al. [1995].
The aim of dendritic cable theory is to study the electro-physiology on a potentially complex dendritic morphology, and the approach is to extend the models for an isopotential neuron (see §2.2.1) onto a weighted graph (see §2.1.2).
It is ideal to build electro-physiological models in a three-dimensional space, because '*any other approach risks excluding important features of the three-dimensional structure or incorporating three-dimensional features incorrectly*' [Lindsay et al.,

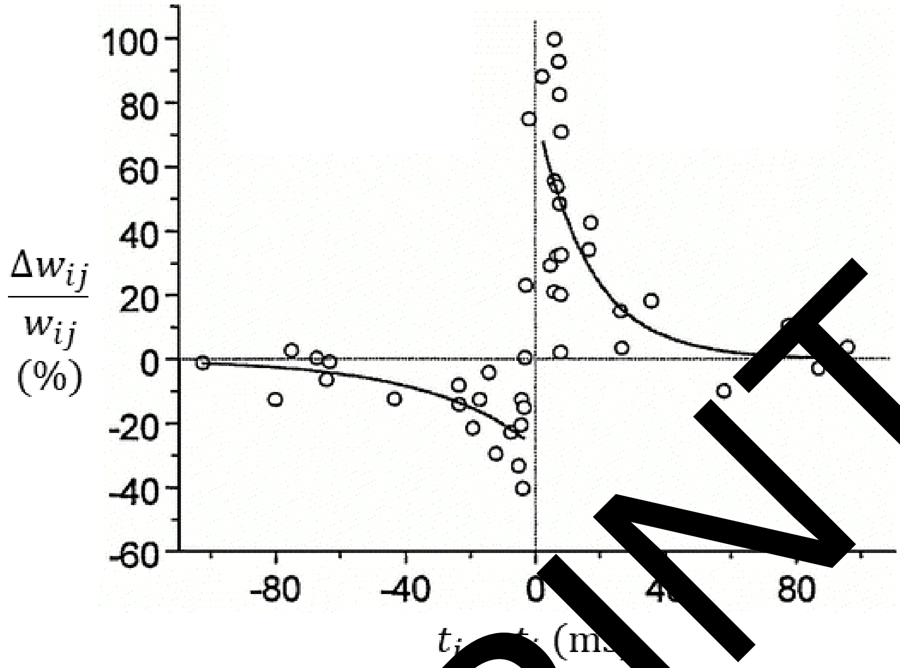

Figure 2.8: Spike-timing dependent plasticity: the normalised change of synaptic strength as a function of the timing difference between the pre- and postsynaptic spikes, where w_{ij} is the synaptic strength between neuron i, j, Δw_{ij} is its change, and t_i and t_j are the spiking times of the two cells, respectively. Modified from Bi and Poo [2001].

2004]. Nonetheless, the standard cable equation is one-dimensional in space, since all radial currents are assumed to be transmembrane, which is justified by the fact that the diameter of a typical neurite is considerably small comparing to its length [Rall, 1969].

2.3.[illegible] Cable equations

Here we first derive the general cable equation of a single dendritic branch with continuously varying radius $r(x)$, into which an input current $I_{in}(x;t)$ is applied. It is then easy to obtain the classical standard cable equation and other simplified models.

General cable equation

To begin with, we work on a little section of the dendritic branch from x to $x + \Delta$. By Kirchhoff's current law (the conservation of electrical currents at a point), we have

$$I_m(x) + I_l(x) + I_g(x) + I(x+\Delta) + I_{in}(x+\Delta) = I(x) + I_{in}(x), \qquad (2.16)$$

where $I(x)$ is the axial current flowing into the section and $I(x+\Delta)$ flowing out. By substituting Eqs. (2.1), (2.3) and (2.4) in Eq. (2.16) and some rearrangments, we have

$$C_m \frac{\partial V}{\partial t} + g_l(V - E_l) + \sum_k g^k_{\max} w^k (V - E^k_g) = \frac{I(x) - I(x+\Delta) + I_{in}(x) - I_{in}(x+\Delta)}{A_m(x, x+\Delta)}, \qquad (2.17)$$

where the surface area of the section is

$$A_m(x, x+\Delta) = 2\pi \int_x^{x+\Delta} \rho(s) ds, \qquad (2.18)$$

with

$$\rho(s) = r(s)\sqrt{1 + (r'(s))^2}, \qquad (2.19)$$

as we assume the cross-sectional area is always perfectly round.
Only the right hand side of Eq. (2.17) depends on Δ and thus by taking the limit $\Delta \downarrow 0$, it becomes,

$$-\frac{[I(x+\Delta) - I(x) + I_{in}(x+\Delta) - I_{in}(x)]/\Delta}{A_m(x, x+\Delta)/\Delta} = -\frac{\partial I/\partial x + \partial I_{in}/\partial x}{2\pi\rho(x)}. \qquad (2.20)$$

If the input current of a total strength of I_{inj} is injected only into the section from y to $y+\Delta$, given the same limit $\Delta \downarrow 0$, we have

$$\left.\frac{\partial I_{in}}{\partial x}\right|_{y^+} = -I_{\text{inj}}\delta(x - y), \qquad (2.21)$$

where $\delta(x)$ is the Dirac delta function. Note that, without loss of generality, from now on we assume all input currents are point processes as we can always easily recover the results for a region of input by integrating the input region.
At the same time, we can compute the axial current $I(x)$ flowing through the section. As we know $V(x)$ and $V(x+\Delta)$ at the respective ends, by Ohm's Law, we have

$$V(x+\Delta) - V(x) = -IR, \qquad (2.22)$$

where

$$R = \frac{R_a \Delta^2}{\int_x^{x+\Delta} A_c(s) ds}, \qquad (2.23)$$

for R_a the axial resistivity and $A_c(x) = \pi r^2(x)$ the cross-sectional area. By simple arithmetics, it follows from the above equations that

$$I = -\frac{\int_x^{x+\Delta} A_c(s)ds}{R_a \Delta} \frac{V(x+\Delta) - V(x)}{\Delta},$$

and again with the limit $\Delta \downarrow 0$, we obtain

$$I(x) = -\frac{1}{r_a} \frac{\partial V}{\partial x}, \tag{2.24}$$

where

$$r_a(x) = \frac{R_a}{A_c(x)}, \tag{2.25}$$

which gives

$$\frac{\partial I}{\partial x} = -\frac{\pi}{R_a} \frac{\partial}{\partial x} \left[r^2(x) \frac{\partial V}{\partial x} \right]. \tag{2.26}$$

The *general cable equation* of a radius-varying dendrite with non-linear channels are obtained by substituing Eqs. (2.21) and (2.26) in Eq. (2.[illegible]), that is,

$$C_m \frac{\partial V}{\partial t} = -g_l(V - E_l) - \sum_k g_{\max}^k w^k (V - E^k) + \frac{1}{2R_a \rho(x)} \frac{\partial}{\partial x} \left[r^2(x) \frac{\partial V}{\partial x} \right] + I_0, \tag{2.27}$$

where

$$I_0 = \frac{I_{\text{inj}} \delta(x - y)}{2\pi \rho(x)}, \tag{2.28}$$

could be considered as the driven force in Eq. (2.27). Note that I_0 is completely determined by y and I_{inj}, because $\delta(x - y) = 0$ unless $x = y$.

Simplified cable equations

As most of the voltage-gated channels are non-linear, Eq. (2.27) is generally impossible to solve analytically. Nonetheless, in the subthreshold regime, they could be linearised and the I_h channel is a main representative (see §2.2.1). Substituting the non-linear currents in Eq. (2.27) by the I_h current following Eq. (2.5), we obtain the *quasi-active (resonant) cable equation with tapering*,

$$C \frac{\partial V}{\partial t} = -g_l V - I_h + \frac{1}{2R_a \rho(x)} \frac{\partial}{\partial x} \left[r^2(x) \frac{\partial V}{\partial x} \right] + I_0, \tag{2.29a}$$

$$L_{res} \frac{\partial I_h}{\partial t} = -r_{res} I_h + V. \tag{2.29b}$$

Note that, without loss of generality, from now on we measure the membrane potential from E_l and use C instead of C_m as the membrane capacitance per unit unless otherwise specified.

A further simplification is to remove the I_h current from the model, which can be experimentally performed by toxinating the I_h channels, and is mathematically equivalent to take the limit $r_{res} \to \infty$. The *passive cable equation with tapering* is thus obtained,

$$C\frac{\partial V}{\partial t} = -g_l V + \frac{1}{2R_a\rho(x)}\frac{\partial}{\partial x}\left[r^2(x)\frac{\partial V}{\partial x}\right] + I_0 \tag{2.30}$$

An alternative simplification of Eq. (2.29) is to assume constant dendritic radius $r(x) = r_c$ while keeping the I_h current in the model, which gives the *resonant cable equation with cylinder*,

$$C\frac{\partial V}{\partial t} = -g_l V - I_h + \frac{r_c}{2R_a}\frac{\partial^2 V}{\partial x^2} + I_0, \tag{2.31a}$$

$$L_{res}\frac{\partial I_h}{\partial t} = -r_{res} I_h + V. \tag{2.31b}$$

If we reduce the model with both simplifications, we arrive at the *passive cable equation with cylinder*, i.e. the classical standard cable equation,

$$C\frac{\partial V}{\partial t} = -g_l V + \frac{r_c}{2R_a}\frac{\partial^2 V}{\partial x^2} + I_0, \tag{2.32}$$

or, in a more well known form,

$$\tau\frac{\partial V}{\partial t} = -V + \lambda^2\frac{\partial^2 V}{\partial x^2} + \frac{I_0}{g_l}, \tag{2.33}$$

by identifying

$$\tau = \frac{C}{g_l}, \tag{2.34}$$

$$\lambda^2 = \frac{r_c}{2g_l R_a}. \tag{2.35}$$

Note that the tapering cable equations (2.29) and (2.30) work for general radius-varying dendrites as clearly shown in the derivation. We have chosen the term 'tapering', because the tapered dendrites are to be investigated in more details. In addition, this thesis mainly studies Eq. (2.29) and its simplifications due to their mathematical solvability within the subthreshold regime, while spikes are considered as somatic current inputs which can be added back into the system via I_0.

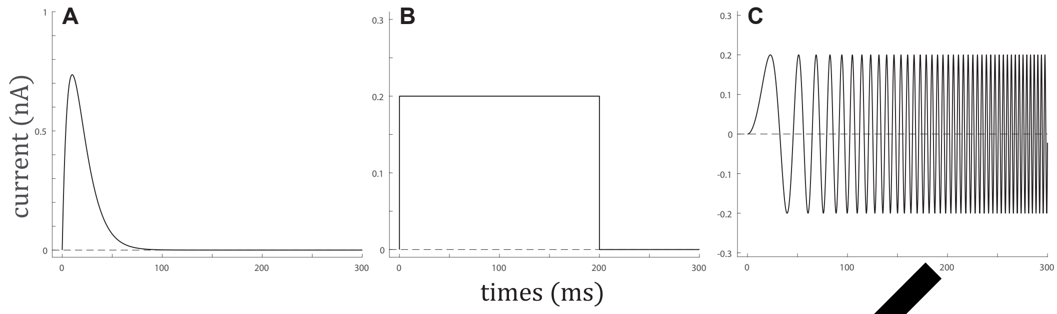

Figure 2.9: Current profiles of three types of inputs with $A_0 = 0.2$ nA. (**A**) An EPSC modelled by an alpha function, with $B_0 = 0.1$. (**B**) A rectangle input. (**C**) A chirp current with $\omega_{\text{chirp}} = 0.003$ kHz.

Input currents

An input current can be caused due to synaptic activities, or directly from experimental injection. Either the case is considered a point process with the location specified by $\delta(x - y)$. The duration and strength of the input is determined by $I_{\text{inj}}(t)$, which is assumed zero for $t < 0$.

If $I_0 = 0$, Eqs. (2.29) - (2.32) are homogeneous differential equations. Since they are all linear, the solutions to the corresponding heterogenous equations with different $I_0 \neq 0$ are additive. It is hence possible to generalise the input from a point process to a field. Nonetheless, in this thesis we consider inputs only as point processes.

The current profiles of I_{inj} can vary from cell to cell due to heterogeneous synaptic activities, or from case to case under different experimental protocols. For simplicity, an EPSC is often modelled by the alpha function (2.15) (see Fig. 2.9A) [Rall, 1967; Jack et al., 1975; Kubota et al., 2011; Coombes and Byrne, 2016].

In addition, we also consider a rectangle input and a chirp current (see Fig. 2.9B,C) in this thesis because they are widely utilised in experiments to investigate, respectively, the asymptotic and oscillating behaviours of electrical systems.

The rectangle input is described by

$$I_{\text{rect}}(t) = A_0 H(t - t_0) H(t_1 - t), \tag{2.36}$$

where A_0 is the strength of the current, $H(t)$ is the Heaviside function, and t_0, t_1 are the starting and finishiing times respectively. For simplicity, we consider $t_0 = 0$ so t_1 is then the duration of the injection. If the finishing time $t_1 \to \infty$, the input becomes a step current. A step current drives a neuron to some new equilibrium voltage, which allows us to compute input and tranfer impedances (see §3.3.3) and

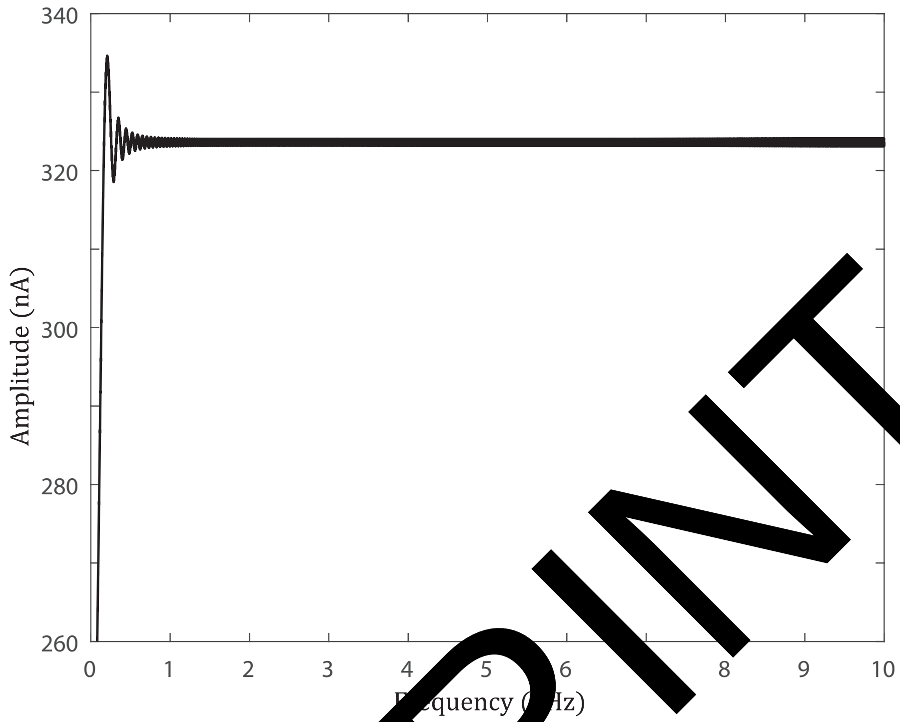

Figure 2.10: Amplitude in the Fourier frequency domain of the chirp current in Fig. 2.9B.

is thus usually a primary indicator of signal attenuation on dendrites.
The chirp current is defined as

$$I_{\text{chirp}}(t) = A_0 \sin\left(\omega_{\text{chirp}} t^2\right), \tag{2.37}$$

whose instantaneous frequency can be found as

$$f(t) = \frac{1}{2\pi}\frac{d}{dt}\left(\omega_{\text{chirp}} t^2\right) = \frac{\omega_{\text{chirp}}}{\pi} t, \tag{2.38}$$

where $\omega_{\text{chirp}}/\pi$ is the rate of frequency, i.e. chirpyness. As the frequency is vayring linearly in time, Eq. (2.37) defines a linear chirp.
Since the amplitudes of the response in the Fourier domain are almost constant for a wide range of frequencies (see Fig. 2.10), that is, the power spectrum of the chirp input is similar to that of a Dirac delta impulse, the envelope of the correspondent oscillating response in time domain will roughly trace the Green's function (which is by nature the response of a Dirac delta input). Therefore, such chirp inputs are useful in experiments to characterise resonant systems.
Note that, however, the phases of a chirp input and a Dirac delta impulse are

different, and thus the chirp responses cannot provide an accurate experimental measurement of the Green's function.

2.3.2 Boundary conditions

Four types of boundary conditions in a neuronal network (see Fig. 2.11) are considered in the thesis. They are all determined by two physical contraints, the Kirchhoff's current law and the continuity of membrane potentials.

Note that it is only for the simplicity of expression that in this section we change the spatial coordinate case by case so that the point under investigation is at the location $x = 0$, while it is common to fix the coordinate when studying a particular model.

Terminals

We call the end of a dendritc branch a *terminal*. It is assumed to be either open or closed.

If a terminal is open, we have

$$V(0;t) = 0, \tag{2.39}$$

which corresponds to the situation where the dendritic branch is cut off at $x = 0$ and thus there is no barrier for ions to move freely into or out from the neuron.

We mostly assume the terminal of a natural dendritic branch is closed, though, that is, there are no axial currents at $x = 0$,

$$\frac{\partial V}{\partial x}(0;t) = 0. \tag{2.40}$$

Branching points

Assume there are N dendritic branches radiating from the point under investigation. Two conditions are required for axial currents and membrane potentials, respectively

$$\sum_{i=1}^{N} \frac{1}{r_{a,i}(0)} \frac{\partial V_i}{\partial x}(0;t) = 0, \tag{2.41}$$

$$V_i(0;t) = V_j(0;t), \tag{2.42}$$

for $i, j \in \{1, 2, 3, \ldots, N\}$ indexing the different branches.

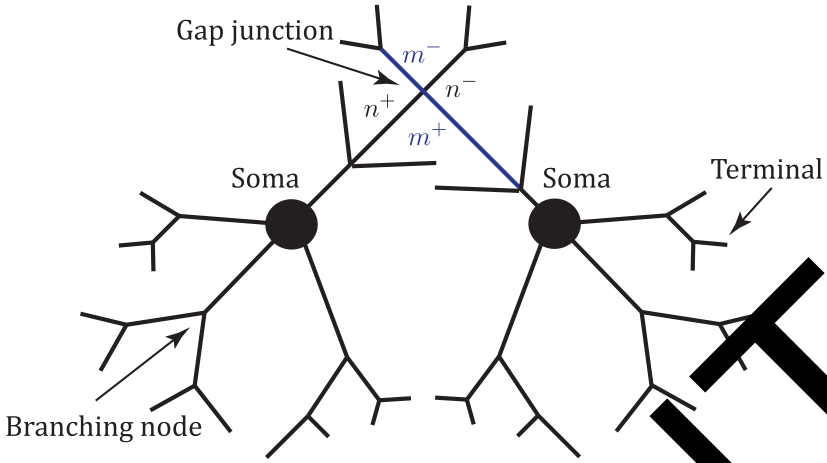

Figure 2.11: A schematic of a network of two neurons connected by a gap junction.

Somata

A soma is treated is an isopotential sphere that is mathematically equivalent to the model of a point neuron as in §2.2.1. Similarly we model its active properties as threshold behaviors in §2.2.2, and therefore we use the resonant model, explicitly,

$$C_S \frac{\partial V_S}{\partial t} = -g_S(V_S - E_l) + \sum_{i=1}^{N} \frac{1}{r_{a,i}(0)} \frac{\partial V_i}{\partial x}(0;t) - I_S, \tag{2.43a}$$

$$L_S \frac{\partial I_S}{\partial t} = -r_S I_S + (V_S - E_l), \tag{2.43b}$$

where V_S is the somatic membrane potential, I_S the somatic resonant current, $C_S = C_{\text{soma}} A_{\text{soma}}$, $g_S = g_{\text{soma}} A_{\text{soma}}$, $L_S = L_{\text{soma}}/A_{\text{soma}}$, $r_S = r_{\text{soma}}/A_{\text{soma}}$ the parameters as in the LRC circuit of the soma, and V_i is the membrane potential of the dendritic branch i radiating from the soma for $i \in \{1, 2, 3, \ldots, N\}$.

In addition to the conservation of current, we again need the continuity of membrane potential, that is,

$$V_S(t) = V_i(0;t). \tag{2.44}$$

Gap junctions

A gap junction is modelled by a resistor whose conductance is $g_{GJ} = R_{GJ}^{-1}$ (see §2.2.3), that is, it follows Ohm's law,

$$\frac{1}{r_{a,m}}\left[\frac{\partial V_{m^-}}{\partial x}(0;t) + \frac{\partial V_{m^+}}{\partial x}(0;t)\right] = g_{GJ}(V_{m^-}(0;t) - V_{n^-}(0;t)), \tag{2.45a}$$

$$\frac{1}{r_{a,n}}\left[\frac{\partial V_{n^-}}{\partial x}(0;t) + \frac{\partial V_{n^+}}{\partial x}(0;t)\right] = g_{GJ}(V_{n^-}(0;t) - V_{m^-}(0;t)), \tag{2.45b}$$

where m^- and m^+ (n^- and n^+) are the two segments of dendritic branch m (branch n) before and after the gap junction.
At the same time, the membrane potentials are continuous on the same branches, that is,

$$V_{m^-}(0;t) = V_{m^+}(0;t), \tag{2.46a}$$

$$V_{n^-}(0;t) = V_{n^+}(0;t). \tag{2.46b}$$

2.3.3 Green's functions

In order to obtain the solution of the cable equations, a classical approach is to solve them with the input currents I_0 as if they are boundary conditions. For instance, Eq. (2.32) is simply a one-dimensional heat equation, which can be solved analytically without I_0 by separation of variables, and plugging I_0 back into the system afterwards.
Since the resonant cable equation with tapering (2.29) and its simplifications are all diffusion equations that are linear differential equations, the approach of Green's functions is chosen as the kernel of a simple diffusion equation is known.
A Green's function is defined as,

$$LG(\bar{x},\bar{y}) = \delta(\bar{y} - \bar{x}), \tag{2.47}$$

where L is a linear differential operator and δ is the Dirac-delta function. It is thus exploited to solve inhomogeneous linear differential equations of the form,

$$Lu(\bar{x}) = f(\bar{x}),$$

for $\bar{x}, \bar{y} \in \mathbb{R}^n$, because we can directly write down the solution as

$$u(\bar{x}) = \int G(\bar{x},\bar{y})f(\bar{y})d\bar{y}, \tag{2.48}$$

or simply,

$$u = G * f, \tag{2.49}$$

where $*$ represents the convolution of the two functions.

A chain of convolutions

Assume $L = L_1 L_2$ and G_1, G_2 are the Green's functions of L_1, L_2 respectively. By applying Eq. (2.49) twice with respect to L_1, L_2 in order,

$$u = G_2 * G_1 * f, \tag{2.50}$$

and, if G is the Green's function of L, we obtain

$$G = G_2 * G_1, \tag{2.51}$$

or explicitly,

$$G(\bar{x}, \bar{y}) = \int G_2(\bar{x}, \bar{z}) G_1(\bar{z}, \bar{y}) d\bar{z}. \tag{2.52}$$

By mathematical induction, the corollary of a chain of convolution follows,

$$G = G_N * G_{N-1} * \cdots * G_2 * G_1, \tag{2.53}$$

if $L = L_1 L_2 L_3 \ldots L_N$, where G is the Green's function of the linear operator L..

Linear time-invarient system

Eq. (2.29) is by definition a linear system and it is also easy to see that the system is time-invariant because all coefficients in the differential equations are constant in t. This property allows us to rewrite the Green's function with respect to t in a convenient way, that is,

$$G(t, t_0) = G(t - t_0). \tag{2.54}$$

Therefore, it is a linear time-invarient (LTI) system and any LTI system can be completely characterised by the Green's function, since the output is simply the convolution of the input with the Green's function,

$$u(t) = \int G(t - t_0) f(t_0) dt_0, \tag{2.55}$$

which is essentially a special case of Eq. (2.48).

Due to Eq. (2.52), Eq. (2.54) can be extended to a series of time points t_0, t_1,

$t_2, \ldots, t_N = t$,

$$G(t, t_0) = G(t, t_{N-1})G(t_{N-1}, t_{N-2}) \ldots G(t_2, t_1)G(t_1, t_0). \tag{2.56}$$

Laplace and Fourier transforms

The Laplace transform $\mathcal{L}$ of a function $f(t)$ is defined as

$$F(\omega) = \mathcal{L}\{f(t)\} = \int_0^\infty f(t)e^{-\omega t}dt, \tag{2.57}$$

where ω is the complex frequency.
By applying the Laplace transform operating on t on Eq. (2.29), we obtain

$$\mathcal{E}(\omega)V(\omega) = \frac{1}{2R_a\rho(x)}\frac{\partial}{\partial x}\left[r^2(x)\frac{\partial V(\omega)}{\partial x}\right] + I_e(\omega) + J_0(\omega), \tag{2.58}$$

where

$$\mathcal{E}(\omega) = C_m\omega + g_l + \frac{1}{r_{res} + L_{res}\omega}, \tag{2.59}$$

$$J_0(\omega) = C_m V(t=0) + \frac{L_{res}I_h(t=0)}{r_{res} + L_{res}\omega}. \tag{2.60}$$

As it is an LTI system, it is safe to assume zero initial data, that is, $V(t=0) = I_h(t=0) = 0$, which gives $J_0 = 0$. Since the Green's function in the frequency domain, also known as the transfer function, is one-to-one correspondent to the Green's function in the time domain, it completely charactersises the system as well. Nonetheless, convolution in the time domain is equivalent to multiplicatioin in the frequency domain, that is, instead of Eq. (2.55), we now have

$$u(\omega) = G(\omega)f(\omega), \tag{2.61}$$

which is easier to analyse and compute.
To recover the function in time domain, the inverse Laplace transfrom $\mathcal{L}^{-1}$ is used,

$$f(t) = \frac{1}{2\pi i}\int_{c-i\infty}^{c+i\infty} F(\omega)e^{t\omega}d\omega, \tag{2.62}$$

for c an arbitrary real number that guarantees the coutour integration to be convergent with respect to $F(\omega)$.

At the same time, the Fourier transform is defined as

$$\hat{f}(\bar{\omega}) = \int_{-\infty}^{\infty} f(t) e^{-i\bar{\omega}t} dt. \tag{2.63}$$

Whereas the Fourier frequency $\bar{\omega}$ is usually understood as a real number, it can be in general treated as complex, in which cases the two transforms (2.57) and (2.63) are indifferent, as long as $f(t) = 0$ for $t < 0$, which is assumed throughout this thesis.
If we assume $\bar{\omega}$ real valued, the Fourier frequency is then merely the complex component of the Laplace frequency, which characterises the periodic behaviours of the system, while the real component is responsible for the transient behaviours.
In addition, the inverse Fourier transform which is defined as

$$f(t) = \frac{1}{2\pi} \int_{-\infty}^{\infty} \hat{f}(\bar{\omega}) e^{it\bar{\omega}} d\bar{\omega}, \tag{2.64}$$

is equivalent to the inverse Laplace transform (2.62), if σ can be chosen as zero, that is, if all singularities are in the left half-plane. Note this condition roughly implies that there exists some $F(\omega)$, such that σ cannot be set as zero, in which cases the inverse Fourier transform will not converge.
Nonetheless, we are not to give any mathematical proof to show that the two transforms are interchangeable for any Green's function that we are to work with, because it will be easy to check the convergence after obtaining explicit expressions.
Whereas the terminology for the Laplace transform will be utilised for consistency, it is more convenient particularly in numerical simulations to use the Fourier transform because the algorithm of the fast Fourier transform (and its inverse) is efficient and accurate.

Additivity of multiple inputs

Whereas it has been long since the existence of non-linear interactions of synaptic inputs on dendrites were discovered [Koch et al., 1983], it is widely accepted that, in the presence of multiple inputs, the total output is the superposition of the outputs of the individual inputs, roughly though.
In our idealised models, this property directly follows from the linearity of the resonant equations, e.g. Eq. (2.58), in which the property can be easily checked. Mathematically, we can write,

$$V(x, \mathbf{y}; \omega) = \mathbf{G}(x, \mathbf{y}; \omega) \mathbf{I_0}^T(\mathbf{y}; \omega), \tag{2.65}$$

where $\mathbf{y} = (y_1, y_2, y_3, \ldots, y_N)$ is an array of N input locations, and $\mathbf{G}, \mathbf{I_0}$ are arrays of size N whose individual elements are successively defined by the correspondent elements of $\mathbf{y}$.

We can easily rewrite Eq. (2.65) into an integration form in y, by assuming the points of $\mathbf{y}$ locate closely in a certain region and taking the limit so that these points are continously distributed, that is,

$$V(x, y; \omega) = \int G(x, y; \omega) I_0(y; \omega) dy, \tag{2.66}$$

with $I_0(y; \omega)$ here a field of input that is a continuous density. This allows us to calculate general inputs directly from our inputs that are assumed specifically to be point processes, and in turn explains why we claim that the assumption is working without loss of generity in Eq. (2.21), the first place the input current included when we derive the cable equations.

Reciprocity between input and output

Since Eq. (2.58) is a second order linear ordinary differential equation, it can be rewritten in the Sturm-Liouville form. At the same time, Eq. (2.58) is also a Fokker-Planck equation which can be easily recast into the canonical form [Park and Petrosian, 1995], whose differential operator is the Hamiltonian (see §4.3.2 for the conversion).

Because a Green's function is symmetric if a self-adjoint operator is acting on it [Stakgold and Holst, 2011], and either the Sturm-Liouville operator or the Hamiltonian operator is self-adjoint, we are guaranteed to have

$$G(x, y) = G(y, x), \tag{2.67}$$

which is known to be the reciprocity principle.

Chapter 3

Method of Local Point Matching

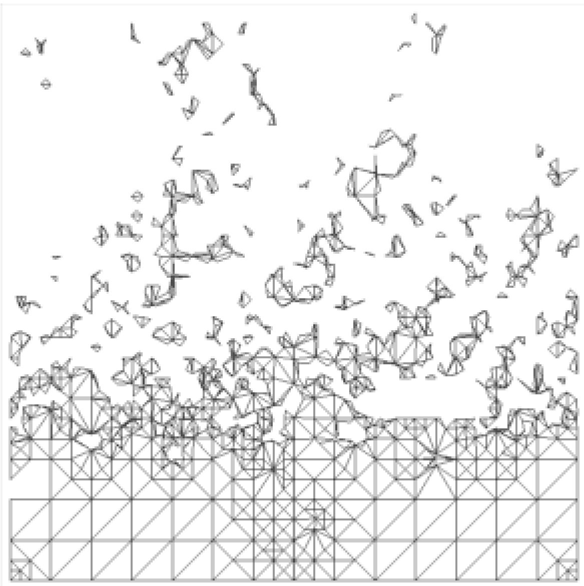

3.1 Framework of sum-over-trips

In order to study the electro-physiology on a dendritic tree, we use the cable theory, which describes the membrain potentials in the sub-threshold regime by Eq. (2.29) with boundary conditions defined in §2.3.2. Since it is important to know the input-output relationship, we naturally adopt Green's functions as the solutions to the cable equations (see §2.3.3). As a Green's function of an input is equivalent to the response to a Dirac-delta impulse at the same input location, the Green's function automatically satisfies all boundary conditions as well. However, an arbitrary dendritic tree generally rises many boundary conditions, and it is not trivial to obtain the Green's function.

An approach to bypass the non-trivial boundary condition problem was first established in Abbott et al. [1991] for obtaining Green's functions on a passive dendritic tree by the path integral formulation of quantum mechanics, and was later termed as *sum-over-trips* in Coombes et al. [2007] in which the approach is extended for a resonant dendritic tree. It is recently generalised in Timofeeva et al. [2013] by including the gap junction as a new boundary condition, so that the approach is able to deal with a gap junction coupled neuronal network.

In this chapter, we only consider dendritic branches as if they are all cylindrical segments, and the change of radius along a single branch can be treated as a chain of cylinders with different radii. We will discuss a dendritic tree with continuous-varying radius in Chapter 4.

3.1.1 On a passive dendritic tree

We can rewrite the passive cable equation with cylinder (2.33) in a dimensionless form,

$$\frac{\partial V}{\partial T} = \frac{\partial^2 V}{\partial X^2} - V + I_c, \tag{3.1}$$

where

$$I_c = \frac{I_{\text{inj}}\delta(x-y)}{2\pi r_c g_l}, \tag{3.2}$$

by absorbing the time and diffusion constants into the diffusion operator,

$$T = \frac{t}{\tau}, \tag{3.3}$$

$$X = \frac{x}{\lambda}, \tag{3.4}$$

where τ and λ are defined in Eqs. (2.34) and (2.35) respectively.

An infinite cable

To begin with, we consider a single cable of an infinite length, on which the Green's function is known to be Gaussian,

$$G_0(X-Y;T) = \frac{1}{2\sqrt{\pi T}} \exp\left[-\frac{(X-Y)^2}{4T}\right], \tag{3.5}$$

which can be obtained by summing up all paths generated by random walks on the cable, i.e. path integral. A path is defined as a configuration of a random walk that starts from X, moves forwards or backwards by length $(2t/N)^{1/2}$ along the cable with equal probability $p_0 = 1/2$ at each step, and stops after N steps in a total time T, with the limit $N \to \infty$ [Abbott et al., 1991].
Heuristically, this purely mathematical description can be understood as individual ions undergoing Brownian motion along the leaky dendritic branch.

A semi-infinite cable

Now consider a single cable of an infinite length but with an open or closed terminal at $X = 0$, that is, $G(0, Y; T)$ satisfies the boundary conditions (2.39) or (2.40) respectively.
From the path integral point of view, the random walk is the same as on the infinite cable except for the origin where the probability of escaping from the cable (into the extracellular environment) is 1 for the open terminal, and 0 for the closed.
On the infinite cable, for $X, Y > 0$

$$G_0(X-Y) = P_0 + P_1, \tag{3.6}$$

where P_0 is the sum of all paths that touches the origin and P_1 is the sum of all other paths which do not (see Fig. 3.1). At the same time,

$$G_0(X+Y) = P_0, \tag{3.7}$$

because Y and $-Y$ is symmetric to the origin and thus the reflection principle applies. To be more specific, since all paths starting from X and terminating at $-Y$ must pass the origin, and by reversing only the direction of the random walks at the origin, there is a one-to-one correspondence between the paths terminating at $-Y$ and Y, which guarantees that the two sums are equal as they are of the equal probability to move in either the direction.
If the terminal is open, all paths touching the origin escape from the cable, that is,

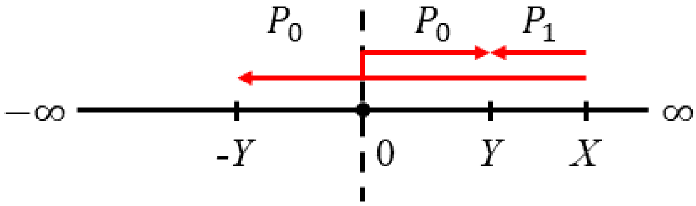

Figure 3.1: Partitions of random walks on an infinite cable starting from X. All the random walks terminating at $-Y$ must pass by the origin $X = 0$, namely P_0. By the reflection principle, there is an equal number of random walks reflecting at the origin and terminating at Y. In addition, the other partition of the random walks terminating at Y does not touch the origin, namely P_1.

the sum only consists of paths that do not touch the origin,

$$G_o(X,Y) = P_1 = G_0(X-Y) - G_0(X+Y). \tag{3.8}$$

If the terminal is closed, all paths touching the origin are forced to reverse direction, that is, the paths terminating at $-Y$ change their destination symmetrically to Y, which gives,

$$G_c(X,Y) = 2P_0 + P_1 = G_0(X-Y) + G_0(X+Y). \tag{3.9}$$

It can be easily checked that Eq. (3.8) and (3.9) satisfy the boundary conditions (2.39) and (2.40) respectively.

A branching node

Here we consider a branching node that connects K semi-infinite cables. The Green's functions can be constructed by applying the same idea as in the previous case. If X, Y locate on the same cable i,

$$G_{ii}(X,Y) = 2p_i P_0 + P_1, \tag{3.10}$$

otherwise, if X, Y locate on the different branches, i.e. $i \neq j$,

$$G_{ij}(X,Y) = 2p_j P_0, \tag{3.11}$$

where P_0, P_1 are defined as in the previous case, and p_i is the probability that the random walk moves into cable i when it stands at the branching node, that should be proportional to the axial conductance, and sum up to 1 over all i, which implies,

$$p_j = \frac{r_j^{3/2}}{\sum_i r_i^{3/2}}, \tag{3.12}$$

assuming the axial resistivity R_a the same for the entire dendritic tree.
To see why Eqs. (3.10) and (3.11) are correct, we can consider p_j as the probability that a closed terminal boundary condition applies at the origin (as $p_j = 1$ in this special case), and $1 - p_j$ for an open terminal (as $p_j = 0$). Eq. (3.10) is thus the superposition of the open and closed terminals defined by Eqs. (2.39) and (2.40). Eq. (3.11) simply follows because all paths have to pass the origin in this situation, which implies the abscence of P_1.
Therefore, by substituting the values of P_0, P_1, we obtain,

$$G_{ij}(X,Y) = \delta_{ij} G_0(X-Y) + (2p_j - \delta_{ij}) G_0(X+Y), \tag{3.13}$$

for $i, j \in \{1, 2, 3, \ldots, K\}$, where δ_{ij} is the Kronecker delta.
It is not difficult to check that Eq. (3.13) satisfies the boundary conditions (2.41) and (2.42), and that Eqs. (3.8) and (3.9) are special cases of Eq. (3.13).

An arbitrary tree

We now consider a passive dendritic tree with branching nodes, terminals and semi-infinite ends in an arbitrary morphology. Recalling,

$$G_{ij}(X,Y;T) = \mathbb{P}(Y \in j | X \in i; T), \tag{3.14}$$

is a probability distribution from the construction of the random walks, which has the Markovian property, that is, the movement along the dendritic tree is independent of the past history. We can hence write down the Chapman-Kolmogorov equation,

$$G_{ij}(X,Y;T) = \sum_k \int_0^{L_k} G_{ik}(X,Z;\epsilon) G_{kj}(Z,Y;T-\epsilon) dZ, \tag{3.15}$$

for k running over all dendritic segments. Since $G_{ij}(X,Y;T)$ is an LTI system, the value of ϵ can be chosen arbitrarily and Eq. (3.15) is indeed well defined due to the properties (2.52) and (2.56).
At a particular node on the dendritic tree with the limit $\epsilon \downarrow 0$, the paths forming $G_{ik}(X,Z;\epsilon)$ are not touching other nodes and thus no boundary conditions other

than those at the node, i.e. Eqs. (2.41) and (2.42), have to be considered.
Therefore, although it is not trivial to contruct the Green's function directly on an arbitrary tree as in the previous cases due to the presence of multiple boundary conditions, it is possible to decomposite the Green's function similarly to Eq. (3.13) locally at individual nodes. By such decompositions successively on all segments, eventually the Green's function is to be rewritten as the sum of Green's functions on an infinite cable G_0.
However, it is more cumbersome than simply presenting and providing the rules for sum-over-trips [Abbott et al., 1991]. We will list the rules in §3.1.2, as the rules for a passive dendritic tree are similar to and essentially a subset of the rules for a resonant tree, and a detailed proof for sum-over-trips with tapering, which is the most recent generalisation, can be found in §4.2.

3.1.2 On a resonant dendritic tree

If we take the Laplace transform of Eq. ([illegible]), or equivalently consider $r(x) = r_c$ as a constant in Eq. (2.58), we obtain the resonant cable equation in the frequency domain, assuming initial zero data,

$$-\frac{\partial^2 V(\omega)}{\partial x^2} + \gamma^2(\omega) V(\omega) = \frac{I_0(\omega)}{CD}, \tag{3.16}$$

where

$$\gamma^2(\omega) = \frac{1}{D}\left[\omega + \frac{1}{\tau} + \frac{1}{C(r_{res} + L_{res}\omega)}\right], \tag{3.17}$$

$$D = \frac{r_c}{2R_aC}, \tag{3.18}$$

$$I_0 = \frac{I_{\text{inj}}(y;\omega)\delta(x-y)}{2\pi r_c}. \tag{3.19}$$

Introducing the scaled spatial variable

$$X = \gamma(\omega)x, \tag{3.20}$$

we obtain

$$(1 - d_{XX})V = A, \tag{3.21}$$

where

$$A(X;\omega) = \frac{I_0(X/\gamma(\omega);\omega)}{CD\gamma^2(\omega)}. \tag{3.22}$$

An infinite cable

Since the Green's function on an infinite cable of the operator $(1 - d_{XX})$ is

$$H_\infty(X) = \frac{1}{2}e^{-|X|}, \tag{3.23}$$

the general solution to Eq. (3.21) is

$$V(X;\omega) = \int_0^\infty H_\infty(X - Y)A(Y;\omega)dY, \tag{3.24}$$

which, in the original coordinates, is

$$V(x;\omega) = \int_0^\infty G_\infty(x - y;\omega)I_{\text{inj}}(y;\omega)dy, \tag{3.25}$$

where

$$G_\infty(x;\omega) = \frac{r_a}{\gamma(\omega)}H_\infty(\gamma(\omega)x) = \frac{r_a}{2\gamma(\omega)}e^{-\gamma(\omega)|x|}. \tag{3.26}$$

Note the definition of $G_\infty(x;\omega)$ is different by a constant scale from that in Coombes et al. [2007] where it is convoluted with I_0 instead of I_{inj}. The new definition of the Green's function by Eq. (3.25) is preferred because it separates the information of the input and the system completely while in the original definition the strength of I_0 is dependent on the input location.

An arbitrary tree

Similarly, if the Green's function on an arbitrary tree of the oparator $(1 - d_{XX})$ is $H_{ij}(X, Y)$, we have

$$V_i(x;\omega) = \sum_j \int_0^{l_j} G_{ij}(x, y;\omega)I_{\text{inj}}(y;\omega)dy, \tag{3.27}$$

where

$$G_{ij}(x, y;\omega) = \frac{1}{z_j(\omega)}H_{ij}(x, y;\omega), \tag{3.28}$$

$$z_j(\omega) = \frac{\gamma_j(\omega)}{r_{a,j}}, \tag{3.29}$$

and $H_{ij}(x, y;\omega)$ is contructed by the rules of sum-over-trips.

Rules for trip construction

A trip is defined to be a highly restricted path that starts from x and terminates y but can only change direction at nodes, while a typical path of the random walk make frequent changes of direction [Abbott et al., 1991]. Explicitly, we define

$$H_{ij}(x, y) = \sum_{\text{trip}} A_{\text{trip}} H_\infty(L_{\text{trip}}(x, y)), \tag{3.30}$$

where A_{trip} is called the trip coefficient, a product of all the node factors A_{nm} along the trip, and $L_{\text{trip}}(x, y)$ is the scaled length of the trip. A node factor A_{nm} is the factor contributed by the trip travelling locally from segment n to m, which is determined by the boundary condition at the node.
As we have shown the local effect of boundary conditions in 3.1.1, the probability of a path is the product of the transition probabilities at the boundary conditions and the transition probability from x to y on a cable without touching any boundaries. If we consider a family of paths that share the same boundary conditions, they virtually live on an infinite cable.
The definition of a trip is based on this idea, where A_{trip} is the product of the node factors A_{nm} which encodes the local information of the nodes that the trip visits, and H_∞ characteristics the random walk on an infinite cable.
Note that the same argument works for the Green's function of any linear differential operator as long as the Markovian property is justified, and thus Eq. (3.30) is the general form for both the Green's functions in time and frequency domains. Nonetheless, H_∞ have different expression in the different domains and it is defined as Eq. (3.23) in the Laplace domain.

Definitions of node factors

By applying Eq. (3.30) to a branching node with semi-infinite cables, we can find that the relationship between the transition probabilities at boundaries and the corresponding node factors are explicitly defined by Eq. (3.13).
They are therefore in the similar form but generally different in time and frequency domains, except for terminals, where

$$A_{mm} = -1, \tag{3.31}$$

for an open terminal, and

$$A_{mm} = 1, \tag{3.32}$$

for a closed one.

At a branching node,

$$A_{nm} = 2p_m - \delta_{nm}, \tag{3.33}$$

where the transition probability p_k is defined as Eq. (3.12) in the time domain, while, in the frequency domain,

$$p_k(\omega) = \frac{z_k(\omega)}{\sum z_k(\omega)}. \tag{3.34}$$

The node factor for a somatic node share the same expression as Eq. (3.33) but

$$p_{S,k}(\omega) = \frac{z_k(\omega)}{z_S(\omega) + \sum z_k(\omega)}, \tag{3.35}$$

where

$$z_S(\omega) = C_S\omega + \frac{1}{R_S} + \frac{1}{r_S + 1/C_S\omega}, \tag{3.36}$$

is the conductance of the somatic membrane.

At a gap junctional node,

$$A_{nm} = p_{GJ,m}, \tag{3.37}$$

and

$$A_{nn} = -p_{GJ,n}, \tag{3.38}$$

for reflecting at the gap junction but

$$A_{mm} = 1 - p_{GJ,n}, \tag{3.39}$$

for passing the gap junction without changing direction, where

$$p_{GJ,m} = \frac{z_m(\omega)}{z_m(\omega) + z_m(\omega) + 2R_{GJ}z_m(\omega)z_n(\omega)}. \tag{3.40}$$

Now, it is not difficult to check that Eq. (3.30) with node factors defined as above (summarised in Fig. 3.2) is the solution to Eq. (3.16) and satisfies all the boundary conditions in §2.3.2.

The detailed proofs for the terminal, branching and somatic node factors can be found in Coombes et al. [2007] and that for the gap junctional node factors in Timofeeva et al. [2013]. A proof for the node factors in the generalised framework of sum-over-trips with tapering, which follows similar protocols and generalises the framework, can be found in §4.2.2.

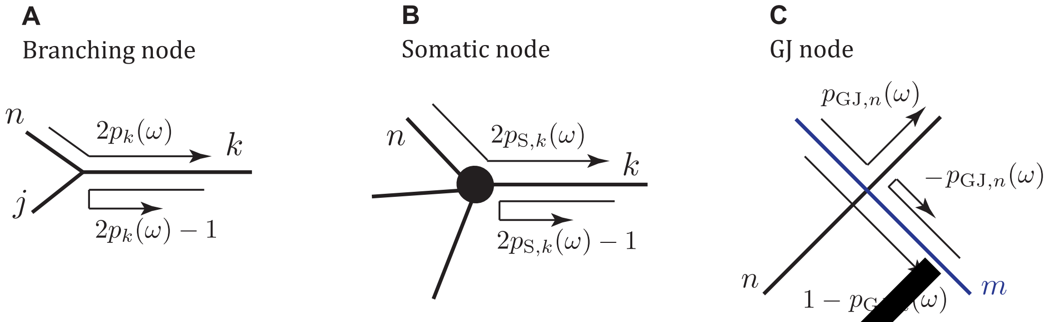

Figure 3.2: The node factors of different types of nodes defined by the sum-over-trip rules. In addition to those in the figure, the node factor of an open terminal is -1 and that of a closed one is $+1$.

3.1.3 Summary of the sum-over-trips algorithm

In above sections, we have reviewed the development and reconstructed the rules of the sum-over-trips framework. Although for a resonant system, we implant the rules first and then prove them satisfying corresponding boundary conditions (as in Coombes et al. [2007]; Timofeeva et al. [201[illegible]]) instead of directly constructing them from the path integral on a passive dendritic tree (as in Abbott et al. [1991]), the path integral explanation works for the resonant systems. However, the probabilities of individual paths become intuitive only in the frequency domain, and it is not straightforward to construct such random walks in the time domain.

Nonetheless, the sum-over-tirps framework has been proven valid and here we summarise the steps of the algorithm for a resonant dendritic tree and see §3.1.2 for the detailed rules:

1. compute the spatial scaling parameter γ for individual dendritic segments and node factors A_{nm} at all nodes;
2. construct all trips from the output location x to the input location y;
3. for each trip, compute the product of all node factors and $H_\infty(L_{\text{trip}})$ where L_{trip} is the scaled length by local γ of the trip;
4. sum over all the trips by Eq. (3.30);
5. scale the sum by a predetermined constant to obtain the Green's function $G(x, y; \omega)$.

In order to retrieve the Green's function in the time domain $G(x, y; t)$, we need to perform the inverse Laplace transform in the end. When an input $I_{\text{inj}}(y; t)$ is considered, it is more convenient to transform it into the Laplace domain so that we can compute the product of $I_{\text{inj}}(y;\omega)$ and $G(x,y;\omega)$, and then bring it back to the time domain, instead of working with the convolution of $I_{\text{inj}}(y;t)$ and $G(x,y;t)$.

3.2 Method of local point matching

By the sum-over-trips framework, the Green's function on an arbitrary dendritic tree with resonant membranes follows,

$$G_{ij}(x,y;\omega) = \frac{1}{z_j(\omega)} \sum_{\text{trip}} A_{\text{trip}}(\omega) H_\infty(L_{\text{trip}}(x,y;\omega)), \tag{3.41}$$

which is simply obtained by substituting Eq. (3.30) into Eq. (3.28).

However, despite of the fact that the convergence of the summation in Eq. (3.41) is guaranteed by the property of H_∞ [Abbott, 1992], for an arbitrary tree in practice, the summation generally consists of an infinite number of trips, and it is not a simple task to rewrite it as a convergent series. In other words, it is non-trivial to enumerate all trips in order. At the same time, for computational purpose in practice, Step 4 in §3.1.3 has to be performed by an algorithm with finite terms.

Here we note that there exist two and only two classes of dendritic morphologies that permits finite trips, an infinite cable and a semi-infinite star, that is, a single node with semi-infinite cables radiating from it. There are no other classes because, if the tree contains at least one finite segment, a trip can reflect at its two ends infinitely many times, which immediately gives an infinite number of trips.

3.2.1 Convergence of sum-over-trips

It is possible to write the infinite summation in Eq. (3.41) as an infinite convergent series for simple morphologies. For instance, if we have a model of a single dendritic branch AB with a finite scaled length L, all trips can be sorted into four classes based on four skeleton trips (see Fig. 3.3), as any other trip with more reflections consists of one skeleton trip and multiple recurrences ($yABy$ or $yBAy$).

Since the recurrences $yABy$ and $yBAy$ both gives the same factor $R = A_A A_B H_\infty(2L)$, where A_A and A_B are the node factors for a trip reflecting at the two ends, the Green's function in this case can be written as

$$G(x,y;\omega) = \frac{1}{z_j} \sum_{n=0}^{\infty} R^n \sum_{i=1}^{4} C_i, \tag{3.42}$$

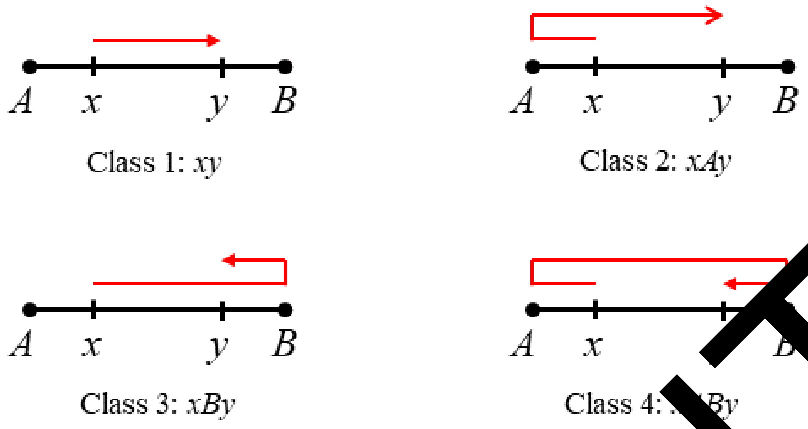

Figure 3.3: The four classes of trips on a single finite dendritic branch. Class 1: xy, the most direct trip not touching two ends. Class 2: xAy, the trips reflecting at one end without passing y. Class 3: xBy, the trip passing y and then reflecting at the other end. Class 4: the trip reflecting at both the ends $xABy$.

where, with $x = 0$ at A and X, Y the scaled coordinates of x, y,

$$C_1 = H_\infty(Y - X), \tag{3.43a}$$

$$C_2 = A_A H_\infty(X + Y), \tag{3.43b}$$

$$C_3 = A_B H_\infty(2L - X - Y), \tag{3.43c}$$

$$C_4 = A_A A_B H_\infty(2L + X - Y), \tag{3.43d}$$

are the factors contributed by the four skeleton trips. As Eq. (3.42) is a geometric series, it can be reduced to an algebraic form that does not contains infinite summation.

A model with two finite segments yields such compact solutions as well. Timofeeva et al. [[illegible]8] considers an example in which the two finite segments are connected by a gap junction and the system is solved by introducing the method of 'words'. This method names each trip with a word consisting of letters that corresponds to its successive movements. It then identifies four shortest words which is essentially the same as the four skeleton trips in the previous case (see Fig. 3.3), and proves any other trips can be constructed by inserting fixed letter pairs into the shortest words. The compact solution is found by combinatorics and appears to be a geometric series again.

However, these methods cannot be generalised to an arbitrary tree. Numerical approximations are thus necessary in computing the infinite summation. Cao and

Abbott [1993] offers an algorithm based on finding the shortest trip, and Caudron et al. [2012] proposes a method with four main trips, plus local recurrences. The four main trips are essentially constructed with the same idea as in Fig. 3.3, and the algorithm is named as the four-classes algorithm.

Caudron et al. [2012] further introduces the length-priority algorithm and compares its convergent errors with the four-classes algorithm on different dendritic morphologies (see Fig. 3.4). Other approaches, e.g. the Monte-Carlo method, are also investigated in the paper, and a more comprehensive study of these numerical methods can be found in Caudron [2012].

We can see from Fig. 3.4 that the approximations converge better on the binary tree, a simple morphology, while considerably worse on realistic dendritic trees. These methods are thus not efficient and effective in the sense of computation, comparing to existing simulation environments, e.g. NEURON [Carnevale and Hines, 2006], which gives accurate solutions.

3.2.2 Deriviation of local point matching

To overcome the problems in the computation and convergence of the sum-over-trips approach, Yihe and Timofeeva [2016] develops the method of local point matching, which is theoretically rooted in the sum-over-trips framework, but avoids the infinite summation and always yields compact solutions in algebraic forms.

To derive the method, we start by introducing the function,

$$J_{ij}(x,y;\omega) = 2z_j G_{ij}(x,y;\omega), \tag{3.44}$$

which can be rewritten as

$$J_{ij}(x,y;\omega) = \sum_{\text{trip}} A_{\text{trip}}(\omega) f(L_{\text{trip}}(x,y;\omega)), \tag{3.45}$$

by Eq. (3.[illegible]1), where

$$f(x) = 2H_\infty(x) = e^{-x}. \tag{3.46}$$

We assume that there are two points v_j and w_j placed on the segment j infinitesimally close to either of its ends and that the point y which is not at a node (i.e. $0 < y < L_j$) is between v_j and w_j. $J_{ij}(x,y;\omega)$ can thus be found as the sum of two

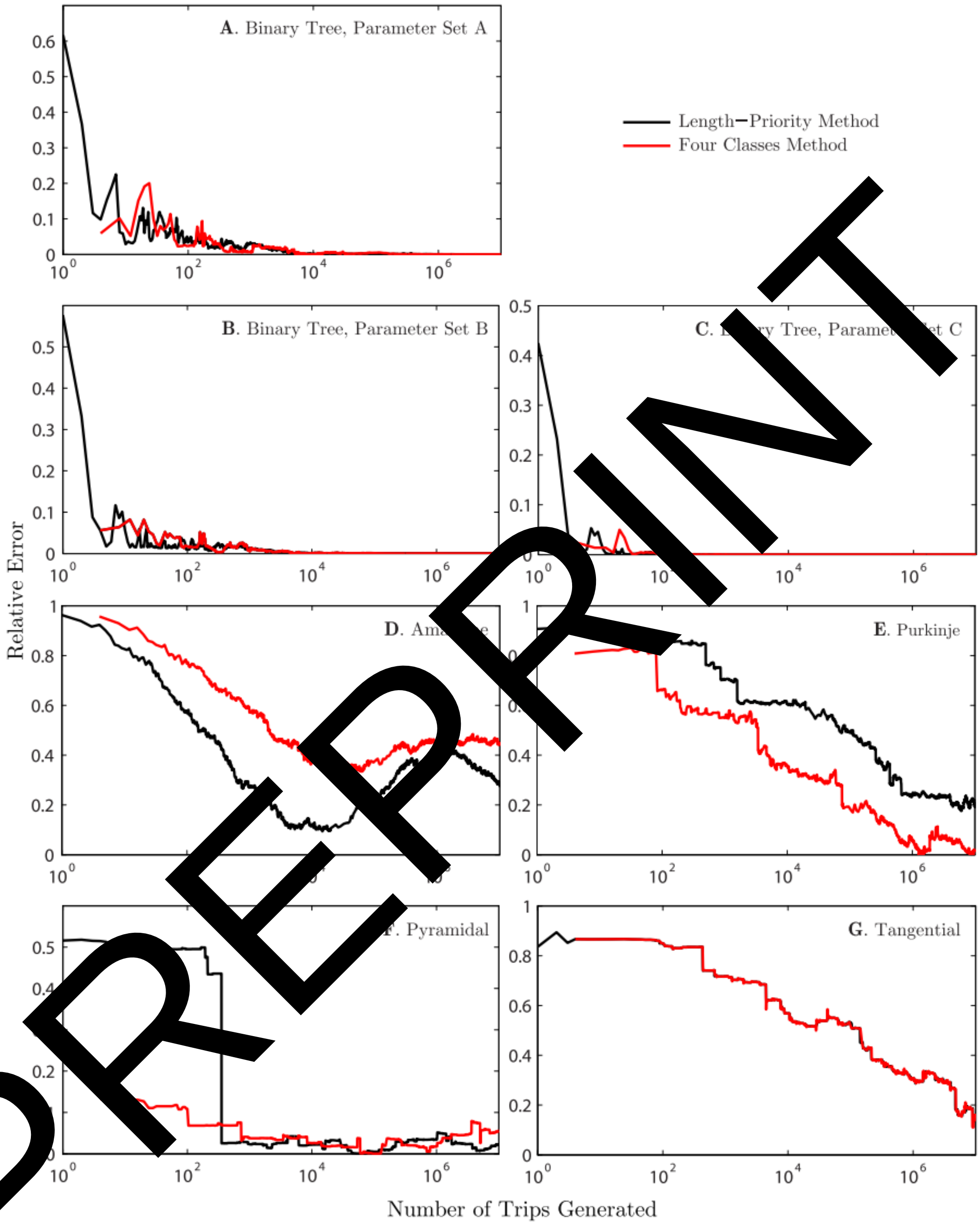

Figure 3.4: Convergence of the four-classes and length-priority algorithms on different dendritic morhpologies. The relative error of the approximation of the Green's function is plotted as a function of the number of trips generated according to either the algorithm in each case [Caudron et al., 2012].

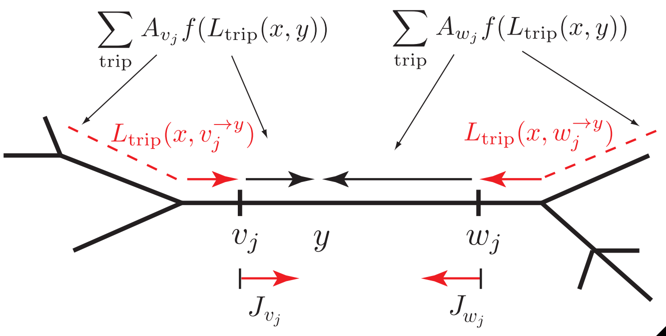

Figure 3.5: Construction of J_y by separating the trips into two groups represented by the functions J_{v_j} and J_{w_j}. Dashed lines indicate all possible trips on a network.

groups of trips,

$$J_{ij}(x,y) = \sum_{\text{trip}} A_{v_j} f(L_{\text{trip}}(x,y)) + \sum_{\text{trip}} A_{w_j} f(L_{\text{trip}}(x,y)) \tag{3.47a}$$

$$= f(v_j - y) \sum_{\text{trip}} A_{v_j} f(L_{\text{trip}}(x, v_j^{\to y})) + f(w_j - y) \sum_{\text{trip}} A_{w_j} f(L_{\text{trip}}(x, w_j^{\to y})). \tag{3.47b}$$

Note that ω is omitted for compactness from this point.

The two separated groups of trips in Eq. (3.47a) are those that are passing by v_j just before reaching y and those that are passing by w_j just before reaching y (see Fig. 3.5). In Eq. (3.47b), we introduce $L_{\text{trip}}(x, v_j^{\to y})$ which defines the length of a trip that moves in the direction of y and ends at v_j before reaching y, and, similarly, $L_{\text{trip}}(x, w_j^{\to y})$ defines the length of a trip that moves in the direction of y and ends at w_j before reaching y (shown in red in Fig. 3.5). A_{v_j} and A_{w_j} are the trip coefficients corresponding to the trips to v_j and w_j.

As y is placed infinitesimally close to one end of the segment, we have $L_{\text{trip}}(x, v_j) = L_{\text{trip}}(x, v_j^{\to y})$, and therefore we introduce

$$J_{ij}(x, v_j) = \sum_{\text{trip}} A_{v_j} f(L_{\text{trip}}(x, v_j^{\to y})), \tag{3.48}$$

and, similarly, for w_j infinitesimally close to the other end of the segment,

$$J_{ij}(x, w_j) = \sum_{\text{trip}} A_{w_j} f(L_{\text{trip}}(x, w_j^{\to y})). \tag{3.49}$$

Now we simplify the notations as $J_{ij}(x, y) = J_y$, $J_{ij}(x, v_j) = J_{v_j}$ and $J_{ij}(x, w_j) = J_{w_j}$ and rewrite Eq. (3.47b) as

$$J_y = f(v_j - y)J_{v_j} + f(w_j - y)J_{w_j}. \tag{3.50}$$

Since both the points v_j and w_j are placed infinitesimally close to the individual ends of the segment j of length L_j, without loss of generality, we consider that $v_j = 0$ and $w_j = L_j$, and therefore Eq. (3.50) becomes

$$J_y = f(y)J_{v_j} + f(L_j - y)J_{w_j}. \tag{3.51}$$

If the point y is located on a semi-infinite branch and w_j is placed on the side towards infinity, then $|w_j - y| \to \infty$, implying $f(w_j - y)J_{w_j} = 0$.
Following similar steps, by placing two points v_k and w_k on each segment k infinitesimally close to either end, we can define functions J_{v_k} and J_{w_k} which can be written in terms of functions J_{v_n} and J_{w_n} associated with points v_n and w_n from all branches connected to a single node. For example, given a node with K segments and K pairs of points (v_k, w_k) (see Fig. 3.6), the function J_{v_k} for $k = 1, 2, 3, \ldots, K$ can be found as

$$\begin{aligned} J_{v_k} &= \sum_{n=1}^{K}\sum_{\text{trip}} A_{w_n} f(L_{\text{trip}}(x, w_n)) a_{nk} f(L_n) \\ &= \sum_{n=1}^{K} A_{nk} f(L_n) \sum_{\text{trip}} A_{w_n} f(L_{\text{trip}}(x, w_n)) \\ &= \sum_{n=1}^{K} A_{nk} f(L_n) J_{w_n}, \end{aligned} \tag{3.52}$$

where L_n is the scaled length of branch n.
Eq. (3.52) can be constructed for any node branches of which do not include point x. If x is located on branch i connected to a node in consideration ($0 < x < L_i$), an additional term representing a direct trip from the starting point x to v_k needs to be added,

$$J_{v_k} = \sum_{n=1}^{K} A_{nk} f(L_n) J_{w_n} + A_{ik} f(x). \tag{3.53}$$

Therefore, summarising Eqs. (3.52) and (3.53), in general we have

$$J_{v_k} = \sum_{n=1}^{K} A_{nk} f(L_n) J_{w_n} + \delta_{ik} A_{ik} f(x). \tag{3.54}$$

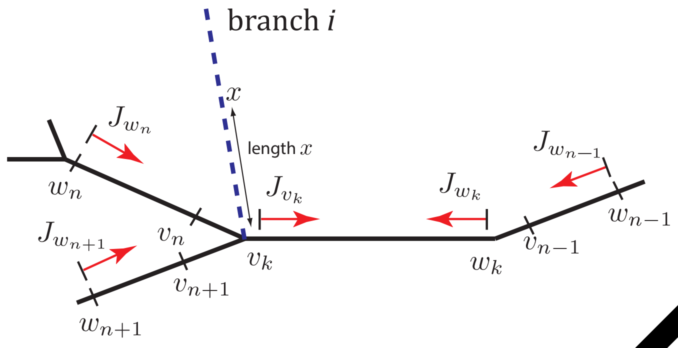

Figure 3.6: Part of a network with the placed pairs of points (v_k, w_k) and the corresponding functions J_{v_k} and J_{w_k}.

Note that J_{w_k} takes exactly the same form as in Eq. (3.54) with different values of node factors and lengths.
Since an unknown J_{v_k} is linearly dependent on other unknowns J_{v_n} that are on the locally connected segments, by writting down all J_v and J_w using Eq. (3.54) we obtain a system of linear equations.
For a fixed network the number of J_v and J_w is equal to the degree sum of the corresponding graph. It is possible to show that the system of equations is linearly independent and therefore has a unique solution. By solving the linear system we can find J_{v_j} and J_{w_j} and obtain $J_y = J_{ij}(x, y)$ from Eq. (3.51). If both x and y are located on the same segment, the direct trip from x to y is added because Eq. (3.51) only considers trips from the two ends of the segment, that is,

$$J_y = f(y)J_{v_j} + f(\mathcal{L}_j - y)J_{w_j} + f(x - y). \tag{3.55}$$

The Green's function $G_{ij}(x, y)$ can then be calculated from Eq. (3.44) as

$$G_{ij}(x, y) = \frac{1}{2z_j} J_y. \tag{3.56}$$

Note that the coefficient before J_y is different from that in Yihe and Timofeeva [2016], because the original definition of the Green's funtion Eq. (3.26) is modified as explained in §3.1.2.

3.2.3 Summary of the local point matching algorithm

In above sections, we have reviewd several techniques for computing the Green's function obtained by the sum-over-trips approach. The methods introduced in §3.2.1

are generally based on truncation of the infinite summmation and thus yield approximated numerical results only, whose error is strongly dependent on the complexity of the dendritic morphology, while the method of local point matching derived in §3.2.2 is analytically exact and computationally cheaper.

Here we summarise the steps of the algorithm for the local point matching method:

1. compute the spatial scaling parameter γ for individual dendritic segments and node factors A_{nm} at all nodes;
2. construct the linear system of J_v and J_w by Eq. (3.54) based on the local connectivity;
3. solve the linear system by matrix inversion;
4. compute J_y and scale it by a predetermined constant to obtain the Green's function $G(x, y; \omega)$.

Note that the first and last steps are the same as in §3.1.3, but the intermediate steps are different, as the method essentially avoids recursive computation for the infinite summation and instead requires only solving the linear system, i.e. matrix inversion.

3.3 Results on arbitrary dendritic trees

Applying the method of local point matching in the framework of sum-over-trips, we can obtain the following theoretical results without specifying the dendritic morphology.

3.3.1 Properties of Green's functions

Here we study some nice properties of a Green's function on an arbitary resonant neuronal network. Since a Green's function is the response function to a Dirac-delta impulse, properties of the Green's function can automatically be extended to any response functions given the input is predetermined.

The input-output reciprocity

If we assume that the original trip has trip coefficient to be,

$$A_{\text{trip}} = A_{ik_1} A_{k_1 k_2} A_{k_2 k_3} \dots A_{k_{n-1} k_n} A_{k_n j}, \tag{3.57}$$

we immediately have the trip coefficient for the reversal trip, namely 'pirt',

$$A_{\text{pirt}} = A_{jk_n} A_{k_n k_{n-1}} A_{k_{n-1} k_{n-2}} \dots A_{k_2 k_1} A_{k_1 i}, \tag{3.58}$$

as the reversal trip exactly travels in the opposite direction. Note that the node factors are equal if $m = n$, while any pair of A_{nm}, A_{mn} share the same denominator and

$$A_{nm} \propto z_m, \tag{3.59}$$

if $m \neq n$. Hence,

$$\frac{A_{\text{trip}}}{A_{\text{pirt}}} = \frac{z_j}{z_i}, \tag{3.60}$$

which gives

$$\frac{\sum A_{\text{trip}} H_\infty(L_{\text{trip}})}{\sum A_{\text{pirt}} H_\infty(L_{\text{pirt}})} = \frac{z_j}{z_i}, \tag{3.61}$$

because for any trip from x to y, its reversal trip has exactly the same (scaled) length, i.e. $L_{\text{trip}}(x, y) = L_{\text{pirt}}(y, x)$.
Therefore, by Eq. (3.41), we can conclude that,

$$G_{ij}(x, y; \omega) = G_{ji}(y, x; \omega), \tag{3.62}$$

and similarly for the Green's function in the time domain. Recall the reciprocity principal (2.67) is discussed for general systems in §2.3.3, and here we have proven it working in our models with complex boundary conditions.
We also note that Eq. (3.62) is the reciprocity identity mentioned in Abbott et al. [1991] and Coombes et al. [2007], but since they define the Green's function differently from ours (up to a constant scale dependent on the input location), there are constant coefficients (depenedent on the locations of input and output) in their reciprocity equations.

Continuity in input locations

In practice, experimentalists can inject current into a node, e.g. a soma. However, it is assumed that the input location y does not locate at any nodes in §3.2.2 where the method of local point matching is derived.
In the original framework of sum-over-trips, locating the input at a node is well defined, since the continuity of the Green's function in the input (or output) location is guaranteed essentially by the path integral formulation. A path starting from (or termiating at) a point infinitesimally close to a node is probabilitically equivalent to

the path starting from (or terminating at) that node, since the transition probability between the two points is asymptotically 1.

By the method of local point matching, we claim that the Green's function is still continuous in the input location. To prove it, we recall that the continuity in x are among the boundary conditions considered in §2.3.2. Since we have proven the input-output reciprocity in the previous section, it immediate yields the continuity in y.

3.3.2 Features of local morphology

Here we consider some interesting features of a part of a dendritic tree by applying the sum-over-trips framework.

Loops in neuronal networks

A single dendritic tree has no loops but a neuronal network has and is commonly highly recurrent, in particular locally. Although the sum-over-trips approach cannot deal with active properties directly, the inclusion of gap junctions into the framework by Timofeeva et al. [2013] has generalised it from single neurons to neuronal networks coupled by gap junctions, and thus loops can be presented.

It is noted firstly in Abbott et al. [1991] that the sum-over-trips approach works on graphs with loops, not only on trees. This can also be clearly seen from the method of local point matching that, when Eq. (3.54) is written down, only pairwise connectivity is useful, and the presence of any loop is not considered.

Conditions for equivalent cylinders

Here we consider a local branching morphology of $n+1$ dendritic branches of length l_i, $i \in \{0, 1, 2, \dots, n\}$, of which segment 0 is eventually connected to the soma and all the rest segments have a closed terminal (see Fig. 3.7).

By the method of local point matching, we can write down

$$a_i = b_i f_i (2p_i - 1) + \sum_{i \neq j = 1}^{n} b_j f_j 2p_i + a_0 f_0 2p_i, \tag{3.63a}$$

$$b_i = a_i f_i, \tag{3.63b}$$

which gives

$$a_i = \frac{2p_i}{1 + f_i^2} \left[a_0 f_0 + \sum_{j=1}^{n} a_j f_j^2 \right], \tag{3.64}$$

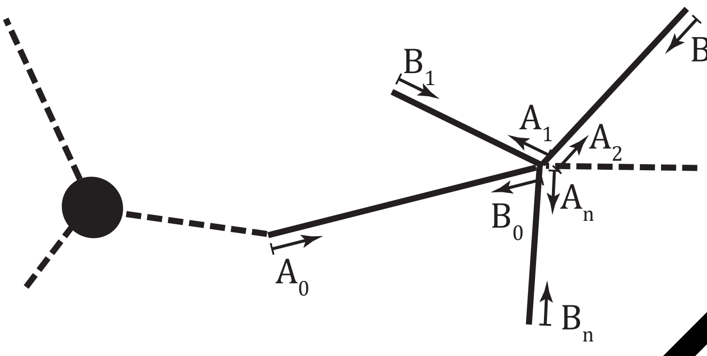

Figure 3.7: Schematic of a branching node in an arbitrary dendritic tree. The node connects n terminal segments, index from 1 to n, and segment 0 that eventually links this branching node to the soma (on the left).

for $f_i = f(l_i)$ and $a_i = J_{A_i}, b_i = J_{B_i}$ being the local trips towards the terminals and the soma, respectively, on segment $i \in \{1, 2, 3, \ldots, n\}$.
By introducing new variables,

$$A = \sum_{j=1}^{n} a_j f_j^2, \tag{3.65}$$

$$B = \sum_{i=1}^{n} \frac{2p_i f_i^2}{1 + f_i^2}, \tag{3.66}$$

Eq. (3.64) gives

$$A = \frac{a_0 f_0 B}{1 - B}, \tag{3.67}$$

and hence

$$\begin{aligned} b_0 &= a_0 f_0 (2p_0 - 1) + \sum b_i f_i 2p_0 \\ &= a_0 f_0 (2p_0 - 1) + 2p_0 A \\ &= a_0 f_0 \left[\frac{2p_0}{1 - B} - 1 \right], \end{aligned} \tag{3.68}$$

where

$$p_0 = \frac{z_0}{z_0 + \sum z_i}. \tag{3.69}$$

Assume the output x does not locate on the local segments under investigation, and that there exists an equivalent cylinder for segments $1, 2, 3, \ldots, n$ that keep the Green's function invariant if they are replaced by it. By the same steps, we have

$$b_0^* = a_0^* f_0 \left[\frac{2p_0^*}{1 - B^*} - 1 \right], \tag{3.70}$$

where

$$p_0^* = \frac{z_0}{z_0 + z_1^*}, \tag{3.71}$$

$$B^* = \frac{2p_1^* f_1^{*2}}{1 + f_1^{*2}}. \tag{3.72}$$

Note that all variables in the equivalent model are denoted by the superscript *.
In order to show the equivalence, we want to show a_0, b_0 are unchanged given the replacement. Since the morphology from the soma to segment 0 is arbitrary but fixed, it is necessary that $a_0^* = a_0, b_0^* = b_0$, which implies

$$\frac{p_0^*}{1 - B^*} = \frac{p_0}{1 - B}, \tag{3.73}$$

since the two conditions $a_0^* = a_0$ and $b_0^* = b_0$ are sufficient and necessary to each other.
Comparing Eqs. (3.66) to (3.72) and (3.6[illegible]) to (3.71), we have to further assume $f_i = f_1^*, B = B^*$, which implies

$$\gamma_1^* l_1^* = \gamma_i l_i \quad \text{for } i = 1, 2, 3, \ldots, n, \tag{3.74}$$

$$z_1^* = \sum_{i=1}^{n} z_i. \tag{3.75}$$

It is now straightforward to see that if the input y does not locate on segment $i = 1, 2, 3, \ldots, n$, the Green's functions of the original branching model and the equivalent cylindrical model are indifferent. If the input does locate on any of segment $i = 1, 2, 3, \ldots, n$, with a distance of l_y away from the branching node, we have

$$J_y = a_i f_i(l_y) + b_i f_i(l_i - l_y), \tag{3.76}$$

which is proportional to a_i, p_i and thus z_i. Due to Eq. (3.56), the Green's functions are also the same.
Furthermore, due to the reciprocity (3.62), we have shown a cylinder is equivalent to a local branching morphology if the conditions (3.74) and (3.75) are satisfied. In the ideal situations, branching structures can be replaced by such equivalent cylinders successively from the terminals to the root (usually the soma) of the dendritic tree. Additionally, a loop can also be equivalent to such a cylinder if the same conditions are valid.
Note the conditions are exactly the famous 3/2 branching rule, as Eq. (3.74) requires

identical electronic lengths while Eq. (3.75) can be written equivalent as

$$r_1^{*3/2} = \sum_{i=1}^{n} r_i^{3/2}, \tag{3.77}$$

where r is the corresponding radius.

3.3.3 Responses at steady states

A typical neuron *in vivo* is constantly receiving thousands of inputs, but here we only consider a single input, as we can sum up the responses due to multiple inputs by the additivity of Green's functions (see §2.3.3). Steady states of the responses are discussed in theory in this section, and we will study the transient behaviours in Chapter 5 by numerical simulations.

Step input

By injecting a step current into the neuron, we are expecting the entire system finally reaches some equilibrium. In order to obtain such equilibria, we can use the *final value theorem* for the Laplace transform, which states that,

$\lim_{t\to\infty} f(t) = \lim_{\omega\to 0} \omega F(\omega)$, *if all poles of* $\omega F(\omega)$ *are in the left half-plane.*
Since we have

$$V(x,y;t) = G(x,y;t) * I_{inj}(t) = \mathcal{L}^{-1}\{G(x,y;\omega) I_{inj}(\omega)\}, \tag{3.78}$$

where $I_{inj} = I_{step}(t)$ is the step input of strength A_0 occuring at time t_0, which is the special case of rectangle input (2.36). Its Laplace transform can be found as,

$$I_{step}(y;\omega) = \frac{A_0}{\omega} e^{-t_0\omega}, \tag{3.79}$$

and we can thus apply the theorem and obtain

$$\lim_{t\to\infty} V(x,y;t) = \lim_{\omega\to 0} \omega \left[G(x,y;\omega) \frac{A_0}{\omega} e^{-t_0\omega} \right] = A_0 G(x,y;\omega = 0). \tag{3.80}$$

Note that, for a passive system $G(x,x;\omega = 0)$ is by definition the input resistance at x, because A_0 in the strength of the injected current and $\lim_{t\to\infty} V(x,x;t)$ is the steady-state voltage. However, the measure cannot fully characterise a resonant neuron, as overshoots and undershoots are to be observed before the system settling down to its equilibrium.

Sinusoidal input

In order to account for the resonant properties of a neuron, we can apply a sinusoidal signal of the form,

$$I_{\sin} = A_0 \sin(\omega_0 t). \tag{3.81}$$

The system will settle on the following steady state,

$$V_{\mathrm{SS}}(x, y; t) = B_0 \sin(\omega_0 t + \phi_K), \tag{3.82}$$

where the amplitude,

$$B_0 = A_0 |K(x, y; \bar{\omega})|, \tag{3.83}$$

and the phase shift,

$$\phi_K = \arg(K(x, y; \bar{\omega})), \tag{3.84}$$

can be found with $G(x, y; i\omega_0)$ [DeCarlo and Lin, 1995].
Therefore, the steady-state responses to sinusoidal inputs with all frequencies fully characterise the Green's function (or the transfer function in LTI systems introduced in §2.3.3). Koch [1984] terms $K(x, y; \bar{\omega}) = G(x, y; \omega)$ for $\bar{\omega} = i\omega$ as the frequency-dependent transfer impedance, and in particular $K(x, x; \bar{\omega}) = G(x, x; \omega)$ is the input impedance, which is a straightforward generalisation of $G(x, x; \omega = 0)$.
Recall that we have introduced the application of chirp inputs in §2.3.1. Since the frequencies are instantaneously varying, the system on principle never reaches any steady state (3.82), which is the reason why the envelope of the oscillating response can only roughly capture the shape of the Green's function.

Chapter 4

Sum-Over-Trips with Tapering

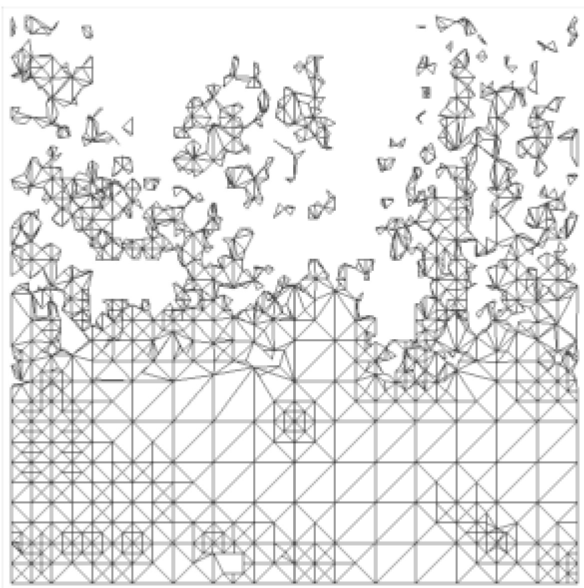

4.1 Tapering cable equations with analytical solutions

In Chapter 3, a comprehensive review of the sum-over-trips framework is present. On an arbitrary resonant dendritic tree with cylindrical segments, the framework permits analytic Green's functions. However, the radius of a realistic dendritic branch could vary from location to location. Such phenomena are mostly noticeable in the distal segments where the dendritic branches taper and terminate.
In this chapter, we are aiming at extending the sum-over-trips framework to dendritic trees with non-cylindrical segments.

4.1.1 Simplification of tapering cable equations

Poznanski [1991] considers the passive tapered cable described by Eq. (2.30) and shows the possibility of obtain analytical solutions given certain constraints. Here we follow the same steps but work on the resonant cable equation with tapering Eq. (2.29) instead.
We first rescale the temporal variable in Eq. (2.29) by

$$T = \frac{t}{\tau} \tag{4.1}$$

where τ is defined in Eq. (2.34), that is,

$$\frac{\partial V}{\partial T} = -V + \frac{1}{2g_l R_a \rho(x)} \frac{\partial}{\partial x}\left[r^2(x)\frac{\partial V}{\partial x}\right] + \frac{I_0 - I_h}{g_l}, \tag{4.2a}$$

$$\frac{\partial I_h}{\partial T} = -r_{res} I_h + V. \tag{4.2b}$$

We then reparameterize the spatial variable by

$$Z = \int_0^x \frac{1}{\lambda(s)} ds, \tag{4.3}$$

where

$$\lambda(x) = \left[\frac{R_m}{2R_a}\right]^{1/2} [r(x)]^{1/2} \left[1 + [r'(x)]^2\right]^{-1/4}, \tag{4.4}$$

and Eq. (4.2a) becomes

$$\frac{\partial V}{\partial T} = -V + \frac{\partial^2 V}{\partial Z^2} + \lambda \frac{\partial}{\partial x}\left(\ln r^2(x)\lambda^{-1}\right)\frac{\partial V}{\partial Z} + \frac{I_0 - I_h}{g_l}, \tag{4.5}$$

or simply,

$$\frac{\partial V}{\partial T} = \frac{\partial^2 V}{\partial Z^2} - V + \frac{d \ln F}{dZ}\frac{\partial V}{\partial Z} + \frac{I_0 - I_h}{g_l}, \tag{4.6}$$

by defining the geometric ratio,

$$F(Z(x)) = F_0 \frac{r^2(x)}{\lambda(x)}. \tag{4.7}$$

Note that the value of the constant F_0 is fixed but arbitrary if only a single dendritic branch is considered, and thus Poznanski [1991] implicitly chooses F_0 so that $F(0) = 1$. We will follow this convention when study a single branch due to its simplicity. However, when we are to deal with an arbitrary tree that has multiple dendritic segments, we prefer $F_0 = 1$ to be a global constant (not dependent on the local segment), so that we have less parameters to concern.
Now introducing a new dependent variable $V^*(Z;T)$ by

$$V(Z;T) = V^*(Z;T)\phi(Z), \tag{4.8}$$

where

$$\phi(Z) = \left[\frac{F(0)}{F(Z)}\right]^{\frac{1}{2}}, \tag{4.9}$$

we can further rewrite Eq. (4.6) as

$$\frac{\partial V^*}{\partial T} = \frac{\partial^2 V^*}{\partial Z^2} - \beta(Z)V^* + \frac{I_0 - I_h}{g_l \phi(Z)}, \tag{4.10}$$

where

$$\beta(Z) = 1 + \frac{\xi^2}{4} + \frac{\xi'}{2}, \tag{4.11}$$

$$\xi(Z) = \frac{d \ln F}{dZ} = \frac{1}{F}\frac{dF}{dZ}. \tag{4.12}$$

At the same time, Eq. (4.2b) simply becomes

$$\frac{L}{\tau}\frac{\partial I_h}{\partial T} = -r_{res} I_h + V^*\phi(Z). \tag{4.13}$$

If we now perform the Laplace transform operating on T to Eqs. (4.10) and (4.13), we obtain

$$\Omega V^* - V^*(t=0) = \frac{\partial^2 V^*}{\partial Z^2} - \beta(Z)V^* + \frac{I_0 - I_h}{g_l \phi(Z)}, \tag{4.14a}$$

$$\frac{L}{\tau}\left[\Omega I_h - I_h(t=0)\right] = -r_{res} I_h + V^*\phi(Z), \tag{4.14b}$$

Type of tapering	$F(Z)$	Constraint	Domain
Exponential	$\exp(2KZ)$	$K < 0$	$0 \leq Z$
Hyperbolic sine	$\frac{\sinh^2 K(Z-\alpha)}{\sinh^2 K\alpha}$	$K^2 > 0$	$0 \leq Z \leq \alpha$
Hyperbolic coinse	$\frac{\cosh^2 K(Z-\alpha)}{\cosh^2 K\alpha}$	$K^2 > 0$	$0 \leq Z \leq \alpha$
Sinuosoidal	$\frac{\cos^2 \lvert K\rvert(Z-\alpha)}{\cos^2 \lvert K\rvert\alpha}$	$K^2 < 0$	$0 \leq Z \leq \pi/\lvert 2K\rvert + \alpha$
Trigonometric	$\cos^2 \lvert K\rvert Z$	$K^2 < 0$	$0 \leq Z \leq \pi/\lvert K\rvert$
Quadratic	$(1 - Z/\alpha)^2$	$\alpha > 0$	$0 \leq Z \leq \alpha$

Table 4.1: Six geometric types that permits analytic solutions for a tapering dendrite. α is a positive constant, while the constant K could be a complex number in certain cases. Modified from Poznanski [1991].

which, by assuming zero initial data and carrying out substitutions and rearrangements, can be reduced to

$$\gamma^2 V^* = \frac{\partial^2 V^*}{\partial Z^2} + \frac{I_0}{g_l(Z)}, \tag{4.15}$$

where

$$\gamma^2 = \Omega + \beta(Z) + \frac{R_m}{r_{res} + L\Omega/\tau} = \tau\omega + \beta(Z) + \frac{R_m}{r_{res} + L\omega}. \tag{4.16}$$

Note that Eq. (4.15) is in the same form as Eq. (3.16) and we can thus solve it analytically if γ is a constant in Z. Otherwise, Eq. (4.15) is non-linear, and mostly solvable via numerical approaches only.

With the assumption that all electrical parameters R_m, r_{res}, L, τ are independent of location, we further need $\beta(Z)$ to be a constant, which, as Poznanski [1991] points out, is equivalently to solve a Ricatti equation and there exist six types of tapering defined by the geometric ratio factor $F(Z)$ that satisfy the condition (see Table 4.1 and Fig. 4.2).

It can be checked by substituting the six types of $F(Z)$ into Eq. (4.11) that, $\beta = 1 - K^2$ for the first three types, $\beta = 1$ for the last, and $\beta = 1 - |K|^2$ for the rest two types, are indeed all constants.

4.1.2 Real shapes of tapered dendrites

Amongst the six types that Eq. (4.15) can be solved analytically, Poznanski [1991] studies the difference in voltage transfers on a cylindrical cable and a tapered branch of the Quadratic type, only in the reparameterised dimensionless coordinate $(Z; T)$. However, it seems more interesting if we can investigate relevant problems in the

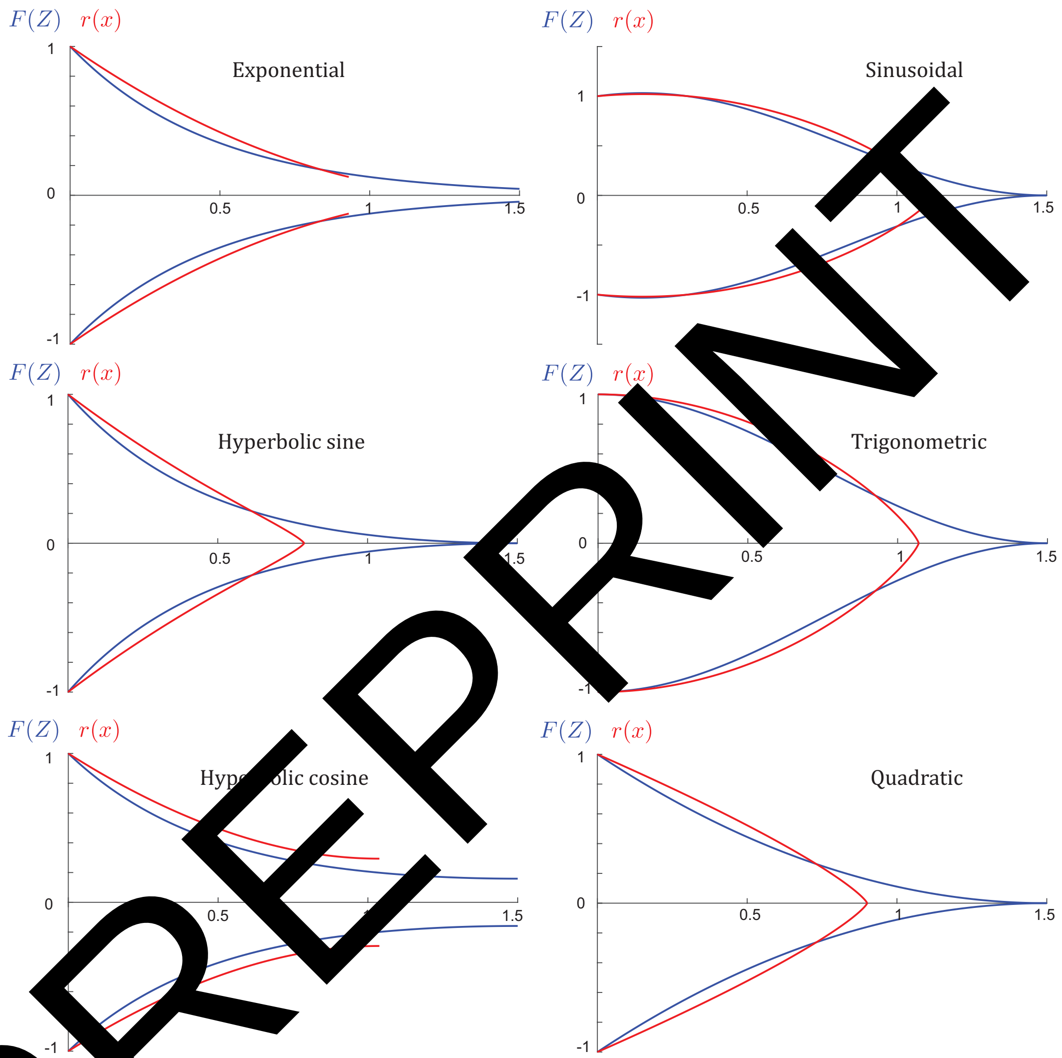

Figure 4.1: Blue curves are tapered cables in the coordinate of $F(Z)$ derived from Table 4.1 with parameters (taken the same as in Poznanski [1991]): $\alpha = 1.5$ and $K = -\pi/3$, except for the sinusoidal cable where $\alpha = 0.15$ and $K = -\pi/2.7$. Red curves are the same cables but in the coordinate of $r(x)$. Note that all functions in this figure are rescaled so that their starting radii equal 1.

original physical coordinate $(x; t)$ instead.

Given $r(x)$, it is straightforward to find $F(Z)$ by Eqs. (4.3), (4.4) and (4.7). However, it is generally only possible to find $r(x)$ from $F(Z)$ by numerical methods, because $r(x)$ is implicitly defined by $F(Z)$, and these six types are not exceptions. This non-trivial reversal problem prevents us from understanding easily the real shapes in the coordinate of $r(x)$ of the six geometric types.

Nonetheless, as the change of dendritic radius is considered small in most situations, that is, $[r'(x)]^2 \ll 1$, Eq. (4.4) reduces to

$$\lambda(x) = \lambda_*[r(x)]^{1/2}, \tag{4.17}$$

where

$$\lambda_* = \left[\frac{R_m}{2R_a}\right]^{1/2}, \tag{4.18}$$

which, by Eq. (4.7), gives

$$F(Z(x)) = \frac{\lambda^3(x)}{\lambda_*^4}, \tag{4.19}$$

and thus we obtain

$$x(Z) = \lambda_*^{3/4} \int_0^Z [F(S)]^{1/3} dS, \tag{4.20}$$

$$r(Z) = [\lambda_* F(Z)]^{2/3}, \tag{4.21}$$

which construct a one-to-one map from x to r.

We therefore obtain $r(x)$ from $F(Z)$ (see Fig. 4.1 for particularly the six types), and it is also noted in Poznanski [1991] that Eq. (4.21) indeed describes the relationship between the radii and the geometric ratios for all the six types.

However, the radius of a real dendritic branch could be less smooth than the nice functions in theory (see Fig. 4.2). Dendritic tapered structures may be different for various types of neurons, or in different locations of a single cell. Additionally, considering constant change of dendritic shapes and imperfect reconstructions by neuron tracing, a conclusion on how realistic dendrties taper or which theoretic type of tapering is the best model has yet not been drawn.

Nonetheless, realistic dendrites are found typically to exhibit initial rapid decay in radius [Bartlett and Banker, 1984; Clements and Redman, 1989; Wilson and Callaway, 2000; Kubota et al., 2011]. Hence, in theoretical works, tapered structures that described by exponential decays, or computationally, decreasing radii of successive compartments by a common factor [Wilson and Callaway, 2000; Lowe, 2002], and

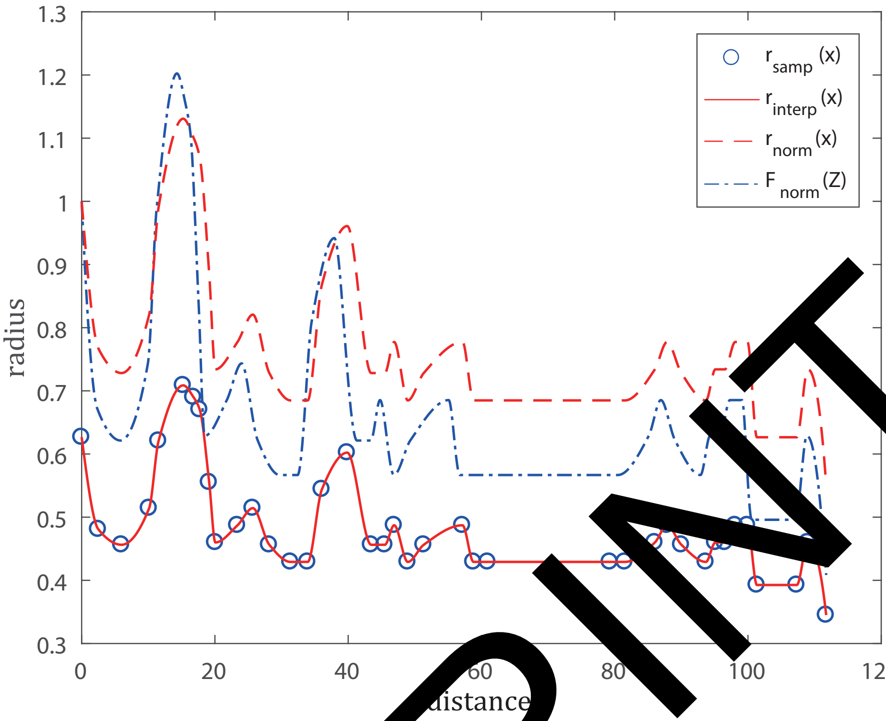

Figure 4.2: An example of the non-trivial continuously varying radius of one terminal dendritic branch (of index 34) of the reconstructed rat pyramidal cell as in Fig. 2.4. The blue circles are the dendritic radius from the reconstructed sample data, and the solid red curve is interpolation of them (by the MATLAB function `interp1` with the method of `pchip`). Their values are measured in μm, and their distances are physical distances, that are in μm as well. The red dashed curve is the normalised radius and the blue dashed curve is the normalised geometric ratio. Both of the dashed curves start with 1 and have no units for their values. In addition, although they appear to be in the same length, the geometric ratio is measured in the electronic distance, which has no units either.

power laws [Cuntz et al., 2007; Romero and Trenado, 2015], are the most favoured models, because they give the seemingly realistic shapes and have simple expressions. Models with (piece-wise) linear tapering is also commonly used [Strain and Brockman, 1975; Lowe, 2002; Walker et al., 2017], which is on principle a special case of power laws, but usually treated as a different type.

Note that the power laws and the exponential decays mentioned in the last paragraph are descripitions of $r(x)$, which are generally convex, except for the special case of linear tapering. We can thus see from Fig. 4.1 that Sinusoidal, Trigometric, and Quadratic types are relatively unrealistic, as they are concave in $r(x)$.

4.1.3 Reasons for favouring Exponential type

Amongst the three tapering types that give more realistic convex shapes, we prefer the Exponential type to the other two Hyperbolic types, and therefore in Chapter 5 where we conduct simulations, we always consider the Exponential type for the tapering structures. Here we explain the reasons.

Equivalence to quadratic tapering

It was long before the existence of the term, geometric ratio, that analytic solutions of $F(Z)$ were obtained for the Exponential type [Rall, 1962]. Later Goldstein and Rall [1974] studies the properties of dendrites following this type of tapering by comparing with cylindrical cables. It is also noted in this work that the Exponential type of $F(Z)$ is approximately the quadratic tapering for $r(x)$, given the assumption $[r'(x)]^2 \ll 1$.

Here we prove this equivalence in the opposite direction, starting by assuming the dendritic segment is tapered quadratically in the physical coordinate, that is,

$$r(x) = r_0 \left[\frac{l-x}{l}\right]^2. \tag{4.22}$$

Since $[r'(x)]^2 \ll 1$, by Eqs. (4.17) and (4.19),

$$\lambda(x) = \lambda_* \frac{l-x}{l}, \tag{4.23}$$

$$F(Z(x)) = \frac{1}{\lambda_*} \left[\frac{l-x}{l}\right]^3. \tag{4.24}$$

At the same time, Eq. (4.3) gives

$$Z(x) = -\frac{l}{\lambda_*} \ln \frac{l-x}{l}. \tag{4.25}$$

Combining Eqs. (4.24) and (4.25), we obtain

$$F(Z) = r_0^{3/2} \exp\left[-\frac{3\lambda_0}{l} Z\right], \tag{4.26}$$

where

$$\lambda_0 = \lambda_* r_0^{1/2}. \tag{4.27}$$

We can therefore conclude the equivalence between the quadratic tapering and the Exponential type by identifying in Eq. (4.26) that

$$K = -\frac{3\lambda_0}{2l}. \tag{4.28}$$

Note that K is a small number because $r_0/l \ll 1$ which can be obtained by differentiating Eq. (4.22) and applying the assumption $[r'(x)]^2 \ll 1$.
Fig. 4.3 shows that the fit between the quadratic tapering by the Exponential type is extremely good.

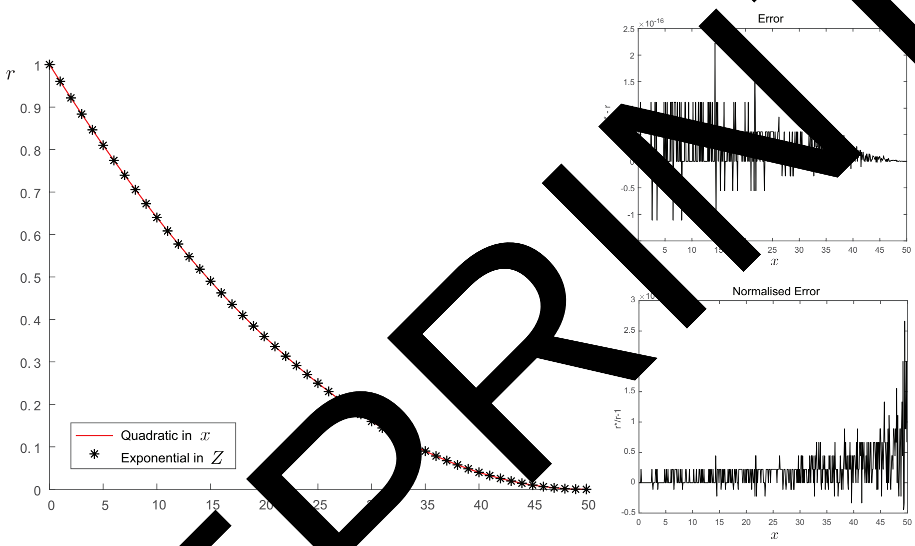

Figure 4.3: Comparison of the original model of quadratic tapering defined by Eq. (4.22) in red and the approximation of the Exponential type defined by Eq. (4.26) in blue dots, transformed back from $F(Z)$ to $r(x)$ by Eq. (4.21), where $l = 50, r_0 = 1, \lambda_0 =$ [illegible]

Optimality of quadratic tapering

It is not only due to its simplicity and representativeness that the quadratic tapering is favoured, but also due to its optimality in current tranfer. Cuntz et al. [2007] suggests that dendritic segments tapered quadratically would optimise current transfers from distal inputs by computational simulation, and later Bird and Cuntz [2016] mathematically proves that the conjecture is valid on a single passive cable that follows quadratic tapering.
The proof starts with the assumption of $r'(x) \ll \partial V(x;t)/\partial x$ and negligible reflective

currents at the distal end where the radius is small, and maximises the functional,

$$\mathcal{J} = \int_0^l V(0, x)dx, \tag{4.29}$$

given the dendritic length l, the distal radius $r(l)$ and the total volume.
The first assumption is almost equivalent to $[r'(x)]^2 \ll 1$, and the second one is justified by the ending radius $r(l)$ being small, as r_a is to be huge near $x = l$, which makes axial currents difficult to propagate in the region, and even harder to reflect at the terminal and propagate back. We can also explain it by the path integral formulation that, there are only a tiny number of paths which touch the end and travel back, because near the end, the transition probability towards the end is considerably small while it is large in the opposite direction.
Bird and Cuntz [2016] also investigates how realistic the model of quadratic tapering is on a dendritic tree and finds that, even though the model cannot match morphologies of all types of neurons, it fits nicely with stereotypic morphology (see Fig. 4.4), of which the neurons are known to obey the 3/2 branching rule [Desmond and Levy, 1984] and undergo replacement constantly throughout life [Cameron and Mckay, 2001].

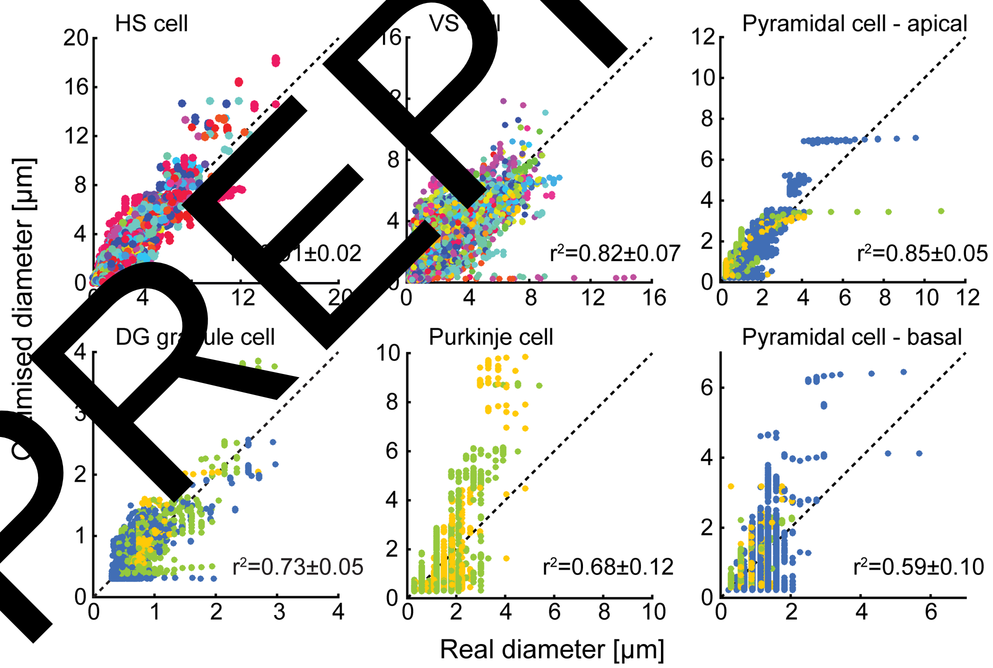

Figure 4.4: Scatter plots of the dendritic radius measured in experiments against the optimal quadratic tapering and the correlation coefficients for different classes of neurons [Bird and Cuntz, 2016].

We therefore prefer the Exponential type to the other five types as it is equivalent to the quadratic tapering, which is optimal in theory and meaningful in practice.

Equivalence to Hyperbolic types

Numerically, one could actually find a good fit of the quadratic tapering by the two Hyperbolic types, but we prefer the Exponential types, because it is characterised by only the parameter K, while the two Hyperbolic types are additionally tuned by α, which set an upper limit for Z (see Table 4.1). However, the limit is enforced by mathematical deductions, rather than biological reality.
To remove this constraint, we could assume $\alpha \to +\infty$. Now we can write down the geometric ratios of the two Hyperbolic types as

$$F(Z) = \left[\frac{e^{K(Z-\alpha)} \pm e^{-K(Z-\alpha)}}{e^{K\alpha} \pm e^{-K\alpha}}\right]^2 = \left[\frac{e^{KZ} \pm e^{-K(Z-2\alpha)}}{e^{2K\alpha} \pm 1}\right]^2. \tag{4.30}$$

The denominator inside the brackets reduces to ± 1 because $K\alpha \to -\infty$, and by the same limit we obtain

$$F(Z) = \left[e^{KZ}\left(1 \pm e^{2K(\alpha-Z)}\right)\right]^2 = e^{2KZ}, \tag{4.31}$$

which is essentially in the same form as the Exponential type.
Therefore, the Exponential types are more representative than the two Hyperbolic types in practice.

4.2 Sum-over-trips with Poznanski's tapering

If each tapered dendritic branch in our models can be described by one of the six types of geometric ratios, the local γ of the segment is constant in Z, which implies that we can reduce Eq. (4.15) to the form of Eq. (3.21) as we have done for Eq. (3.[illegible]6). Therefore, it directly follows the application of the sum-over-trips framework, but in the transformed coordinate of $V^*(Z;\Omega)$.
Note that a trip length is now measured based on Z instead of x and that node factors have to be modified, because the reparameterised dependent variable V^* has to satisfy potentially different boundary conditions, even though the boundary conditions for V are unchanged. In addition, it is more convenient for computational purpose that the algorithm is performed in the original coordinate of $V(x;\omega)$.
Here we derive the extended framework of the sum-over-tirps approach with the six tapering shapes discussed by Poznanski [1991].

4.2.1 The Green's function

Since γ is a constant in Z, we can rescale the spatial variable by $\bar{z} = \gamma Z$, which would reduce Eq. (4.15) to

$$-V^*_{\bar{z}\bar{z}} + V^* = A, \tag{4.32}$$

where

$$A(\bar{x};\omega) = \frac{I_0(\bar{x}/\gamma;\omega)}{\gamma^2 g_l \phi(\bar{x})}. \tag{4.33}$$

Recall that the Green's function of the operator $(1 - d_{\bar{z}\bar{z}})$ is $H_\infty(x) = e^{-|\bar{z}|}/2$, we can write the general solution to Eq. (4.32) as

$$V_i^*(\bar{x};\omega) = \sum_j \int_0^{\bar{l}_j} d\bar{y} H_{ij}(\bar{x},\bar{y}) A_j(\bar{y},\omega), \tag{4.34}$$

where $H_{ij}(\bar{x},\bar{y})$ satisfies

$$(1 - d_{\bar{x}\bar{x}}) H_{ij}(\bar{x},\bar{y}) = \delta_{ij}\delta(\bar{x} - \bar{y}), \tag{4.35}$$

and is to be determined by the sum-over-trip framework.
We may rewrite the solution in the original coordinate as

$$V_i^*(x,\omega) = \sum_j \int_0^{L_j} dy G^*_{ij}(x,y) I_{\text{inj}}(y,\omega), \tag{4.36}$$

where

$$G^*_{ij}(x,y) = \frac{r_{a,j}(y)\lambda_j(y)}{\gamma_j \phi_j(y)} H_{ij}(X(x), Y(y)), \tag{4.37}$$

$$H_{ij}(X,Y) = \sum_{\text{trip}} A_{\text{trip}}(\omega) H_\infty(L_{\text{trip}}), \tag{4.38}$$

and X, Y are the transformed spatial parameters from x, y by Eq. (4.3), respectively. If we rescale everything back to the original coordinate,

$$G_{ij}(x,y;\omega) = \kappa_j(y;\omega)\phi_i(x) \sum_{\text{trip}} A_{\text{trip}}(\omega) H_\infty(L_{\text{trip}}(x,y;\omega)), \tag{4.39}$$

where

$$\kappa_j(y;\omega) = \frac{1}{z_j(y;\omega)\phi_j(y)}, \tag{4.40}$$

$$z_j(y;\omega) = \frac{\gamma_j(\omega)}{\lambda_j(y)r_{a,j}(y)}. \tag{4.41}$$

Note the coefficient before H_{ij} here is different from that in Eq. (3.28). In §4.2.3, it is to be shown that Eq. (4.39) can be reduced to Eq. (3.28) in the case of cylindrical dendrites.

4.2.2 Tapering node factors

As in cylindrical cases, the node factors in the framework of sum-over-trips with tapering also encodes the information of boundary conditions at all nodes at on an arbitrary dendritic tree.

The boundary conditions for V are the same as in §2.3.2, but we are now working with the new dependent variable V^*, and in general each dendritic branch could have different ϕ that reparameterise V into V^*. Thus, here we derive the new node factors.

The deriviation will be conducted as if semi-infinite cables are attached to the node under investigation, because the node factors have only local effects as explained in §3.1.1.

For simplicity, we always consider the node under investigation to locate at the origin of the coordinate, i.e. $X(x=0)=0$, in this section, while we note it is more usual in practical computation to fix the coordinate globally.

Terminal nodes

For terminals, we have

$$G(X(x),Y(y)) = \kappa(y)\phi(X)\left[H_\infty(\gamma Y - \gamma X) + \alpha_k H_\infty(\gamma Y + \gamma X)\right], \tag{4.42}$$

where $\alpha_k, k \in \{o,c\}$ is the node factor for open and closed terminals, respectively. The boundary condition for an open end is given by Eq. (2.39), equivalently,

$$G(0,y) = 0. \tag{4.43}$$

By Eqs. (4.42) and (4.43), we have

$$\kappa(y)\phi(0)(1+\alpha_o)H_\infty(\gamma Y) = 0,$$

which simply gives

$$\alpha_o = -1. \tag{4.44}$$

The boundary condtion for a closed end is given by Eq. (2.40), which implies,

$$0 = \left.\frac{\partial G}{\partial x}\right|_{(0,y)} = \left.\frac{\partial G}{\partial X}\frac{dX}{dx}\right|_{(0,Y)} = \frac{1}{\lambda(0)}\frac{\partial G}{\partial X}(0,Y). \tag{4.45}$$

Since

$$\frac{\partial \phi(X)}{\partial X} = -\frac{1}{2}\xi(X)\phi(X), \tag{4.46}$$

$$\frac{\partial H(\gamma X)}{\partial X} = -\gamma H(\gamma X), \tag{4.47}$$

by differentiating both sides of Eq. (4.42) we have

$$\frac{\partial G}{\partial X} = \kappa(y)\phi(X)\left(\left[\gamma - \frac{1}{2}\xi(X)\right]H_\infty(\gamma Y - \gamma X) - \alpha_c\left[\gamma + \frac{1}{2}\xi(X)\right]H_\infty(\gamma Y + \gamma X)\right),$$

which can be substituted in Eq. (4.45) and gives

$$0 = \frac{\partial G}{\partial X}(0,Y) = \kappa(y)\phi(0)\left(\left[\gamma - \frac{1}{2}\xi(0)\right] - \alpha_c\left[\gamma + \frac{1}{2}\xi(0)\right]\right)H_\infty(\gamma Y).$$

Solving for α_c, we obtain

$$\alpha_c = \frac{\gamma - \xi(0)/2}{\gamma + \xi(0)/2} = \frac{2\gamma}{\gamma + \xi(0)/2} - 1. \tag{4.48}$$

Branching node

Assume that a branching node is attached by N cables and that the input y locates on branch 1. There are generally two cases, the output is also on branch 1, or the output is on a different branch $k \neq 1$. Let $\alpha_k, k \in \{1, 2, 3, \ldots, N\}$ be the node factors, we have

$$G_1(x_1, y) = \kappa_1(y)\phi_1(X)\left[H_\infty(\gamma_1 Y - \gamma_1 X) + \alpha_1 H_\infty(\gamma_1 Y + \gamma_1 X)\right], \tag{4.49a}$$

$$G_k(x_k, y) = \kappa_1(y)\phi_k(X)\alpha_k H_\infty(\gamma_1 Y + \gamma_k X), \qquad \text{for } k \neq 1. \tag{4.49b}$$

The continuity of voltage boundary condition Eq. (2.42) requires

$$G_1(0, y) = G_k(0, y), \tag{4.50}$$

that is,

$$\phi_1(0)(1+\alpha_1) = \phi_k(0)\alpha_k, \qquad \text{for } k \neq 1. \tag{4.51}$$

At the same time, the conservation of currents boundary condition Eq. (2.41) requires

$$0 = \sum_k \frac{1}{r_{a,k}(0)} \frac{\partial G_k}{\partial x}(0,y) = \sum_k \frac{1}{r_{a,k}(0)\lambda_k(0)} \frac{\partial G_k}{\partial X}(0,Y).$$

where

$$\frac{\partial G_1}{\partial X}(0,Y) = \kappa_1(y)\phi_1(0)\left(\left[\gamma_1 - \frac{1}{2}\xi_1(0)\right] - \alpha_1\left[\gamma_1 + \frac{1}{2}\xi_1(0)\right]\right) H_\infty(\gamma_1 Y),$$
$$\frac{\partial G_k}{\partial X}(0,Y) = \kappa_1(y)\phi_k(0)\left(-\alpha_k\left[\gamma_k + \frac{1}{2}\xi_k(0)\right]\right) H_\infty(\gamma_1 Y), \qquad \text{for } k \neq 1.$$

Thus, cancelling out the common factors $\kappa_1(y)H_\infty(\gamma_1 Y)$, we have

$$\frac{\phi_1(0)}{r_{a,1}(0)\lambda_1(0)}\left[\gamma_1 - \frac{1}{2}\xi_1(0)\right] = \sum_k \frac{\phi_k(0)\alpha_k}{r_{a,k}(0)\lambda_k(0)}\left[\gamma_k + \frac{1}{2}\xi_k(0)\right],$$

which can be reduced by Eq. (4.51), that is,

$$\frac{2\gamma_1}{\lambda_1(0)r_{a,1}(0)} = (\alpha_1 + 1)\sum_k \frac{\gamma_k + \xi_k(0)/2}{\lambda_k(0)r_{a,k}(0)}.$$

We can therefore solve for α_1 and then obtain α_k for $k \neq 1$ by Eq. (4.51), which gives,

$$\alpha_1 = \frac{2z_1(0)}{\sum_k z_k^*(0)} - 1, \tag{4.53a}$$
$$\alpha_k = \frac{\phi_1(0)}{\phi_k(0)} \frac{2z_1(0)}{\sum_k z_k^*(0)}, \qquad \text{for } k \neq 1, \tag{4.53b}$$

where

$$z_k^*(x) = \frac{\gamma_k + \xi_k(x)/2}{\lambda_k(x)r_{a,k}(x)}. \tag{4.54}$$

Somatic nodes

Here we assume the same structure as in the last section but for a soma at the centre. We immediately obtain the expression of G_k, the same as Eq. (4.49), and Eq. (4.51) is also valid as the continuity of voltage Eq. (4.50) holds. However, the soma has its own current leakage, which requires a new boundary condition, that is, Eq. (2.43), or equivalently in the Laplace domain,

$$z_S G_k(0,y) = \sum_k \frac{1}{r_{a,k}(0)} \frac{\partial G_k}{\partial x}(0,y), \tag{4.55}$$

whose left hand side, by Eq. (4.50), is

$$z_S G_k(0,y) = z_S G_1(0,y) = z_S \kappa_1(y)\phi_1(0)(1+\alpha_1)H_\infty(\gamma_1 Y),$$

and whose right hand side can be rewritten as

$$z_S G_k(0,y) = \kappa_1(y)\phi_1(0)H_\infty(\gamma_1 Y)\left[\frac{2\gamma_1}{\lambda_1(0)r_{a,1}(0)} - (\alpha_1+1)\sum_k \frac{\gamma_k + \xi_k(0)/2}{\lambda_k(0)r_{a,k}(0)}\right].$$

We therefore obtain

$$\frac{2\gamma_1}{\lambda_1(0)r_{a,1}(0)} - (\alpha_1+1)\sum_k \frac{\gamma_k+\xi_k(0)/2}{\lambda_k(0)r_{a,k}(0)} = z_S(1+\alpha_1),$$

which gives

$$\alpha_1 = \frac{2z_1(0)}{z_S + \sum_k z_k^*(0)} - 1, \tag{4.56a}$$

$$\alpha_k = \frac{\phi_1(0)}{\phi_k(0)}\frac{2z_1(0)}{z_S+\sum_k z_k^*(0)}, \qquad \text{for } k \neq 1. \tag{4.56b}$$

Gap junctional nodes

At a gap junction that connects dendritic branch m and n, if we assume that the input was located on segment m^-, i.e. the segment on branch m before the gap junction, we have

$$G_k(x_k, y) = \kappa_m(y)\phi_k(x_k)\left[\delta_{km^-} H_\infty(\gamma_m Y - \gamma_m X) + \alpha_k H_\infty(\gamma_m Y + \gamma_k X)\right], \tag{4.57}$$

for $k \in \{m^-, m^+, n^-, n^+\}$.

The continuity of voltage boundary condition Eq. (2.46) requires

$$G_{m^-}(0,y) = G_{m^+}(0,y),$$
$$G_{m^-}(0,y) = G_{m^+}(0,y),$$

which gives,

$$1 + \alpha_{m^-} = \alpha_{m^+}, \tag{4.59a}$$
$$\alpha_{n^-} = \alpha_{n^+}. \tag{4.59b}$$

Note that $\phi_{m^-}(0) = \phi_{m^+}(0) = \phi_m(0)$ and $\phi_{n^-}(0) = \phi_{n^+}(0) = \phi_n(0)$ because ϕ_k is continuous on segment k.
At the same time, the conservation of currents boundary condition Eq. (2.45) requires

$$\frac{1}{r_{a,m}(0)}\left[\frac{\partial G_{m^-}}{\partial x}(0,y) + \frac{\partial G_{m^+}}{\partial x}(0,y)\right] = g_{GJ}(G_{m^-}(0,y) - G_{n^-}(0,y)),$$
$$\frac{1}{r_{a,n}(0)}\left[\frac{\partial G_{n^-}}{\partial x}(0,y) + \frac{\partial G_{n^+}}{\partial x}(0,y)\right] = g_{GJ}(G_{n^-}(0,y) - G_{m^-}(0,y)),$$

that is,

$$\frac{1}{r_{a,m}(0)\lambda_m(0)}\left[\frac{\partial G_{m^-}}{\partial X}(0,Y) + \frac{\partial G_{m^+}}{\partial X}(0,Y)\right] = g_{GJ}(G_{m^-}(0,Y) - G_{n^-}(0,Y)), \tag{4.60a}$$
$$\frac{1}{r_{a,n}(0)\lambda_n(0)}\left[\frac{\partial G_{n^-}}{\partial X}(0,Y) + \frac{\partial G_{n^+}}{\partial X}(0,Y)\right] = g_{GJ}(G_{n^-}(0,Y) - G_{m^-}(0,Y)). \tag{4.60b}$$

Since

$$G_k(0,Y) = \kappa_m(y)\phi_k(0)(\delta_{km^-} + \alpha_k)H_\infty(\gamma_m Y),$$
$$\frac{\partial G_k}{\partial X}(0,Y) = \kappa_m(y)\phi_k(0)\left(\delta_{km^-}\left[\gamma_m - \frac{1}{2}\xi_m(0)\right] - \alpha_k\left[\gamma_k + \frac{1}{2}\xi_k(0)\right]\right)H_\infty(\gamma_m Y),$$

Eq. (4.60) can be rewritten as

$$\begin{aligned} & g_{GJ}[\phi_m(0)(1+\alpha_{m^-}) - \phi_n(0)\alpha_{n^-}] \\ =& \frac{\phi_m(0)}{r_{a,m}(0)\lambda_m(0)}\left(\left[\gamma_m - \frac{1}{2}\xi_m(0)\right] - (\alpha_{m^-} + \alpha_{m^+})\left[\gamma_m + \frac{1}{2}\xi_m(0)\right]\right) \\ =& \frac{\phi_n(0)}{r_{a,n}(0)\lambda_n(0)}(\alpha_{n^-} + \alpha_{n^+})\left[\gamma_n + \frac{1}{2}\xi_n(0)\right], \end{aligned}$$

or equivalently, by Eq. (4.59),

$$
\begin{aligned}
&g_{GJ}[\phi_m(0)\alpha_{m^+} - \phi_n(0)\alpha_{n^+}] \\
=&\frac{\phi_m(0)}{r_{a,m}(0)\lambda_m(0)}\left(2\gamma_m - 2\alpha_{m^+}\left[\gamma_m + \frac{1}{2}\xi_m(0)\right]\right) \\
=&\frac{\phi_n(0)}{r_{a,n}(0)\lambda_n(0)}2\alpha_{n^+}\left[\gamma_n + \frac{1}{2}\xi_n(0)\right].
\end{aligned}
$$

Solving for $\alpha_{m^+}, \alpha_{n^+}$ and then substituting the solutions in Eq. (4.[illegible]), we obtain

$$1 + \alpha_{m^-} = \alpha_{m^+} = \frac{z_m(0)\,(1 + 2R_{GJ}z_n^*(0))}{z_m^*(0) + z_n^*(0) + 2R_{GJ}z_m^*(0)z_n^*(0)}, \tag{4.61a}$$

$$\alpha_{n^-} = \alpha_{n^+} = \frac{\frac{\phi_m(0)}{\phi_n(0)}z_m(0)}{z_m^*(0) + z_n^*(0) + 2R_{GJ}z_m^*(0)z_n^*(0)}. \tag{4.61b}$$

4.2.3 Summary and discussion

To summarise, the tapering node factors are

$$A_{mm} = -1, \quad \text{for an open terminal,} \tag{4.62a}$$

$$A_{mm} = \frac{2z_m}{z_m^*} - 1, \quad \text{for a closed terminal,} \tag{4.62b}$$

$$A_{nm} = 2p_m\Phi_{nm} - \delta_{nm}, \quad \text{for a branching node,} \tag{4.62c}$$

$$A_{nm} = 2p_{S,m}\Phi_{nm} - \delta_{nm}, \quad \text{for a somatic node,} \tag{4.62d}$$

$$A_{nm} = p_{GJ,m}\Phi_{nm}, \quad \text{for passing through a gap junctional node,} \tag{4.62e}$$

$$A_{mm} = -p_{GJ,m} - q_m, \quad \text{for reflecting at a gap junctional node,} \tag{4.62f}$$

$$A_{mm} = 1 - p_{GJ,n} - q_m, \quad \text{for passing by a gap junctional node,} \tag{4.62g}$$

in which

$$\Phi_{nm} = \frac{\phi_m}{\phi_n}, \tag{4.63}$$

$$p_k = \frac{z_k}{\sum_k z_k^*}, \tag{4.64}$$

$$p_{S,k} = \frac{z_k}{z_S + \sum_k z_k^*}, \tag{4.65}$$

$$p_{GJ,k} = \frac{z_k}{z_m^* + z_n^* + 2R_{GJ}z_m^*z_n^*}, \tag{4.66}$$

$$q_m = \frac{(1 + 2R_{GJ}z_n^*)\xi_m/2}{z_m^* + z_n^* + 2R_{GJ}z_m^*z_n^*}, \tag{4.67}$$

where all values are taken at the node under investigation.
At the same time, the tapering Green's function Eq. (4.39) can be rewritten as

$$G_{ij}(x,y;\omega) = \frac{\Phi_{ji}(y,x)}{z_j(y;\omega)} \sum_{\text{trip}} A_{\text{trip}}(\omega) H_\infty(L_{\text{trip}}(x,y;\omega)), \tag{4.68}$$

where

$$\Phi_{ji}(y,x) = \frac{\phi_i(x)}{\phi_j(y)} = \left[\frac{r_j(y)}{r_i(x)}\right]^{\frac{3}{4}} \left[\frac{1+[r_j'(y)]^2}{1+[r_i'(x)]^2}\right]^{\frac{1}{8}}, \tag{4.69}$$

is the general formula of Φ_{nm} (whose numerator and denominator are always evaluated at the same point, i.e. the node that connects segment [illegible]).
Despite of the spatial reparameterisation different from that in the cylindrical cases, we can apply the method of local point matching on the rescaled coordinate and therefore the algorithm follows exactly the same steps as in §3.2.3. Once J_y is obtain, we can write down the Green's function as

$$G_{ij}(x,y;\omega) = \frac{\Phi_{ji}(y,x)}{2z_j(y;\omega)} J_y. \tag{4.70}$$

Note that individual segments can have different shapes as long as they belong to the six types of tapering or they are simply cylindrical.

Reduced to cylindrical cases

In order to check the identity between Eqs. (3.41) and (4.68) in the cylindrical cases, we first note that all the newly derived tapering node factors summarised in Eq. (4.62) which are reflective at the node, i.e. A_{mm}, are simply reduced to those defined in §3.[illegible].2 if we return to the cylindrical cases, by recognising $\xi_k = 0, \Phi_{nm} = 1$ for all cylinders, which implies $z_k^* = z_k, q_k = 0$.
However, for $m \neq n$, $A^t_{nm} = A^c_{nm}\Phi_{nm}$ because $\xi_k = 0$ but $\Phi_{nm} \neq 1$. Recall Eq. ([illegible].57) writes a trip coefficient in the cylindrical cases as,

$$A^c_{\text{trip}} = A^c_{ik_1} A^c_{k_1k_2} A^c_{k_2k_3} \dots A^c_{k_{n-1}k_n} A^c_{k_nj}, \tag{4.71}$$

while in the tapering framework, it becomes

$$\begin{aligned} A^t_{\text{trip}} &= A^t_{ik_1} A^t_{k_1k_2} A^t_{k_2k_3} \dots A^t_{k_{n-1}k_n} A^t_{k_nj} \\ &= A^c_{ik_1}\Phi_{ik_1} A^c_{k_1k_2}\Phi_{k_1k_2} A^c_{k_2k_3}\Phi_{k_2k_3} \dots A^c_{k_{n-1}k_n}\Phi_{k_{n-1}k_n} A^c_{k_nj}\Phi_{k_nj}, \end{aligned} \tag{4.72}$$

assuming all node factors are not reflective. Hence, the ratio is

$$\frac{A^t_{\text{trip}}}{A^c_{\text{trip}}} = \Phi_{ik_1}\Phi_{k_1k_2}\Phi_{k_2k_3}\dots\Phi_{k_{n-1}k_n}\Phi_{k_nj} = \frac{\phi_j}{\phi_i}. \tag{4.73}$$

Note that ϕ_k here is not dependent on the specific location x but only on the segment index k, and that the ratio is consistent for all trips from x to y including those have reflections, as all reflective node factors are pairwise the same and cancel each other. We therefore obtain

$$\frac{\sum A^t_{\text{trip}} H_\infty(L_{\text{trip}})}{\sum A^c_{\text{trip}} H_\infty(L_{\text{trip}})} = \frac{\phi_j}{\phi_i}, \tag{4.74}$$

which yields the new term $\Phi_{ji}(y, x)$ in Eq. (4.68) that is not in Eq. (3.41).

Similar results as in cylindrical cases

Many results for the cylindrical Green's function in §[illegible] are directly valid for the tapering Green's function as well. For instance, the framework permits the existence of loops and yields similar results at steady state.

Here we study the reciprocity identity ([illegible]) as it is not straightforward to obtain. For a trip and its reversal configuration, 'pirt', we can write down the trip coefficients in the same forms as Eqs. (3.57) and (3.58) and find the ratio

$$\frac{A_{\text{trip}}}{A_{\text{pirt}}} = \frac{A_{ik_1}A_{k_1k_2}A_{k_2k_3}\dots A_{k_{n-1}k_n}A_{k_nj}}{A_{jk_n}A_{k_nk_{n-1}}A_{k_{n-1}k_{n-2}}\dots A_{k_2k_1}A_{k_1i}}, \tag{4.75}$$

assuming all reflective node factors have cancelled each other.

Let the node connecting segment k_m, k_{m+1} indexed by η_m and $i = k_0, j = k_n$, we have

$$\frac{A_{k_mk_{m+1}}}{A_{k_{m+1}k_m}} = \frac{z_{k_{m+1}}(\eta_m)}{z_{k_m}(\eta_m)}\Phi^2_{k_mk_{m+1}}(\eta_m) = \frac{\gamma_{k_{m+1}}}{\gamma_{k_m}}, \tag{4.76}$$

for $m = 0, 1, 2, \dots, n$, which gives

$$\frac{\sum A_{\text{trip}} H_\infty(L_{\text{trip}})}{\sum A_{\text{pirt}} H_\infty(L_{\text{pirt}})} = \frac{\gamma_j}{\gamma_i}. \tag{4.77}$$

Therefore, by Eq. (4.68), we obtain

$$\frac{G_{ij}(x, y)}{G_{ji}(y, x)} = \frac{z_i(x)}{z_j(y)}\Phi^2_{ji}(y, x)\frac{\gamma_j}{\gamma_i} = 1. \tag{4.78}$$

We then immediately obtain the continuity in input locations as well.

4.3 Sum-over-trips with general morphology

Although we have extended the originial sum-over-trips framework which works on a cylindrical dendritic tree so that the generalised framework can now deal with tapered dendritic branches, the types of the shapes are still limited, because otherwise we cannot solve Eq. (4.15) analytically and do not have a known kernel if γ there is dependent on Z.

Nonetheless, as it is explained in §3.1.2 when we initially derive the sum-over-trips framework from the path integral formulation, the same argument works for all Green's functions other than the heat kernel. Since the resonant cable equation (2.29) is a diffusion equation (that is linear), it always permits a Green's function and can be interpreted as a Fokker-Planck equation constructed from a path integral. Therefore, on principle, any linear cable equation on an arbitrary dendritic tree could be fit into the sum-over-trips framework.

4.3.1 Finite element method: a generalisation

To solve computationally a cable equation, particularly a non-linear one is commonly conducted by discretising the cable into small segments and solving all of them simultaneously via numerial approaches, i.e. the finite element method.

For numerical results, we can apply this method and treat individual segments as cylinders, and thereby the framework of sum-over-trips without tapering (see Chapter 3) can be used to solve for Green's functions on a dendritic tree with tapering.

Here we use the finite element method from a theoretical perspective by taking the partition to the limit of infinite compartments.

Infinite partition

We first consider a resonant cable of length l with both electrical and spatial parameters that are dependent on locations. The cable is then discretised into N compartments which are small enough so that, approximately, all individual comparments are cylinders with constant local parameters.

By the method of local point matching, we can write down

$$J_{a_i} = J_{a_{i-1}} f_i(l_i) \frac{2z_{i+1}}{z_i + z_{i+1}} + J_{b_{i+1}} f_{i+1}(l_{i+1}) \left(\frac{2z_{i+1}}{z_i + z_{i+1}} - 1 \right), \tag{4.79a}$$

$$J_{b_i} = J_{a_{i-1}} f_i(l_i) \left(\frac{2z_i}{z_i + z_{i+1}} - 1 \right) + J_{b_{i+1}} f_{i+1}(l_{i+1}) \frac{2z_i}{z_i + z_{i+1}}, \tag{4.79b}$$

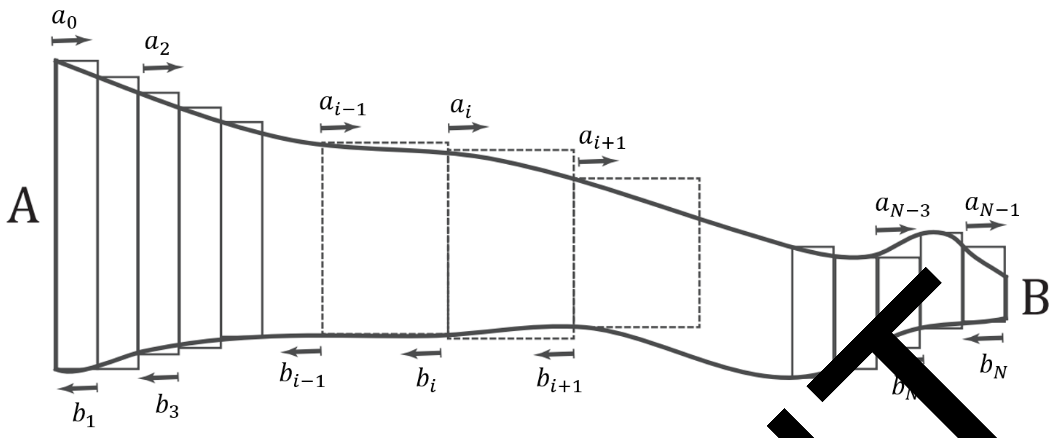

Figure 4.5: A schematic of a general tapered dendrite with finite partition. Since each segment is cylindrical, we can apply the sum-over-paths framework for cylinders. Note the points a_i, b_i are on the left and right of the right end of segment i.

where J_{a_i} and J_{b_i} are unknowns defined recursively at the point $i = 1, 2, 3, \ldots, N-1$, which is also the index of segment $(i-1, i)$ (see Fig. 4.5). Note J_{a_i} is only rooted at point i and pointing in the direction of segment $i+1$. At the two ends, we have

$$J_{a_0} = J_A, \tag{4.80}$$

$$J_{b_N} = J_B, \tag{4.81}$$

where J_A and J_B will be dependent only on each other and all other unknowns from other cables, exactly the same as in the method of local point matching for cylindrical cases.

We may rewrite Eq. (4.79) as

$$\alpha_i(2z_i + \Delta z_i) = (\alpha_i - \Delta\alpha_{i-1})f_i(\Delta x_{i-1})(2z_i + 2\Delta z_i) + (\beta_i + \Delta\beta_i)f_{i+1}(\Delta x_i)\Delta z_i, \tag{4.82a}$$

$$\beta_i(2z_i + \Delta z_i) = (\alpha_i - \Delta\alpha_{i-1})f_i(\Delta x_{i-1})(-\Delta z_i) + (\beta_i + \Delta\beta_i)f_{i+1}(\Delta x_i)2z_i, \tag{4.82b}$$

by renaming $\alpha_i = J_{a_i}, \beta_i = J_{b_i}f_i$ and use Δ for any variable which defines the difference from step $i+1$ to i, e.g. $\Delta z_i = z_{i+1} - z_i$.

Since the Taylor expansion of $f_i(x) = e^{-\gamma_i x}$ at $x = 0$ is

$$f_i(x) = 1 - \gamma_i x + \ldots,$$

we have the following first order expansions,

$$f_i(\Delta x_{i-1}) = 1 - \gamma_i \Delta x_{i-1} + \dots,$$
$$f_{i+1}(\Delta x_i) = 1 - \gamma_{i+1}\Delta x_i + \dots = 1 - \gamma_i \Delta x_i + \dots,$$

as $\gamma_{i+1} = \gamma_i + \Delta\gamma_i$.

By taking the limit $N \to \infty$, that is, all $\Delta x_i \to 0$ and assuming J_a, J_b, γ are smooth, Eq. (4.82) becomes a pair of differential equations,

$$2\alpha z\gamma = (\alpha+\beta)z' - 2z\alpha', \tag{4.83a}$$
$$-2\beta z\gamma = (\alpha+\beta)z' - 2z\beta'. \tag{4.83b}$$

Note from now on we abuse all notations as they are the corresponding continuous variables. However, we have to pay attention to the boundary, as J_{a_0}, J_{b_N} are not defined in Eq. (4.82) but are involved in the definition of $J_{a_1}, J_{b_1}, J_{a_{N-1}}, J_{b_{N-1}}$. When we take the limit, J_{a_1} almost becomes [illegible] and similarly for J_{b_N}. Since the variables are now continuous in x, we may write the boundary conditions as

$$\alpha(0) = J_{A\to}, \tag{4.84}$$
$$\beta(l) = J_{B\to}. \tag{4.85}$$

At the same time, the root of J_{a_1} goes very close to the left end of the cable; we can treat it as the left-forward J ending at this point. The similar and symmetric description fits for $J_{a_{N-1}}$, which gives the other pair of boundary conditions,

$$\beta(0) = J_{\to A}, \tag{4.86}$$
$$\alpha(l) = J_{\to B}. \tag{4.87}$$

These four J's are substantial when applying the method of local point matching, as the [illegible] of the neighbourhood attached to the current segment will ask for this information.

Analytic solutions

By addition and subtraction of Eqs. (4.83a) and (4.83b), we obtain

$$m' + \gamma n = \frac{z'}{z} m, \tag{4.88a}$$
$$n' + \gamma m = 0, \tag{4.88b}$$

where

$$m = \alpha + \beta,$$
$$n = \alpha - \beta,$$

which gives

$$m'' - \left[\frac{\gamma'}{\gamma} + \frac{z'}{z}\right]m' - \left[\gamma^2 + \gamma\left(\frac{z'}{z\gamma}\right)'\right]m = 0, \tag{4.89a}$$
$$n'' - \left[\frac{\gamma'}{\gamma} + \frac{z'}{z}\right]n' - \gamma^2 n = 0. \tag{4.89b}$$

Hence, instead of the coupled equations, we can solve Eq. (4.89b) for n first with the boundary condition,

$$n(0) = J_A - J_{\to A}, \tag{4.90a}$$
$$n(l) = J_{\to B} - J_B, \tag{4.90b}$$

and obtain m by Eq. (4.88b).
Note that, by the method of local point matching, in the case when the input is on the cable under investigation while the output is not, we have

$$G(x, y; \omega) = \frac{1}{2z(y)}[\alpha(y) + \beta(y)] = \frac{m(y)}{2z(y)}. \tag{4.91}$$

Recalling the definitions of $\gamma, \mathcal{E}$ in Eqs. (3.17) and (2.59), we have

$$\gamma^2(x;\omega) = \frac{2R_a}{r}\left(\frac{1}{R_m} + C_m\omega + \frac{1}{r_{res} + \omega L_{res}}\right) = \frac{2R_a(x)\mathcal{E}(x;\omega)}{r(x)}, \tag{4.92}$$

where in general all paramters can be location-dependent. Eq. (4.89b) thereby becomes

$$n'' - [\ln \mathcal{E} r]' n' - \frac{2R_a\mathcal{E}}{r} n = 0. \tag{4.93}$$

If the coefficients in Eq. (4.93) are constants, or Eq. (4.93) is a Cauchy-Euler equation, we can obtain analytic solutions.
In the first case,

$$\mathcal{E} = C_1 r, \tag{4.94}$$

where $C_1 \neq 0$ is an arbitary constant. Note that R_a is assumed to be a global constant, because it is not realistic to assume the axial resistivity varying along the cable.

At the same time,

$$[\ln \mathcal{E}r]' = 2[\ln r]', \tag{4.95}$$

is also a constant (in x), which implies

$$r = e^{C_2 x + C_3}, \tag{4.96}$$

where C_2, C_3 are arbitrary constants. If $C_2 = 0$, r and thus $\mathcal{E}$ are constants, which recovers the most trivial cases that the cable is not tapered and has homogeneous electrical properties.
Otherwise, the cable is tapered exponentially, which, by Eq. (4.94), gives

$$\mathcal{E} = C_4 e^{C_2 x}, \tag{4.97}$$

where $C_4 = C_1 e^{C_3}$ and $C_2, C_4 \neq 0$.
In the other case when Eq. (4.93) is a Cauchy-Euler equation, we have

$$[\ln \mathcal{E}r]' = \frac{C_5}{x + C_0}, \tag{4.98}$$

$$\frac{\mathcal{E}}{r} = \frac{C_6}{(x + C_0)^2}, \tag{4.99}$$

where C_0, C_5, C_6 are arbitrary constants. Eq. (4.98) gives,

$$\mathcal{E}r = e^{C_7}(x + C_0)^{C_5}, \tag{4.100}$$

for arbitrary C_7. Combining Eqs. (4.99) and (4.100), we obtain

$$\mathcal{E} = C_8 (x + C_0)^{C_5/2-1}, \tag{4.101}$$

$$r = C_9 (x + C_0)^{C_6/5+1}, \tag{4.102}$$

where

$$C_8 = {C_6}^{1/2} e^{C_7/2},$$

$$C_9 = {C_6}^{-1/2} e^{C_7/2}.$$

Note that $C_6 = 2$ recovers the special case of the quadratic tapering with homogeneous electrical properties discussed in §4.1.3.
In summary, we can acquire analytic solutions if either Eqs. (4.96) and (4.97) or (4.101) and (4.102) are satisfied for $r, \mathcal{E}$, respectively. The framework of sum-over-trips is thereby extended for a larger family of tapered dendrites.

4.3.2 Conformal quantum mechanics: a complementary

In §3.1.2 where we construct the framework of sum-over-trips, it is stated that a dendritic tree whose electro-physiology is described by a linear cable equation can be solved via the same approach, as long as the kernel, i.e. the Green's function on an infinite cable, is known.
Here we consider the dendritic radius following a power law, similar to Eq. (4.102), but for simplicity, we define

$$r(x) = r_0 \left[\frac{l-x}{l}\right]^{\nu} = r_0(1+ax)^{\nu}, \tag{4.103}$$

where ν and $a = -l^{-1}$ are arbitrary constants that charaterise the tapered structure. Note that $\nu = 0, 2$ recover the cylindrical and paraboloid cables, respectively.

On passive cables

Romero and Trenado [2015] proves that, for a passive dendritic branch whose morphology can be described by the power law Eq. (4.103), the passive cable equation with tapering is invariant under the conformal transformation. Hence, by introducing new variables,

$$\zeta = \frac{(1+ax)^{1-\nu/2}}{a(1-\nu/2)}, \tag{4.104}$$

$$V(\zeta;t) = \zeta^{-\frac{3\nu}{4(1-\nu/2)}} e^{-t/\tau} \Psi(\zeta;t), \tag{4.105}$$

Eq. (2.30) can be rewritten as

$$-\frac{\partial \Psi(\zeta;t)}{\partial t} = \hat{H}\Psi(\zeta;t), \tag{4.106}$$

given the assumption $[r'(x)]^2 \ll 1$.
Note Eq. (4.106) appears to be in the same form as a time-dependent one-dimensional Schrödinger equation for a non-relativistic free particle, where the Hamiltonian is defined to be

$$\hat{H} = -D_0 \frac{\partial^2}{\partial \zeta^2} + \frac{3\nu(5\nu-4)}{4(2-\nu)^2}\frac{D_0}{\zeta^2}. \tag{4.107}$$

where

$$D_0 = \frac{\lambda_0^2}{\tau}. \tag{4.108}$$

Although the transformation is not well defined for $\nu = 2$, we have discussed the case of quadratic tapering in §4.1.3, and Romero and Trenado [2015] studies this

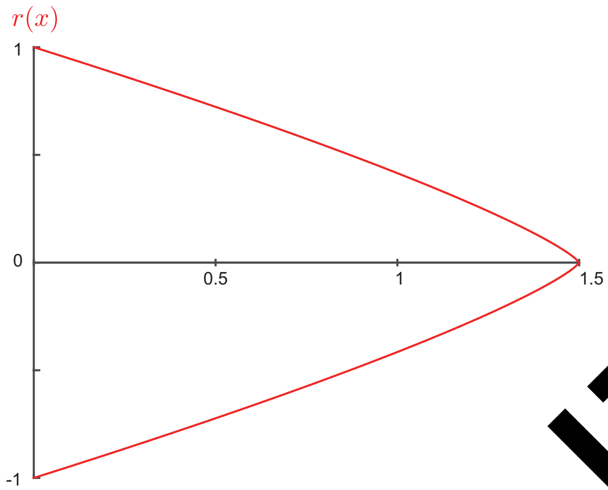

Figure 4.6: A tapered dendrite in a conical shape. The radius is defined by Eq. (4.103) with $\nu = 4/5$.

case separately with a different spatial parameterisation which is essentially the same as Eq. (4.25).

Other than $\nu = 0$ which recovers the cylindrical cases that we have discussed, $\nu = 4/5$ which represents a conical tapering (see Fig. 4.6) also reduces Eq. (4.106) to a heat equation.

For $\nu \neq 0, 4/5, 2$, Eq. (4.106) can be solved by separation of variables [Romero and Trenado, 2015], that is, by taking

$$\Psi(\zeta, t) = e^{-Et}\psi(\zeta), \tag{4.109}$$

we obtain

$$E\psi(\zeta) = \hat{H}\psi(\zeta), \tag{4.110}$$

which appears to be in the same form as a time-independent Schrödinger equation.

On resonant cables

By assuming zero initial data and $[r'(x)]^2 \ll 1$, the resonant cable equation with tapering in the Laplace frequency domain (2.58) is now reduced to

$$\mathcal{E}(\omega)V(\omega) = \frac{1}{2R_a r(x)}\frac{\partial}{\partial x}\left[r^2(x)\frac{\partial V(\omega)}{\partial x}\right] + I_0(\omega), \tag{4.111}$$

which, by change of variable Eq. (4.104), becomes

$$\mathcal{E}V = \frac{r_0}{2R_a}\left[\frac{\partial^2 V}{\partial \zeta^2} + \frac{3\nu}{2(1-\nu/2)}\frac{1}{\zeta}\frac{\partial V}{\partial \zeta}\right] + I_0. \tag{4.112}$$

Since we are now working in the frequency domain, instead of Ψ defined in Eq. (4.105), we introduce the new variable Ψ^* by

$$V(\zeta;t) = \phi_\zeta \Psi^*(\zeta;t), \tag{4.113}$$

where

$$\phi_\zeta = \zeta^{-\frac{3\nu}{4(1-\nu/2)}}, \tag{4.114}$$

or, equivalently, $\Psi^* = e^{-t/\tau}\Psi$, which reduces Eq. (4.112) to

$$\left[\frac{2R_a}{r_0}\mathcal{E} + \frac{3\nu(5\nu-4)}{4(2-\nu)^2}\frac{1}{\zeta^2} - \frac{\partial^2}{\partial \zeta^2}\right]\Psi^* = \frac{I_0}{\phi_\zeta}. \tag{4.115}$$

Note that the operator has the simliar structure to $\hat{H}$ in Eq. (4.107) and thus we have extended the method of Rome[illegible] and Tr[illegible]do [2015] from passive cables to resonant ones.
Additionally, we point out that the reparameterisations, ζ, Ψ^*, conducted here are essentially special cases of Z, V^* (up to a scale) introduced by Poznanski [1991], since the dendrtic radius is assumed to follow Eq. (4.103). It could also be checked that ϕ_ζ is indifferent from $\phi(Z)$ defined in Eq. (4.9). Therefore, we can directly incorporate the new case of $\nu =$ [illegible]$/5$ into the framework of sum-over-trips with tapering.

4.3.[illegible] General Green's functions: a summary

For various versions of cable equations, passive or resonant, cylindrical or tapered, we have consistently used the heat kernel, because after local coordinate tranformations, all the cable equations (2.29) - (2.33), with the certain constraints, reduce to the form of Eq. (3.21) or (4.32) and hence the reparameterised variables share the same underlying Green's function, which is simply an elementary function. Therefore, even though the cable equations can potentially be different from segment to segment, they can be integrated into the framework of sum-over-trips.

Location-dependent electrical properties

In order to obtain analytical solutions to Eqs. (3.16) and (4.15), we enforce the constraints that both γ take values independent of location,

$$\gamma_c^2(x;\omega) = \frac{1}{D}\left[\omega + \frac{1}{\tau} + \frac{1}{C(r_{res} + L_{res}\omega)}\right] = \frac{2R_a}{r_c}\mathcal{E}, \tag{4.116a}$$

$$\gamma_t^2(Z;\omega) = \tau\omega + \beta + \frac{R_m}{r_{res} + L_{res}\omega} = R_m[\mathcal{E} + (\beta - 1)g_l]. \tag{4.116b}$$

Note the difference between their definitions, and that we can recover the cylindrical γ_c by recognising $\beta(Z) = 1$ in γ_t and some rescaling, and that Eq. (4.115) reduces to the same structure as Eq. (4.116a) if $\nu = 0, 4/5$.
Recall that in §4.3 we have obtain several analytical solutions with $\mathcal{E}$ varying in x by the Cauchy-Euler equation. By the same approach, we would require $\gamma_c, \gamma_t \propto x^{-1}$. However, the leaky and axial resistivities $R_m = 1/g_l, R_a$ are not likely to vary along a dendritic branch, the cylindrical radius r_c is also a constant, and $\mathcal{E} = C\omega + g_l + (r_{res} + L_{res}\omega)^{-1}$ involves these constants as well (C the capacitance per area is also a constant). Therefore, it is quite unrealistic for the Cauchy-Euler equation to hold.
Nonetheless, $\mathcal{E}$ can be location-dependent in both the cases as it encodes information of resonant channels, which could have a heterogeneous distribution. It has been found in some pyramidal neurons that the density of I_h channels is varying linearly along the dendrites [].
Assume all the individual channels are identical, and that they are linearly distributed along a cylindrical cable for $x \geq 0$ where a soma (or a closed terminal) is at $x = 0$, that is, $g_h = r_{res}^{-1} = \rho_g(x - x_0), p_h = L_{res}^{-1} = \rho_p(x - x_0)$, for constants $x_0 \leq 0$ and $\rho_g, \rho_p > 0$, we thereby have, for Eq. (4.116a),

$$\mathcal{E}(x;\omega) = C\omega + g_l + \frac{\rho_g(x - x_0)}{1 + \omega\rho_g/\rho_p}, \tag{4.117}$$

which reduces Eq. (3.16) to the form of an Airy function [] whose Green's function can be found in terms of elementary and Airy functions [Vallée and Soares, 2010].
Mathematically, we can take the same approach for Eq. (4.116b) with $\mathcal{E}(Z;\omega)$ and obtain analytical Green's functions by Airy functions. However, as $\mathcal{E}(Z;\omega)$ is linear in Z, it is not linear in x unless we go back to the cylindrical cases.

General morphology and resonance

Given a homogeneous distribution of resonant channels, we can obtain analytical solutions only if the geometric ratio $F(Z)$ is one of the six types in Table 4.1, or the dendritic radius $r(x) = r_0(1 + ax)^{4/5}$. If $\nu \neq 0, 4/5, 2$ in Eq. (4.115), or more generally, if $\mathcal{E}$ is location-dependent, we cannot apply the heat kernel.
Nonetheless, as is stated in §3.1.2, any linear differential equation has Green's functions. For an arbitrary resonant cable equation with tapering, by the Laplace transform and assuming zero initial data, we can write Eq. (2.58) as

$$\mathcal{E}(x)V = \frac{1}{2R_a r(x)\sqrt{1+(r'(x))^2}} \frac{\partial}{\partial x}\left[r^2(x)\frac{\partial V}{\partial x}\right] + I_0(\omega), \tag{4.118}$$

where both the morphological parameter r and the electrical paramter $\mathcal{E}$ are generally dependent on location x. Differentiating the terms in the bracket, we obtain

$$\mathcal{E}(x)V = a(x)\left[2r'(x)\frac{\partial V}{\partial x} + r(x)\frac{\partial^2 V}{\partial x^2}\right] + I_0(\omega), \tag{4.119}$$

where

$$a(x) = \frac{1}{2R_a\sqrt{1+(r'(x))^2}}, \tag{4.120}$$

which can be reduced to

$$[\mathcal{E}\phi_v - 2ar'\phi'_v - r\phi''_v]v = ar\phi_v\frac{\partial^2 v}{\partial x^2} + I_0, \tag{4.121}$$

by introducing a change of variable,

$$V(x;\omega) = \phi_v(x)v(x;\omega), \tag{4.122}$$

and defining

$$\phi_v(x) = \frac{C}{r(x)}, \tag{4.123}$$

where C is an arbitrary constant.
Equivalently, Eq. (4.121) can be rewritten as

$$Hv = u, \tag{4.124}$$

where

$$H = \frac{\mathcal{E}r + 2ar' - 2}{ar^2} - \frac{\partial^2}{\partial x^2}, \tag{4.125}$$

$$u(x;\omega) = \frac{I_0}{C_0 a}. \tag{4.126}$$

The Green's function thus satisfies,

$$HG_v(x,y) = \delta(y-x), \tag{4.127}$$

and can be explicitly found by

$$G_v(x,y) = \sum_{n=0}^{\infty} \frac{\bar{g}_n(x) g_n(y)}{\mu_n} \tag{4.128}$$

where $g_n(x)$ are a set of eigenfunctions admitted by the linear operator H, whose complex conjugates are $\bar{g}_n(x)$, and μ_n are the corresponding eigenvalues.
However, in order to find g_n, μ_n, it is necessary to solve

$$Hg_n = \mu_n g_n, \tag{4.129}$$

for all n, which can be recognised as a Schrödinger equation. Note that the Hamiltonian,

$$H = \frac{\hat{p}^2}{2m} + V(x;t). \tag{4.130}$$

is the sum of the kinetic energy, i.e. the differential operator, and the potential energy $V(x;t)$. Since r is arbitrary due to Eq. (4.125), in general it does not admit analytical solutions.
Nonetheless, several special cases have been thoroughly studied in quantum mechanics, and their Green's functions are available for $V(x;t)$ being linear [Brown and Zhang, 1994; Tsaur and Wang, 2006], harmonic [Tsaur and Wang, 2006; Rother, 2017], centrifugal [Tsaur and Wang, 2006], or somehow more generally, conservative [Rother, 2017].
Whereas we could obtain Green's function for any linear cable equations, they admit either too complicated or implicit solutions that are not practically useful if no constraints are applied. Besides, their Green's functions are different, which means they cannot fit into the framework of sum-over-trips together, even though they can fit into the framework individually. In other words, for a dendritic tree with general tapering and resonance, the appraoch of sum-over-trips would work, only if the

cable equations on all branches are indifferent, which is apparently an unrealistic assumption.

Nevertheless, such models are applicable if the entire dendritic tree can be reduced to an equivalent single dendrite that is equipped with location dependent properties.

Chapter 5

Application and Discussion

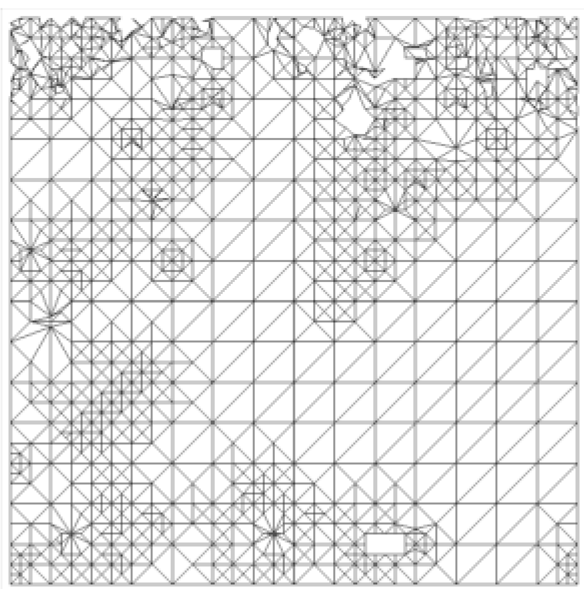

5.1 Preparations for computer simulations

In this chapter, we will take computational approaches based on the theoretical results discussed in all the previous chapters. All simulations are conducted with MATLAB. Here we first present the standard models, methods and measurements to be considered in this chapter.

5.1.1 Model

In order to study the funtions of different neuronal morphologies, structures and parameters of dendritic trees could be different from case to case. Nonetheless, we will only consider cylindrical and parabolic dendritic branches.
It has been discussed in §4.1.3 why the quadratic tapering, i.e. the Exponential type, but not other tapering structures is preferred. The shape of the parabolic dendrite is defined by Eq. (4.22) as

$$r(x) = r_0 \left[\frac{l - x}{l}\right]^2, \tag{5.1}$$

for $x \in [0, l_0]$, where $l_0 \leq l$ is the dendritic length, and r_0 is the initial dendritic radius. The choice of l_0 instead of l allows us to freely control the dendritic length when necessary.
We can thereby easily find the terminal radius r_1 by inserting l_0 in Eq. (5.1),

$$r_1 = r(l_0) = \left[\frac{l - l_0}{l}\right]^2. \tag{5.2}$$

If $l_0 = l$, the dendritic terminal radius is zero. Otherwise, the terminal radius is finite.
In practice, however, it is more straightforward to define a parabolic dendrite by specifying its length l_0 and intial and terminal radii r_0, r_1. We hence identify, from Eq. (5.2),

$$l = \frac{l_0}{1 - \sqrt{r_1/r_0}}, \tag{5.3}$$

which together with r_0 fully charaterises the parabola, and determines the geometric ratio.
In addition, we keep the values of other membrane parameters the same in different examples, unless otherwise specified.

5.1.2 Method

To calculate the response voltage profile in time, we first find the Fourier transform of the input $I_{\text{inj}}(t)$, and construct the Green's function $G(x, y; i\omega)$ by the method of local point matching, multiply them, and and finally take the inverse Fourier transform to obtain $V(x, y; t)$ (see §2.3.3).

Input currents

Whereas we can only find the Fourier transform of a general input by numerical approaches (e.g. the chirp current in Fig. 2.10 is obtained by the fast Fourier transform, the `fft` function in MATLAB), some idealised models of input can be transformed analytically, or by simply refering to a table of Laplace tranforms [Abramowitz and Stegun, 1964].
For instance, a step function in time domain,

$$I_{\text{step}}(t) = A_0 H(t - t_0), \tag{5.4}$$

appears exponential in the Laplace frequency domain

$$\bar{I}_{\text{step}}(\omega) = \frac{A_0}{\omega} e^{-t_0\omega}, \tag{5.5}$$

and the EPSC (2.15) becomes

$$\bar{I}_{\text{EPSC}}(\omega) = \frac{A_0}{(\omega + B_0)^2}. \tag{5.6}$$

Green's function

For an arbitrary dendritic tree, we can find the Green's function in algebraic expression by the method of local point matching following the steps in §3.2.3 and then substituting in numerical values. If all branches are cylindrical, the node factors are to be found in §3.1.2, and the spatial scaling parameter γ_c is defined by Eq. (3.17) as

$$\gamma_c^2(\omega) = \frac{1}{D}\left[\omega + \frac{1}{\tau} + \frac{1}{C(r_{res} + L_{res}\omega)}\right]. \tag{5.7}$$

If some of the dendritic segments are parabolic, the node factors are to be found in §4.2.3, and all spatial parameters are firtsly transformed by Eq. (4.25) as

$$Z(x) = \frac{3}{2K} \ln \frac{l - x}{l}, \tag{5.8}$$

and then scaled by γ_p which is defined in Eq. (4.16) as

$$\gamma_p^2(\omega) = \tau\omega + \beta(Z) + \frac{R_m}{r_{res} + L_{res}\omega}. \tag{5.9}$$

For the rest dendrites which are cylindrical, instead of Eq. (5.8), we directly use the definition (4.3), which gives

$$Z(x) = \frac{x}{\lambda}. \tag{5.10}$$

Note we can also use the framework for tapering for a dendritic tree with all cylindrical segments, but we prefer the original framework of sum-over-trips, because the cylindrical node factors are simpler than the tapering ones.
The steps to obtain the Green's function will be presented explicitly in the first example (see §5.2.1), while the detailed calculations will be similar for the other examples and thus omitted.
Whereas we can obtain $G(x, y; \omega)$ for all possible combinations of input and output locations, we will mainly consider somatic responses $G(x = x_{\text{soma}}, y; \omega)$ and responses at the input location $G(x = y, y; \omega)$.

5.1.3 Measurements

Other than directly showing plots of Green's functions and response profiles, the main measurements to be investigated are the voltage equilibria and the resonant frequencies. Given the Green's function, the voltage equilibrium can be easily found by Eq. (3.80). This measurement is mainly meaningful for passive neurons with step inputs, but it relates directly to the current transfer from input to output and thus characterises the strength of a response, even for a resonant system.
The resonant dynamics can be characterised by the two resonant frequencies, the preferred frequency Ω^* and the natural frequency $\bar{\Omega}^*$, because the real part of the (complex) frequency in the Laplace domain characterises the transient behaviours, and the imaginary part characterises the periodic behaviours of a resonant system. The two frequencies can be both understood roughly as the frequencies where the Green's function reaches its largest amplitude. Ω^* is defined on the real frequency axis of the Laplace domain, which can be obtained as a solution of the implicit equation, for $\omega \geq 0$,

$$\frac{\partial G(x, y; \omega)}{\partial \omega} = 0, \tag{5.11}$$

while the natural frequency $\bar{\Omega}^*$ is defined on the imaginary axis of the Laplace domain, i.e. the real axis of the Fourier domain, which maximises the modulus of

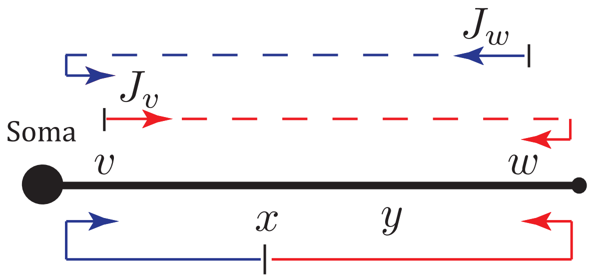

Figure 5.1: A schematic of a neuron with a soma and a single dendrite. Terms of Eq. (5.13a) are shown by blue arrows, terms of Eq. (5.13b) are shown by red arrows.

the Green's function, that is, for $\omega \geq 0$.

$$\frac{\partial |G(x, y; i\omega)|}{\partial \omega} = 0. \tag{5.12}$$

5.2 Results of simplified models

5.2.1 Single neuron with a single dendritic cable

Here we consider a model of a single dendritic branch, whose left end ($x = 0$) is attached to a lumped soma and whose right end ($x = l_0$) is a closed terminal (see Fig. 5.1).

Cylindrical dendrite

In this case, by the method of local point matching, a system of linear equations for J_v and J_w corresponding to a pair of points (v, w) takes the following form,

$$J_v = [J_w f(\gamma_c l_0) + f(\gamma_c x)](2p_{\mathrm{S},c} - 1), \tag{5.13a}$$

$$J_w = J_v f(\gamma_c l_0) + f(\gamma_c (l_0 - x)), \tag{5.13b}$$

where p_{S} can be found from Eq. (4.65).

Solving the linear system (5.13) we can find that

$$J_v = \frac{(2p_{\mathrm{S},c} - 1)[f(\gamma_c(2l_0 - x)) + f(\gamma_c x)]}{1 - (2p_{\mathrm{S},c} - 1) f(2\gamma_c l_0)}, \tag{5.14a}$$

$$J_w = \frac{(2p_{\mathrm{S},c} - 1) f(\gamma_c(l_0 + x)) + f(\gamma_c(l_0 - x))}{1 - (2p_{\mathrm{S},c} - 1) f(2\gamma_c l_0)}, \tag{5.14b}$$

and by

$$J_y = J_v f(\gamma_c y) + J_w f(\gamma_c (l - y)) + f(\gamma_c |x - y|), \tag{5.15}$$

we can obtain the Green's function in the Laplace domain by Eq. (3.56).
It can be checked that the solution is equivalent to that in the form of an infinite series obtained by directly applying the sum-over-trips method [Timofeeva and Coombes, 2014].

Parabolic dendrite

By the method of local point matching, the linear system can be found as

$$J_v = [J_w f(\gamma_p Z(l_0)) + f(\gamma_p Z(x))](2p_{\mathrm{S},p} - 1), \tag{5.16a}$$

$$J_w = [J_v f(\gamma_p Z(l_0)) + f(\gamma_p Z(l_0 - x))](2p_{\mathrm{C},p} - 1), \tag{5.16b}$$

which is similar to the system (5.13) but with several modifications.
Solving the system (5.16) we obtain,

$$J_v = \frac{(2p_{\mathrm{S},p} - 1)\left[\left(\frac{l-l_0+x}{l}\frac{l-l_0}{l}\right)^{-3\gamma_p/2K}(2p_{\mathrm{C},p} - 1) + \left(\frac{l-x}{l}\right)^{-3\gamma_p/2K}\right]}{1 - (2p_{\mathrm{S},p} - 1)(2p_{\mathrm{C},p} - 1)\left(\frac{l-l_0}{l}\right)^{-3\gamma_p/K}}, \tag{5.17a}$$

$$J_w = \frac{(2p_{\mathrm{C},p} - 1)\left[\left(\frac{l-x}{l}\frac{l-l_0}{l}\right)^{-3\gamma_p/2K}(2p_{\mathrm{S},p} - 1) + \left(\frac{l-l_0+x}{l}\right)^{-3\gamma_p/2K}\right]}{1 - (2p_{\mathrm{S},p} - 1)(2p_{\mathrm{C},p} - 1)\left(\frac{l-l_0}{l}\right)^{-3\gamma_p/K}}, \tag{5.17b}$$

and by

$$J_y = J_v f(\gamma_p Z(y)) + J_w f(\gamma_p Z(l_0 - y)) + f(\gamma_p Z(|x - y|)), \tag{5.18}$$

we can obtain the Green's function in the Laplace domain by Eq. (4.70).

Somatic response

If the output is measured at the soma, i.e. $x = 0$, the Green's functions can be found as

$$G_c(0, y) = \frac{p_{\mathrm{S},c}[\exp(-\gamma_c y) + \exp(\gamma_c y - 2\gamma_c l_0)]}{z_c[1 - (2p_S - 1)\exp(-2\gamma_c l_0)]}, \tag{5.19a}$$

$$G_p(0, y) = \frac{p_{\mathrm{S},p}\left[\left(\frac{l-y}{l}\right)^{-3\gamma_p/2K} + (2p_{\mathrm{C},p} - 1)\left(\frac{l-l_0}{l}\frac{l-l_0+y}{l}\right)^{-3\gamma_p/2K}\right]}{z_p(y)\left[1 - (2p_{\mathrm{S},p} - 1)(2p_{\mathrm{C},p} - 1)\left(\frac{l-l_0}{l}\right)^{-3\gamma_p/K}\right]}\left(\frac{l-y}{l}\right)^{3/2}. \tag{5.19b}$$

For comparison between the cylindrical and parabolic cases, we simplify the parabolic model by assuming $l_0 = l$, which gives,

$$G_c(0, y; \omega) = \frac{1}{z_c \tanh \gamma_c l + z_{\mathrm{S}}} \frac{\cosh \gamma_c (l - y)}{\cosh \gamma_c l}, \tag{5.20a}$$

$$G_p(0, y; \omega) = \frac{p_{\mathrm{S},p}}{z_p(y)} \left[\frac{l - y}{l} \right]^{3/2 - 3\gamma_p/2K}. \tag{5.20b}$$

We can then easily obtain the Green's functions in the case of semi-infinite dendritic cables from Eq. (5.19), that is,

$$\lim_{l \to \infty} G_p(0, y; \omega) = \lim_{l \to \infty} G_c(0, y; \omega) = \frac{2 p_{\mathrm{S},c}}{z_c} \exp(-\gamma_c y), \tag{5.21}$$

given that all electrical parameters, the somatic radii and the starting radii of the dendritic cables are identical in both the cylindrical and parabolic models. Note that the limit of $G_p(0, y; \omega)$ in Eq. (5.21) can be checked algebraically, but it is more heuristic to consider that the parabola asymptotically becomes a cylinder as $K \to 0$.

In the opposite case when the dendritic length is extremely short, it is straightforward to see that

$$\lim_{l \to 0} G_p(0, 0; \omega) = \lim_{l \to 0} G_c(0, 0; \omega) = \frac{1}{z_{\mathrm{S}}}, \tag{5.22}$$

which is exactly the system of a single soma.

For intermediate dendritic length which varies in the realistic range, we plot the resonant frequencies as functions of dendritic length according to the somatic input impedance for the two models in Fig. 5.2. The two curves are considerably close when the dendritic length is either small or large, so the two models are to behave similarly, as predicted by the two limits of l in Eqs. (5.21) and (5.22).

However, the two pairs of curves are quite away from each other around $l = 150$ μm, which implies the two models behave differently; as we can see from the somatic voltage profiles in response to the same chirp stimulus in Fig. 5.3, the tapering structure does not only affect the strength of the signal, but also the arrival time of the peak, i.e. the phase of signal.

Now we consider a more realistic input modelled by the idealised EPSC defined by Eq. (2.15). It can be clearly see from Fig. 5.4A that the difference between two models are minor when the dendritic length is either small or large, and there is a noticeable gap in the peak amplitudes for $l = 150$ μm.

The peaks arrival times of the two models seem not distinguishable in the case of a single EPSC, but if we apply a train of EPSCs with succesive time gap of 10 ms, such

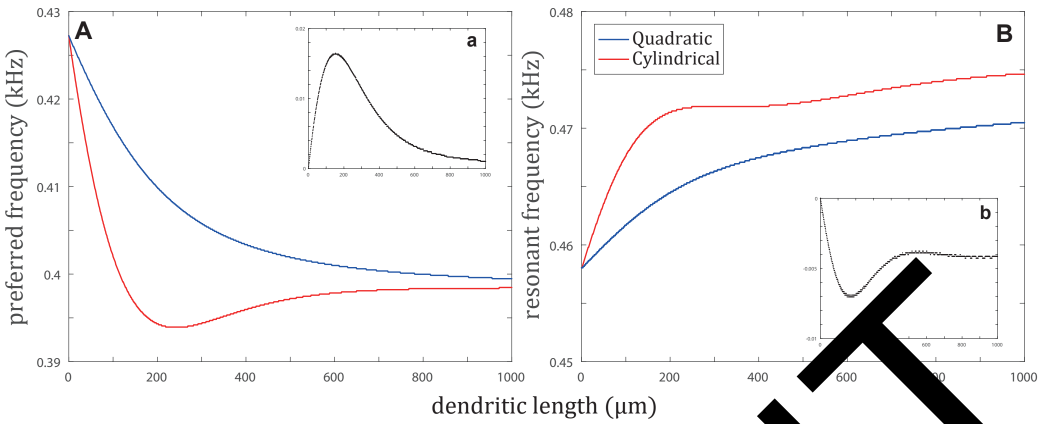

Figure 5.2: Resonant frequencies vary with respect to the dendritic lengths in the cylindrical (red) and parabolic (blue) models, for (**A**) preferred frequencies Ω^* and (**B**) natural frequencies $\bar{\Omega}^*$, nested in which (**a**) and (**b**) are the differences between the two models. Dendritic parameters: $r = 1$ μm for the cylindrical model while $r_0 = 1$ μm and $r_1 = 0$ μm for the tapering model; additionally, $C_m = 1$ μF·cm^{-2}, $R_m = 2000$ Ω·cm^2, $R_a = 100$ Ω·cm, $r_{\text{res}} = 100$ Ω·cm^2 and $L_{\text{res}} = 5$ H·cm^2 are the same for both the models. Somatic parameters: $r_S = 12.5$ μm, $C_{\text{soma}} = 1$ μF·cm^{-2}, $R_{\text{soma}} = 2000$ Ω·cm^2, $r_{\text{soma}} = 100$ Ω·cm^2, $L_{\text{soma}} = 5$ H·cm^2.

difference in peak arrivals (due to the different phases) could cause the two models to reach global maxima at two peaks (see Fig. 5.4B). In the case that the difference occurs near the threshold of any nonlinear behaviour, e.g. an IF model (see §2.2.2), such small differences could lead to entirely different neuronal computation and, furthermore, different emergent network behaviours.

Input impedance

The input impedance can be found for $x = y$,

$$G_c(y, y) = \frac{[1 + (2p_{S,c} - 1)\exp(-2\gamma_c y)][1 + \exp(-2\gamma_c(l - y))]}{2z_c[1 - (2p_{S,c} - 1)\exp(-2\gamma_c l)]}, \tag{5.23a}$$

$$G_p(y, y) = \frac{(2p_{S,p} - 1)\left(\frac{l-y}{l}\right)^{3\gamma_p/K} + (2p_{C,p} - 1)\left(\frac{y}{l}\right)^{3\gamma_p/K} + 1}{2z_p(y)}, \tag{5.23b}$$

with the assumption $l_0 = l$ again which reduces the parabolic model with the zero ending radius.

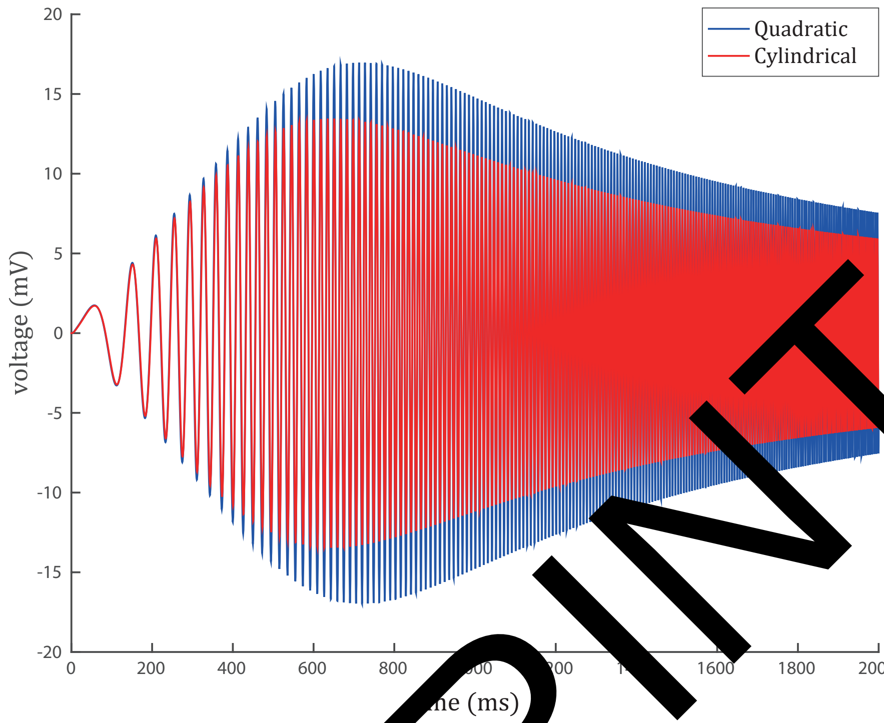

Figure 5.3: Somatic voltage response to a chirp input at soma with $\omega_{\text{chirp}} = 0.0003$ kHz and $A_{\text{chirp}} = 0.2$ nA, for the case $l = 150$ μm about where the differences between the two resonant frequencies are the largest.

Voltage attenuation

The voltage attenuation from an injected location to the soma is defined by Koch [1984] as

$$A_V(y;\omega) = \left| \frac{G(0,y;\omega)}{G(y,y;\omega)} \right|, \tag{5.24}$$

by which we obtain

$$A_{V,c}(y) = \frac{2p_{\mathrm{S},c}}{\exp(\gamma_c y) + (2p_{\mathrm{S},c} - 1)\exp(-\gamma_c y)}, \tag{5.25a}$$

$$A_{V,p}(y) = \frac{2p_{\mathrm{S},p}\left(\frac{l-y}{l}\right)^{3/2-3\gamma_p/2K}}{(2p_{\mathrm{S},p} - 1)\left(\frac{l-y}{l}\right)^{3\gamma_p/K} + (2p_{\mathrm{C},p} - 1)\left(\frac{y}{l}\right)^{3\gamma_p/K} + 1}. \tag{5.25b}$$

5.2.2 Single neuron with a compartmental dendrite

Here we consider a model of a single neuron similar to that in §5.2.1, but its dendritic branch is fixed in length and compartmentalised into N successive cylinders

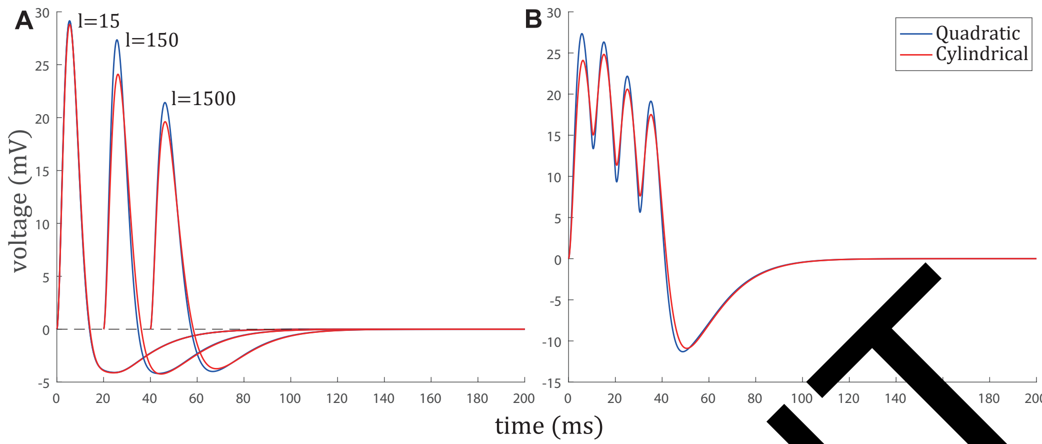

Figure 5.4: Somatic voltage responses to EPSCs at soma. A. Voltage profiles on the three models with dendritic lengths of 15, 150 and 1500 μm, respectively, to a single EPSC. B. Voltage profiles on the model with dendritic length of 150 μm to a train of four EPSCs with successive time gap of 10 ms.

whose lengths are the same but radii are different. Such compartmentalisation can be commonly seen in computational works considering tapering [Cuntz et al., 2007]. In order to compare with the parabolic model in §5.2.1, we assume the compartmental model shares the same electrical parameters as in the parabolic one. At the same time, the radii of the successive cylinders are chosen to be

$$r_c(i) = \frac{r_m(i) + r_M(i) + \sqrt{r_m(i) r_M(i)}}{3}, \tag{5.26}$$

where

$$r_m(i) = r\left(\min_{x \in \Delta_i}(x)\right), \tag{5.27a}$$

$$r_M(i) = r\left(\max_{x \in \Delta_i}(x)\right), \tag{5.27b}$$

and Δ_i is the segment of compartment $i \in \{1, 2, 3, \ldots, N\}$.

Eq. (5.26) ensures the total membrane areas in the two models are exactly the same, and the cylinders approximately tracks the dendritic shape of the quadratic tapering with a succesive decrease in their radii (see Fig. 5.5A). This compartmental model is motivated by the fact that the dendritic membrane plays an important role in signal filtration. Note the model is reduced to the cylindrical model when $N = 1$, but its radius it not chosen to be the same as the starting radius as the parabolic model as in §5.2.1.

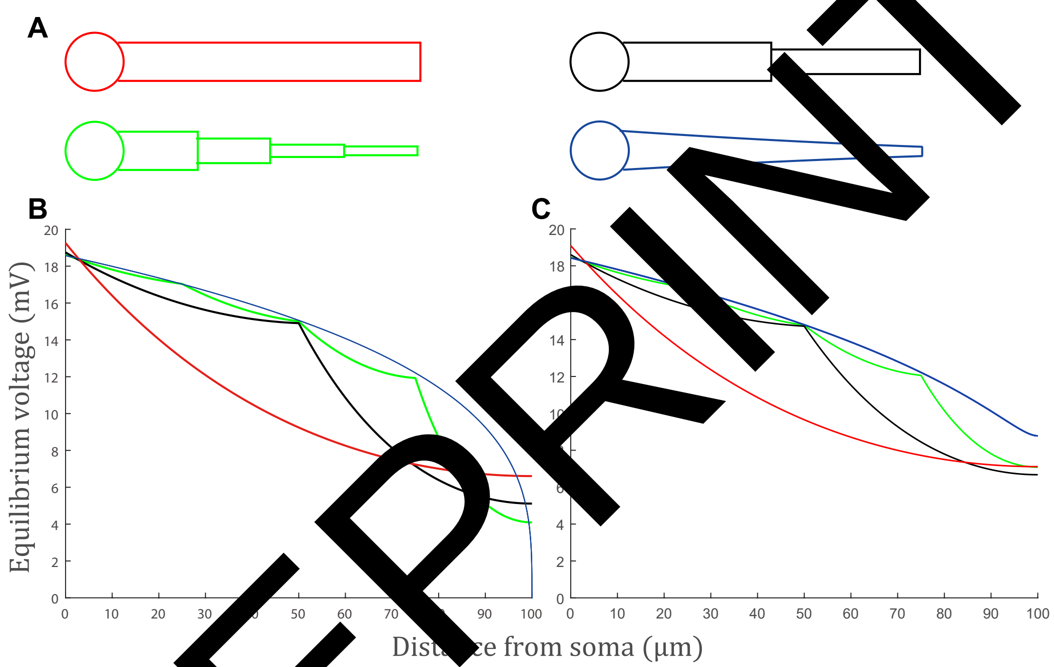

Figure 5.5: (**A**) Schematic shapes of the compartmental models with $N = 1$ (red), 2 (black), 4 (green), and the parabolic model (blue). All the models are purely passive here, i.e. $r_{\text{res}} = r_{\text{soma}} \to \infty$. Other paramters and morphology are the same as the parabolic model in Figure 5.2 except for $l = 100$ μm and $R_a = 1000$ Ω·cm. (**B** & **C**) Somatic response at equilibrium as a function of input location, where $r_1 = 0$ μm in (B) but $r_1 = 0.01$ μm in (C).

Dendrite with zero terminal radius

In Figure 5.5B, we plot the somatic responses at equilibrium ($t \to \infty$) of a purely passive neuron by a step input at different locations. When $N = 1$, we can clearly see a large range that the parabolic model yields a higher voltage equilibrium than the cylindrical model, as is proven by Bird and Cuntz [2016] for a single dendritic branch.

When $N > 1$, we can further observe the same phenomena on each local segment, as the compartmental curve are convex piece-wisely on individual compartments, and the voltages at the both ends of the segments are equal to those on the parabolic concave curve. Therefore, the property of optimal current transfer of quadratic tapering is seemingly a local property and thus works on individual tapered dendritic segments regardless of the global morphology.

We have also verified that when N is large (e.g. $N = 100$), the compartmental model becomes indistinguishable from the parabolic one. However, considering computational expenses, a tapered dendrite is usually partitioned into only a few segments ($N < 10$) Cuntz et al. [2007]. Hence, with a small number of compartments, the cylindrical model badly approximates the parabolic model as it is believed.

Note in Fig. 5.5B the voltage of the parabolic model reaches 0 when $y = l$, which can be easily seen from Eq. (5.20b), while that of the cylindrical model never does (unless $N \to \infty$). This phenomena can be easily understood as we have assumed zero radius at the terminal, which leads to infinitely large input resistence. We must point out that, in such models with realistic parameters, the point where the voltage of the parabolic model becomes smaller than that of the cylindrical model always occurs when the dendritic radius is considerably small (at the scale of nm in Fig. 5.5B), which is thinner than cell membrane. This is apparently unrealistic and is considered merely a mathematical result.

Nonetheless, moving the input away from the terminal, we can still observe a large range ($y >$ 50 μm) of the voltage attenuation ratio (5.25) of the parabolic model starting at almost zero (see Fig. 5.6), while the voltage responses of the parabolic model are larger than those of the cylindrical one (see Fig. 5.5B). Therefore, we can conclude that the somatic response of the cylindrical model will be greater given the same size of EPSPs at the same input location, while that of the quadratic model will be larger due to same strength of EPSCs.

By the definition of the voltage attenuation ratio (5.25), we can additionally infer that the input resistence is higher in the region close to the terminal end than the region close to the somatic end. The results are consistent with the simulations on neurons with real morphology [Kubota et al., 2011].

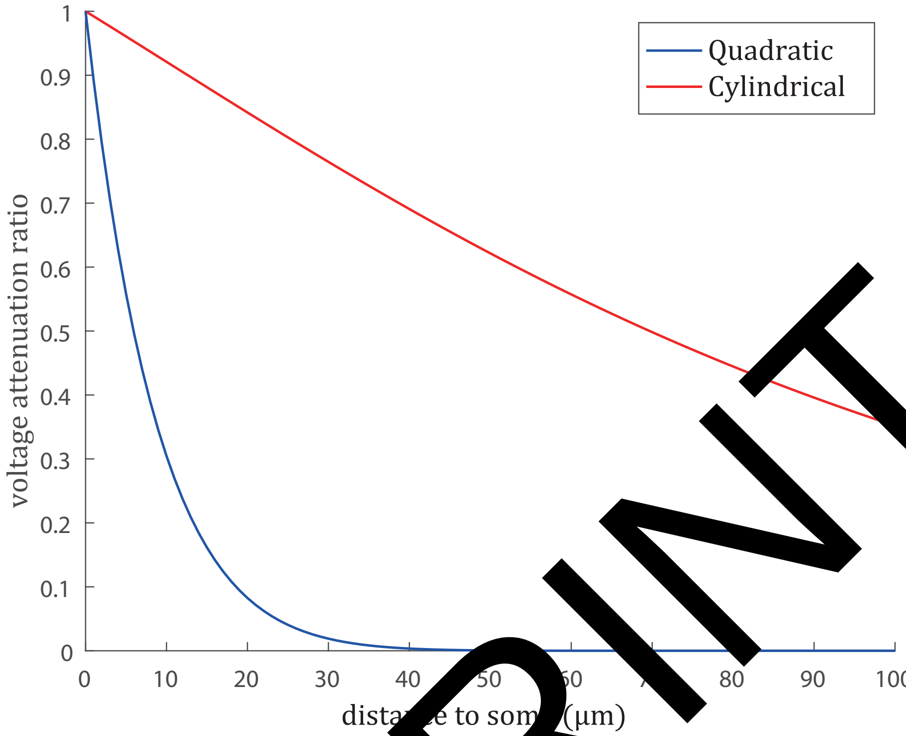

Figure 5.6: Voltage attenuation as a function of input location. All the parameters are the same as in Fig. 5.5B.

Dendrite with finite terminal radius

Here we consider a more realistic parabolic model with $r_1 = 0.01$ µm, and plot Fig. 5.5C. The voltage of the parabolic model exhibits no more drastic slump near the terminal and remains larger than that of the compartmental models.
However, we can still observe differences between the parabolic model and the compartmental models with small N. If we approximate the parabolic model by the compartmental model with fixed N, the error is ignorable in the thicker segments, but noticeable in the thinner segments, which suggests that it is more economic for computational works to discretise a tapered branch more dense near its terminal.

5.2.3 Single neuron with a 'Y'-shaped dendritic tree

Here we consider two neuronal models of a simple 'Y'-shape, whose dendritic tree consists of one primary dendrite and two identical branched dendrites. The dendrites are connected at the branching point (where we assume $x = 0$) and at the other end of the primary dendrite the same lumped soma are attached (see Fig. **??**). The two branched dendrites are modelled by either two identical parabolas, or two identical cylinders, so that we can see the effects of the global morphology more clearly. The primary dendrite is a cylinder with $r_c = r_0$ in either the model.

Identify the node factors by the rules of sum-over-trips

Firstly, at the soma, we have

$$A^S_{00} = 2p^S_0 - 1, \tag{5.28}$$

where

$$p^S_0 = \frac{\gamma_0 \theta^S_0}{\Gamma^S_0 \theta^S_0 + z_S}, \tag{5.29}$$

with

$$\theta^S_0 = \frac{1}{\lambda^S_0 r^S_{a,0}}, \tag{5.30a}$$

$$\Gamma^S_0 = \gamma_0 + K_0. \tag{5.30b}$$

Secondly, at the branching point, we have

$$A^b_{00} = 2p^b_0 - 1, \tag{5.31a}$$

$$A^b_{11} = A^b_{22} = 2p^b_1 - 1, \tag{5.31b}$$

$$A^b_{01} = A^b_{02} = 2p^b_1 \Phi_{01}, \tag{5.31c}$$

$$A^b_{10} = A^b_{20} = 2p^b_0 \Phi_{10}, \tag{5.31d}$$

$$A^b_{21} = A^b_{12} = 2p^b_1, \tag{5.31e}$$

where

$$\Phi_{10} = \Phi^{-1}_{01} = \frac{\phi^b_0}{\phi^b_1} = \left[\frac{\lambda^b_0}{\lambda^b_1}\right]^{\frac{1}{2}}, \tag{5.32}$$

and

$$p^b_0 = \frac{\gamma_0 \theta^b_0}{\Gamma^b_0 \theta^b_0 + 2\Gamma^b_1 \theta^b_1}, \tag{5.33a}$$

$$p^b_1 = \frac{\gamma_1 \theta^b_1}{\Gamma^b_0 \theta^b_0 + 2\Gamma^b_1 \theta^b_1}, \tag{5.33b}$$

in which θ^b_0, θ^b_1 are similarly defined as θ^S_0 in Eq. (5.30a) with their local parameters, and

$$\Gamma^b_0 = \gamma_0 - K_0, \tag{5.34a}$$

$$\Gamma^b_1 = \gamma_1 + K_1, \tag{5.34b}$$

Finally, at the two closed terminals in the end of the branched dendrites, we have

$$A_{11}^{c} = \frac{2\gamma_1}{\Gamma_1} - 1, \tag{5.35}$$

where

$$\Gamma_1 = \gamma_1 - K_1. \tag{5.36}$$

Find the Green's function by the method of local point matching

With the output $x = -L_0$ locating at the soma and closed terminals, we have

$$J_a = J_b f(L_0) A_{00}^{S} + f(0) A_{00}^{S}, \tag{5.37a}$$
$$J_b = J_a f(L_0) A_{00}^{b} + f(L_0) A_{00}^{b} + J_d f(L_1) A_{10}^{b} + J_e f(L_2) A_{20}^{b}, \tag{5.37b}$$
$$J_c = J_a f(L_0) A_{01}^{b} + f(L_0) A_{01}^{b} + J_d f(L_1) A_{11}^{b} + J_e f(L_2) A_{21}^{b}, \tag{5.37c}$$
$$J_d = J_c f(L_1) A_{11}^{c}, \tag{5.37d}$$

and J_e, J_f are omitted since identical branches are assumed, for $L_0 = \gamma_0 Z_0(l_0), L_1 = \gamma_1 Z_1(l_1)$.
Equivalently, the linear system (5.37) can be rewritten in the matrix form as,

$$\begin{bmatrix} -1 & f(L_0)A_{00}^{S} & 0 & 0 \\ f(L_0)A_{00}^{b} & -1 & 0 & 2f(L_1)A_{10}^{b} \\ f(L_0)A_{01}^{b} & 0 & -1 & f(L_1)[A_{11}^{b} + A_{21}^{b}] \\ 0 & 0 & f(L_1)A_{11}^{c} & -1 \end{bmatrix} \begin{bmatrix} J_a + 1 \\ J_b \\ J_c \\ J_d \end{bmatrix} = \begin{bmatrix} -(A_{00}^{S} + 1) \\ 0 \\ 0 \\ 0 \end{bmatrix}. \tag{5.38}$$

We can thus solve the J's by matrix inversion and compute J_y by

$$J_y = \begin{cases} [J_a + 1] f(L_y) + J_b f(L_0 - L_y), & \text{for } 0 \le y \le l_0, \\ J_c f(L_{y-l_0}) + J_d f(L_1 - L_{y-l_0}), & \text{for } l_0 < y \le l_0 + l_1. \end{cases} \tag{5.39}$$

where $L_y = \gamma_0 Z_0(x_0), L_{y-l_0} = \gamma_1 Z_1(y - l_0)$, which then gives the Green's function.

Somatic responses

In Fig. 5.7A, we plot the somatic responses at equilibrium with different lengths of the primary dendrite, based on the calculation in the previous sections. We can see that, despite of the voltage change in different cases, the signals are locally larger in the parabolas than in the cylinders for a wide range.
We can also set the primary dendrite to be parabolic but the branched dendrites

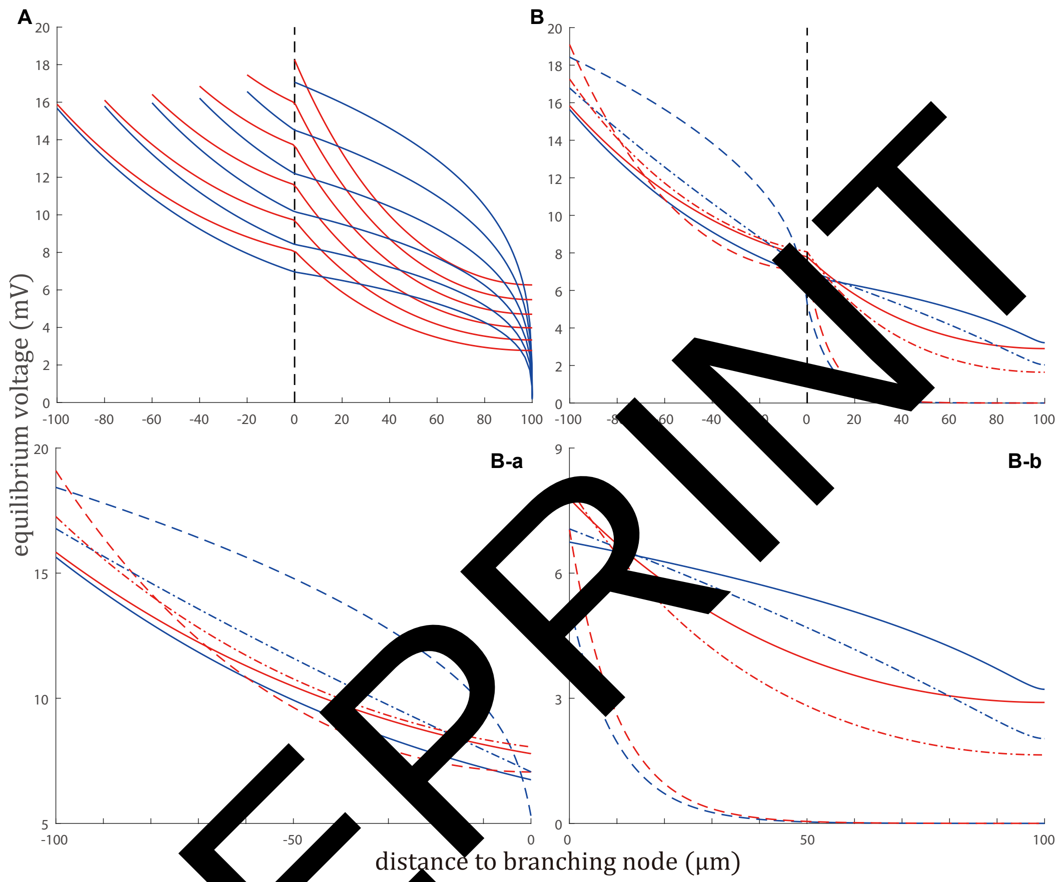

Figure [illegible]: Somatic response at equilibrium as a funtion of input location on a 'Y'-shaped dendritic tree. (**A**) The two identical branched segments are exactly the same as in Figure 5.5B in either the parabolic or the cylindrical case, but they are now attached to a cylindrical primary dendrite with the other end attached to the soma. The radius of the primary dendrite is $r_0 = 1$ μm and the length is 0, 20, 40, 60, 80 and 100 μm, respectively in the six different cases. The soma is attached at the other root of the primary dendrite. All other parameters are the same as in Fig. 5.5B. (**B**) All segments are parabolic. $r_0 = 1$ μm and $r_1 = 0.01$ μm are fixed, while the radius at the branching node $r_b = 1$ (solid), 0.5 (dotted) and 0.01 (dashed). Other parameters are unchanged from (A). (**B-a** & **B-b**) Zoomed-in plots of (B) for (a) on the primary dendrite and (b) on the branched dendrits.

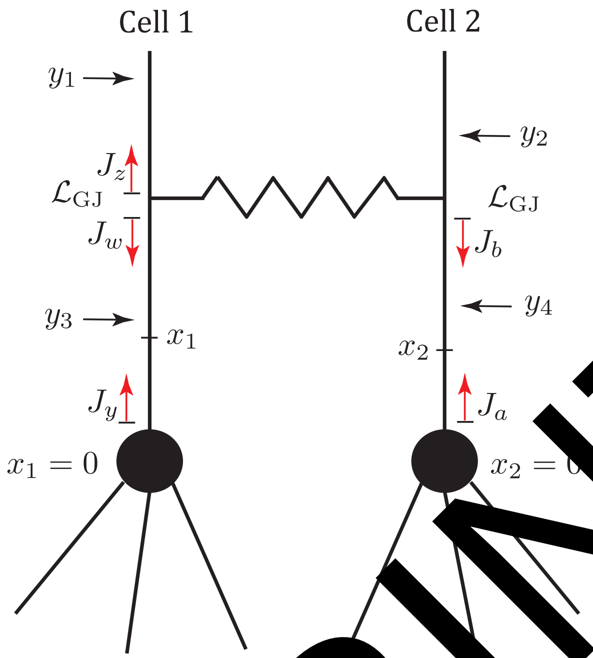

Figure 5.8: A schematic of a two-cell simplified network coupled by a gap junction.

cylindrical, which yields opposite results that such neuron amplifies proximal signals (see dashed curves in Fig. 5.7B).

In fact, by fixing $r_0 = 1$ µm (the initial dendritic radius at $x = -100$ µm) and $r_1 = 0.01$ µm (the terminal dendritic radius at $x = 100$ µm) and varying r_b (the dendritic radius at the branching node at $x = 0$ µm) in the range between r_0, r_1, we observe the blue curve deforming from convex for $r_b \sim r_0$ (the primary dendrite is almost a cylinder) eventually to concave for $r_b \sim r_1$ (the branched dendrites are almost cylinders). We can therefore confidently conclude that the optimal current transfer property of the quadratic tapering is quite local a property, whereas Bird and Cuntz [2016] had only proven it for a single branch of dendrite.

It is also interesting to mention that, with intermediate values of r_b (e.g. the dotted line in Fig. 5.7B), both the primary and the branched dendrites are quite tapered, which leads to larger signals in either the proximal or the distal dendrites, comparing to the cylindrical model.

5.2.4 Two simplified neurons coupled by a gap junction

Here we consider a simplified two-cell network. The two neurons are coupled by a dendro-dendritic gap junction (see Fig. 5.8). For simplicity, all dendritic branches are considered cylindrical and semi-infinite.

Identical neurons

We start by considering a model of two identical cells, either of which consists of a soma and N dendritic branches. We assume that the biophysical properties of all dendritic segments are the same and that the physical lengths are scaled by the characteristic function $\gamma(\omega)$. The gap junction is located at some distance $\mathcal{L}_{\rm GJ}$ away from the somata. We assume that this network can receive stimuli in four different locations mimicking distal (y_1 and y_2) and proximal (y_3 and y_4) inputs. Points of output x_1 (for neuron 1) and x_2 (for neuron 2) are located between either the soma and the gap junction.
By the method of local point matching we can construct a linear system of algebraic equations for the functions J_a, J_b, J_y and J_w in the case of placing output at x_2 (see Fig. 5.8),

$$J_a = J_b f(\mathcal{L}_{\rm GJ})(2p_{\rm S}-1) + f(x_2)(2p_{\rm S}-1), \tag{5.40a}$$

$$J_b = J_y f(\mathcal{L}_{\rm GJ})p_{\rm GJ} + J_a f(\mathcal{L}_{\rm GJ})(-p_{\rm GJ}) + f(\mathcal{L}_{\rm GJ}+x_2)(-p_{\rm GJ}), \tag{5.40b}$$

$$J_y = J_w f(\mathcal{L}_{\rm GJ})(2p_{\rm S}-1), \tag{5.40c}$$

$$J_w = J_y f(\mathcal{L}_{\rm GJ})(-p_{\rm GJ}) + J_a f(\mathcal{L}_{\rm GJ})p_{\rm GJ} + f(\mathcal{L}_{\rm GJ}+x_2)p_{\rm GJ}. \tag{5.40d}$$

This system of equations can be solved algebraically by hand [Yihe and Timofeeva, 2016]. The Green's functions for four individual inputs for neuron 2 are

$$G_2(x_2,y_1) = \frac{1}{2z}\frac{p_{\rm GJ}+p_{\rm GJ}a_0}{q_0}\bar{F}(x_2,y_1), \tag{5.41a}$$

$$G_2(x_2,y_2) = \frac{1}{2z}\frac{1-p_{\rm GJ}+p_{\rm GJ}a_0}{q_0}\bar{F}(x_2,y_2), \tag{5.41b}$$

$$G_2(x_2,y_3) = \frac{1}{2z}\frac{p_{\rm GJ}f(2\mathcal{L}_{\rm GJ})}{q_0}\bar{F}(x_2,0)\bar{F}(y_3,0), \tag{5.41c}$$

$$G_2(x_2,y_4) = \begin{cases} \frac{1}{2z}\left[\bar{F}(x_2,y_4) - \frac{p_{\rm GJ}f(2\mathcal{L}_{\rm GJ})}{q_0}\bar{F}(x_2,0)\bar{F}(y_4,0)\right], \text{if } x_2 < y_4, \\ \frac{1}{2z}\left[\bar{F}(y_4,x_2) - \frac{p_{\rm GJ}f(2\mathcal{L}_{\rm GJ})}{q_0}\bar{F}(x_2,0)\bar{F}(y_4,0)\right], \text{if } x_2 > y_4. \end{cases} \tag{5.41d}$$

where

$$a_0 = (2p_{\rm S}-1)f(2\mathcal{L}_{\rm GJ}), \tag{5.42}$$

$$q_0 = 1 + 2p_{\rm GJ}a_0, \tag{5.43}$$

$$\bar{F}(x,y) = f(x+y)(2p_{\rm S}-1) + \frac{f(y)}{f(x)}. \tag{5.44}$$

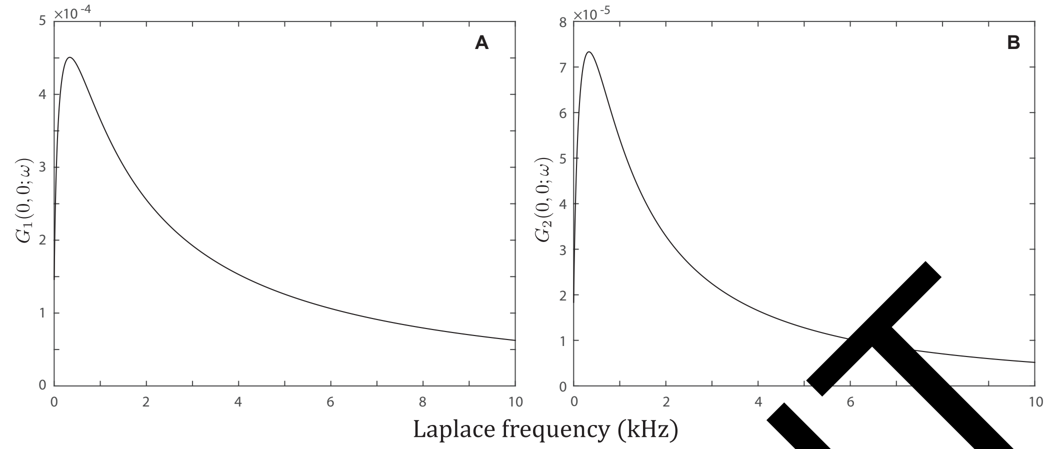

Figure 5.9: The somatic Green's function in the Laplace domain when input is placed at $y_3 = 0$, for (**A**) Cell 1 and (**B**) Cell 2. Biophysical parameters of the cells' membrane are the same as in Fig. 5.2. Gap-junctional parameters: $\mathcal{L}_{\mathrm{GJ}} = 50\,\mu$m, $R_{\mathrm{GJ}} = 100\,\mathrm{M}\Omega$.

Since the neurons are identical, the corresponding Green's functions for neuron 1 can be easily obtained from Eq. (5.44) by the symmetry of the input locations.
In Fig. 5.9 we plot the Green's functions at the soma of each cell ($x_1 = 0$ and $x_2 = 0$) in response to a stimulus $y_3 = 0$ applied to Cell 1. Note that Eqs. (5.41a) and (5.41b) are equivalent to the solutions for the Green's functions in the form of an infinite series found using the 'method of words' in Timofeeva et al. [2013].

Symmetric inputs

If two distal inputs y_1 and y_2 are applied at equal distances from each soma ($y_1 = y_2 > \mathcal{L}_{\mathrm{GJ}}$), the Green's function for each soma is identical. We obtain

$$G_1(0,y_1) + G_1(0,y_2) = G_2(0,y_1) + G_2(0,y_2) = \frac{\bar{F}(0,y_1)}{2z} = \frac{p_{\mathrm{S}} f(y_1)}{z}. \tag{5.45}$$

Similarly, for the case of two proximal inputs y_3 and y_4 placed at the same distance away from each soma ($y_3 = y_4 < \mathcal{L}_{\mathrm{GJ}}$), the somatic Green's function for each cell has the same form:

$$G_1(0,y_3) + G_1(0,y_4) = G_2(0,y_3) + G_2(0,y_4) = \frac{\bar{F}(0,y_3)}{2z} = \frac{p_{\mathrm{S}} f(y_3)}{z}. \tag{5.46}$$

Both the solutions are independent of g_{GJ} and $\mathcal{L}_{\mathrm{GJ}}$ and share the same form as Eq. (5.21) for the single neuron with single dendrite model. This result can also be inferred directly from the equivalent cylinders (see §3.3.2).

Different neurons

Now we consider the network consisting of two different neurons. Following the same steps as for the previous case, we obtain the somatic Green's functions for neuron 1,

$$G_1(0, y_2) = \frac{p_{\mathrm{S}_1}}{z_2} f(\mathcal{L}_1 + y_2 - \mathcal{L}_2) \frac{p_{\mathrm{GJ},2} + p_{\mathrm{GJ},2} a_2}{q_{12}}, \tag{5.47a}$$

$$G_1(0, y_1) = \frac{p_{\mathrm{S}_1}}{z_1} f(y_1) \frac{1 - p_{\mathrm{GJ},2} + p_{\mathrm{GJ},1} a_2}{q_{12}}, \tag{5.47b}$$

$$G_1(0, y_4) = \frac{p_{\mathrm{S}_1}}{z_2} \frac{p_{\mathrm{GJ},2}}{q_{12}} \bar{F}_2(y_4, \mathcal{L}_1 + \mathcal{L}_2), \tag{5.47c}$$

$$G_1(0, y_3) = \frac{p_{\mathrm{S}_1}}{z_1} \left[f(y_3) - \frac{p_{\mathrm{GJ},2}}{q_{12}} \bar{F}_1(y_3, 2\mathcal{L}_1) \right], \tag{5.47d}$$

and, symmetrically for neuron 2,

$$G_2(0, y_1) = \frac{p_{\mathrm{S}_2}}{z_1} f(\mathcal{L}_2 + y_1 - \mathcal{L}_1) \frac{p_{\mathrm{GJ},1} + p_{\mathrm{GJ},1} a_1}{q_{12}}, \tag{5.48a}$$

$$G_2(0, y_2) = \frac{p_{\mathrm{S}_2}}{z_2} f(y_2) \frac{1 - p_{\mathrm{GJ},1} + p_{\mathrm{GJ},2} a_1}{q_{12}}, \tag{5.48b}$$

$$G_2(0, y_3) = \frac{p_{\mathrm{S}_2}}{z_1} \frac{p_{\mathrm{GJ},1}}{q_{12}} \bar{F}_1(y_3, \mathcal{L}_1 + \mathcal{L}_2), \tag{5.48c}$$

$$G_2(0, y_4) = \frac{p_{\mathrm{S}_2}}{z_2} \left[f(y_4) - \frac{p_{\mathrm{GJ},1}}{q_{12}} \bar{F}_2(y_4, 2\mathcal{L}_2) \right], \tag{5.48d}$$

where, for $k = 1, 2$,

$$a_k = (2p_{\mathrm{S}_k} - 1) f(2\mathcal{L}_k), \tag{5.49}$$

$$q_{12} = 1 + p_{\mathrm{GJ},2} a_1 + p_{\mathrm{GJ},1} a_2, \tag{5.50}$$

$$\bar{F}_k(x, y) = f(x + y)(2p_{\mathrm{S}_k} - 1) + \frac{f(y)}{f(x)}, \tag{5.51}$$

$$p_{\mathrm{S}_k} = \frac{\gamma_k / r_{a,k}}{N\gamma_k / r_{a,k} + C_{\mathrm{S}_k}\omega + R_{\mathrm{S}_k}^{-1} + (r_{\mathrm{S}_k} + L_{\mathrm{S}_k}\omega)^{-1}}, \tag{5.52}$$

$\gamma_k = \gamma_k(\omega)$ is the characteristic function of the membrane of Cell k, and $\mathcal{L}_k$ is the distance between the gap junction and the soma of Cell k.

Gap junction

Using Eqs. (5.47) and (5.48) we can investigate how the strength and location of the gap junction affect the dynamics of the two-cell model. Here, we consider that

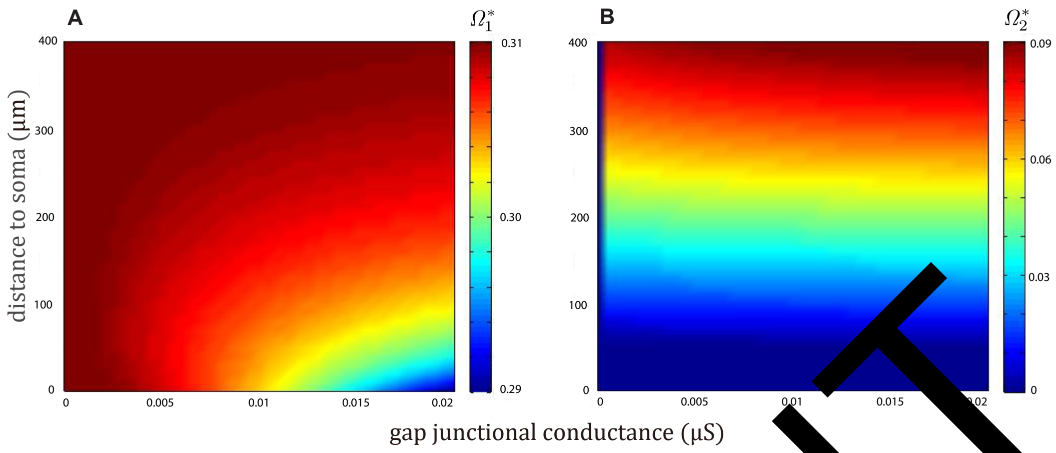

Figure 5.10: The preferred frequencies Ω_1^* and Ω_2^* in the soma of Cell 1 (**A**) and of Cell 2 (**B**). The dendritic parameters of Cell 1 as in Fig. 5.9 except $r_1 = 100\,\Omega\cdot\mathrm{cm}^2$. The dendritic parameters of Cell 2: $a_2 =$ [illegible] μm, $C_2 = 1\,\mu\mathrm{F}\cdot\mathrm{cm}^{-2}$, $R_2 = 20000\,\Omega\cdot\mathrm{cm}^2$, $R_{a,2} = 150\,\Omega\cdot\mathrm{cm}$, and $r_2 \to \infty$ ([illegible] passive dendritic membrane). Both somas are passive.

a stimulus is applied to the soma of Cell 1 and construct a map

$$\Psi : (\mathcal{L}_{\mathrm{GJ}}, g_{\mathrm{GJ}}) \to (\Omega_1^*, \Omega_2^*) \tag{5.53}$$

for the preferred frequencies Ω_1^* and Ω_2^* in the soma of Cell 1 and Cell 2 respectively. This map is shown in Fig. 5.10. In this case Cell 2 is assumed to be purely passive, and Cell 1 has a passive soma with resonant dendrites. The map indicates that the location of a gap junction plays a significant role in the dynamics of the network, unless the coupling is weak. Moreover, the initially passive soma of Cell 2 starts to demonstrate a resonant behaviour imposed by Cell 1 even for weak coupling.

Often it is difficult to measure experimentally locations and strengths of gap junctions in real neuronal networks. Knowledge of the inverse map

$$\Psi^{-1} : (\Omega_1^*, \Omega_2^*) \to (\mathcal{L}_{\mathrm{GJ}}, g_{\mathrm{GJ}}) \tag{5.54}$$

from a pair of preferred frequencies (obtained from somatic sub-threshold stimulations) to $(\mathcal{L}_{\mathrm{GJ}}, g_{\mathrm{GJ}})$ might provide estimates for gap-junctional parameters. However, the map Ψ is neither surjective nor injective (see, for example, Fig. 5.11 for a network of two resonant cells showing that the system may demonstrate the same resonant behaviour for two different gap-junctional locations, proximal and distal, and identical coupling strengths) making it mathematically impractical to obtain Ψ^{-1}. At the same time, if a constraint on locations of gap junctions is imposed

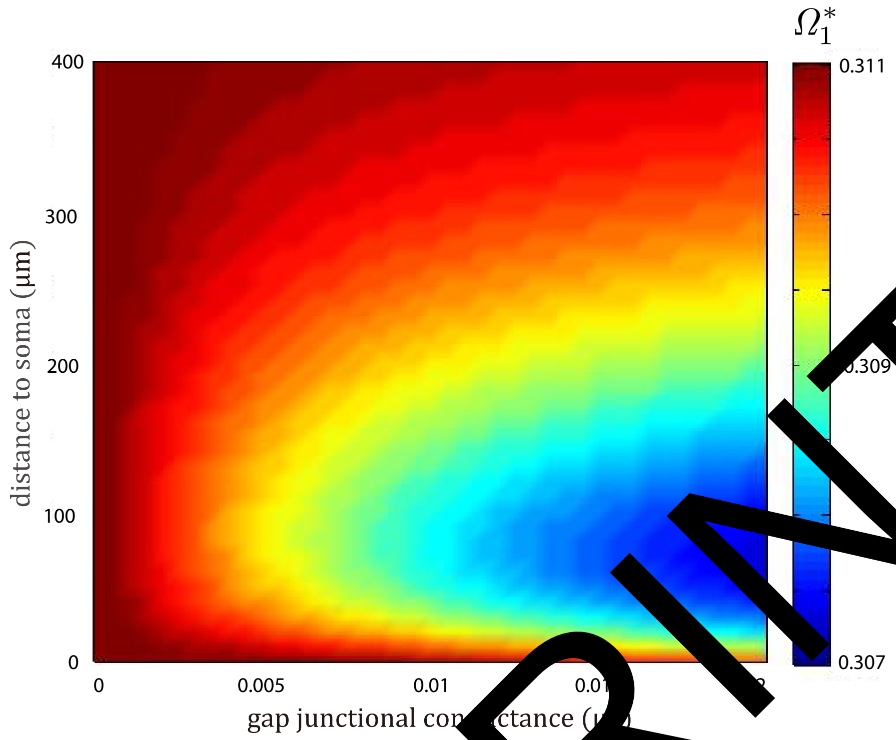

Figure 5.11: The preferred frequency Ω_1^* in soma 1. All parameters are the same as in Fig. 5.10, except $r_2 = 300\,\Omega \cdot \text{cm}^{-1}$.

(e.g., proximal or distal), this may lead to a one-to-one correspondence between $(\mathcal{L}_{\text{GJ}}, g_{\text{GJ}})$ and (Ω_1^*, Ω_2^*) and therefore assists in the estimation of gap-junctional parameters just from the somatic stimulations.

5.2.5 Two tufted neurons coupled by gap junctions

Now we consider a more realistic neuronal network consisting of two identical tufted or mitral cells. Each neuron has a soma attached to N dendritic branches, one of which is the primary dendrite with the tuft spanning from its end. The two cells are coupled via their tufts by dendro-dendritic gap junctions (see Fig. 5.12A). As in the previous model, we assume that the biophysical properties of all dendritic segments are the same and that the physical lengths are scaled by the characteristic function $\gamma(\omega)$. We consider that each cell has n_{T} segments in its tuft, and n_{GJ} of them possess identical single gap-junctional points located l_0 away from the end of the primary dendrite. The primary dendrite of each cell has the length $\mathcal{L}$, while the other branches are semi-infinite. For simplicity, we consider that the membrane of both cells is purely passive (i.e. $\gamma^2(\omega) = (\tau^{-1} + \omega)/D$), however it is straightforward

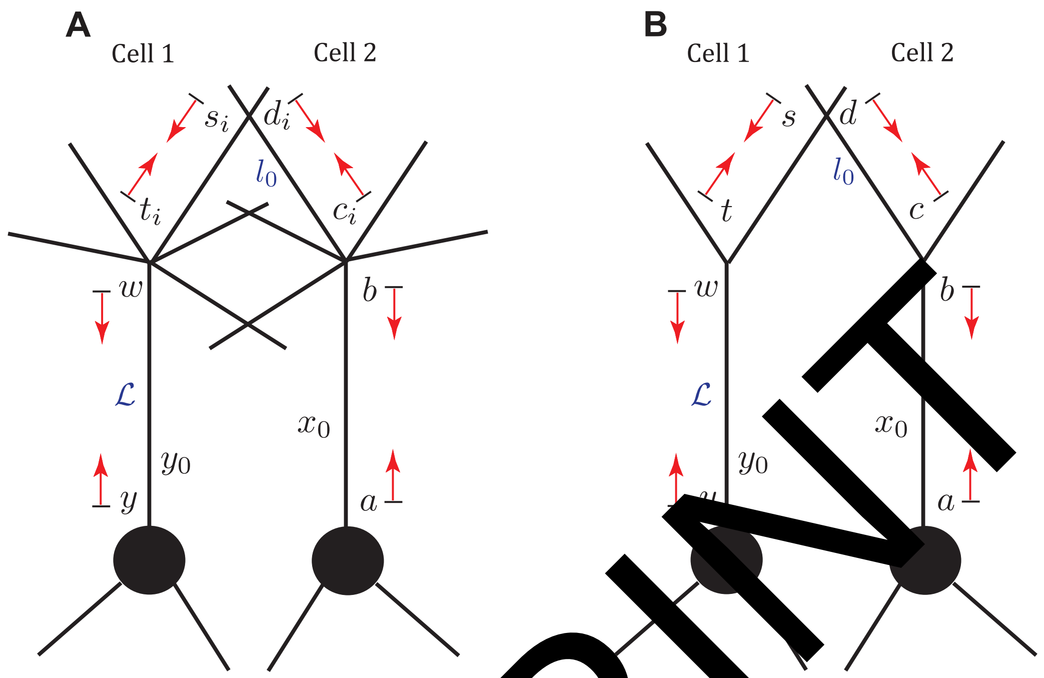

Figure 5.12: **A**: A full two-cell tufted network model. **B**: An equivalent reduced model.

to generalise it for the resonant case.

Model reduction

Although it is possible to use the method of local point matching to construct the Green's functions for this tufted network, it is more convenient to reduce the model by equivalent cylinders (see §3.3.2), which gives the simplified structure shown in Fig. 5.12B. Note that the simplified morphology is the 'Y'-shape neuron we have investigated in §3.3.

To be specific, if the input and output are not located in the tufts, the tufted segments of either the neuron are to merge into two equivalent cylinders, with an equivalent gap junction located on one of them, or explicitly,

$$z^*_{\mathrm{T,GJ}} = n_{\mathrm{GJ}} z_{\mathrm{T}}, \tag{5.55a}$$

$$R^*_{\mathrm{GJ}} = R_{\mathrm{GJ}}/n_{\mathrm{GJ}}, \tag{5.55b}$$

where z_{T} is the impedance of the individual tufted segments, $z^*_{\mathrm{T,GJ}}$ is that of the equivalent cylinder with the gap junction, and $R_{\mathrm{GJ}}, R^*_{\mathrm{GJ}}$ are the gap junctional resistances in the original and simplified models, respectively.

If the input is in the tuft but the output is not, it is easy to check that the constraints (5.55) would give the same J_y, but due to Eq. (3.56), Green's functions are dependent on the input impedance $z_j(y)$. We therefore have

$$G(x_0, y_k) = \frac{1}{n_{\mathrm{T}} - n_{\mathrm{GJ}}} G^*(x_0, y_1), \tag{5.56}$$

for the input y_k applied to the branch without a gap junction, and

$$G(x_0, y_k) = \frac{1}{n_{\mathrm{GJ}}} G^*(x_0, y_2), \tag{5.57}$$

for the input y_k applied to the branch with a gap junction. Here the reduced model is constructed in such a way that the stimuli in the full and reduced models are located at the same distance away from the primary dendrite, i.e. $y_1 = y_k$ and $y_2 = y_k$. The point x_0 ($0 \le x_0 \le \mathcal{L}$) is located on the primary dendrite of either of the cells.

If the output is in the tufts but the input is not, we can use the reciprocity identity (**??**) as we have derived the opposite case. If both the input and output are in the tufts, the symmetry amongst the tufted segments is broken, and thus the model reduction fails. Fortunately, such cases are not of important interests.

By the method of local point matching, the somatic Green's functions to the somatic input in soma 1 can be found as

$$G_2(0,0) = \frac{p_{\mathrm{S}}^2 c_0^2 g_0 t_0 f(\mathcal{L})}{z(1 - 2g_0(c_0 s_0 t_0 + 2n_{\mathrm{GJ}} p_{\mathrm{T}} - 1))}, \tag{5.58a}$$

$$G_1(0,0) = \frac{p_{\mathrm{S}}}{z}(1 + d_0 f(\mathcal{L}))c_0 - G_2(0,0), \tag{5.58b}$$

where $s_0 = f(\mathcal{L})(2p_{\mathrm{S}} - 1)$, $d_0 = f(\mathcal{L})(2p_{\mathrm{D}} - 1)$, $g_0 = p_{\mathrm{GJ}} f(2l_0)$, $t_0 = 2n_{\mathrm{GJ}} p_{\mathrm{T}} p_{\mathrm{D}} f(\mathcal{L})$ and $c_0 = 2/(1 - d_0 s_0)$, with p_{D} contributing to the node factors of travelling into the primary dendrite.

Note that the proof of the model reduction and the derivation of the Green's functions are quite tedious and thus omitted here. All the details can be found in the Appendices in Yihe and Timofeeva [2016].

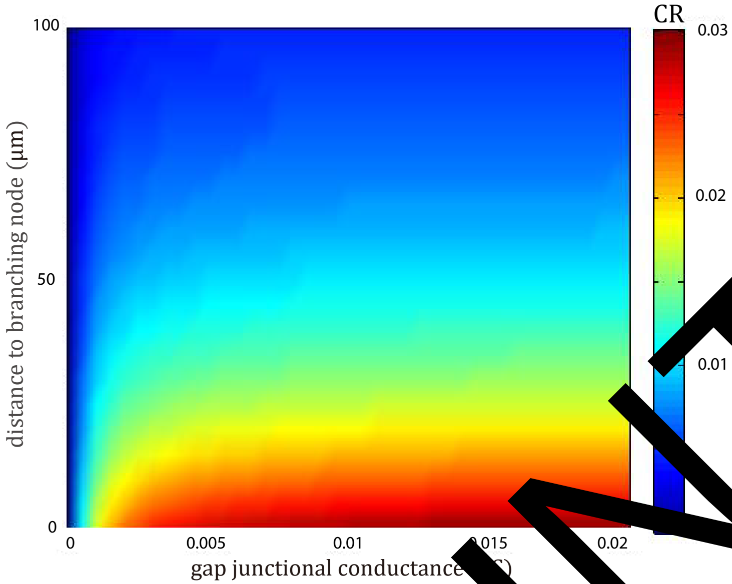

Figure 5.13: Coupling ratio as a function of gap-junctional conductances and distances from the branch point with the primary dendrite. Both cells are identical and passive. Dendritic parameters: $a = 0.4\,\mu\text{m}$, $C = 1\,\mu\text{F}\cdot\text{cm}^{-2}$, $R = 2000\,\Omega\cdot\text{cm}^2$, $R_a = 150\,\Omega\cdot\text{cm}$. Somatic parameters: $r_S = 25\,\mu\text{m}$, $C_{\text{Soma}} = 1\,\mu\text{F}\cdot\text{cm}^{-2}$, $R_{\text{Soma}} = 2000\,\Omega\cdot\text{cm}^2$. The length of the primary dendrite is $\mathcal{L} = 350\,\mu\text{m}$.

Gap junction

For investigating the effect of gap junctions from the tufted regions of the cells on the model's behaviour we define a coupling ratio (CR) as

$$\text{CR} = \frac{\max_t \text{InvLT}\{G_2(0,0;\omega)\}(t)}{\max_t \text{InvLT}\{G_1(0,0;\omega)\}(t)}. \tag{5.59}$$

Using the Green's functions (5.58), we compute and plot in Fig. 5.13 a map of CR for various values of conductance g_{GJ} and location l_0 of the gap junctions in the tuft. This map can be compared with the CR map obtained earlier in Migliore et al. [2005] for two mitral cells coupled by distal gap junctions. Note that the map in Migliore et al. [2005] is obtained by brute-force numerical simulations of a computational model with a similar, but not identical, structure to our two-cell model.

Chapter 6

Conclusion

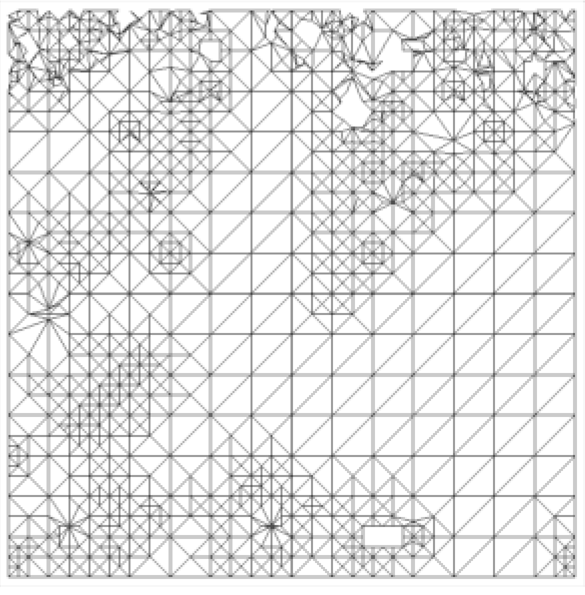

6.1 Summary

In this thesis, we have thorougly studied the dendritic cable theory, which provides us a fundamental framework of understanding the effects on dendritic functions of its structures.

Due to the complex morphology of dendrites, it is non-trivial to find the input-output relationship, even though we simplify the electro-physiological model and assume all cable equations linear. We thus introduce the sum-over-trips framework in Chapter 3, which allows us to write the solutions as the Green's functions in the form of infinite sums. In Chapter 4, we further generalise the original framework from cylindrical dendrites to tapered ones.

The sum-over-trips framework is useful in theory. Without specifying the morphology, we are able to show some general properties of the input-output relationship on dendritic trees, e.g. the reciprocity identity, the condition for equivalent cylinder. However, the computational results do not converge nicely in practice. To overcome this problem, the method of local point scattering is developed, by which we can calculate the compact algebraic expressions for any Green's functions.

Finally, we conduct simulations in Chapter 5, and explicitly investigate different dendritic morphologies. Whereas the structures of the models are simplified, with equivalent cylinders, they are representative for a few classes of neurons.

We have shown that the tapered dendritic strutures are better at tranfering currents from distal to proximal locations than the non-tapered, and the signals are also different in their phases, which could potential cause the two neurons firing at different times and rates. In addition, this property is quite local, that is, the global morphology has little effect (only quantative) on the dendritic segment under investigation.

Since gap junctions allow subthreshold signals to transmit directly between adjacent cells, we can directly investigate its properties in the sum-over-trips framework. A network of two identical neurons and a network of two different neurons are studied. It has been shown possible for us to infer the parameters of a gap junction (mainly its strength and location) by simply stimulating and recording the somata. This is useful because the gap junctions are often so small that their parameters cannot be measured directly in experiments.

6.2 Further works

It has been shown in this thesis that the framework of sum-over-trips and the method of local point matching are powerful tools in analysing and computing responses on morphologically realistic neurons. However, we have explore little into the research field of dendritic physiology (other than electro-physiology), and many important aspects of neuroscience have yet not been considered. Here we point out the natural directions of further work.

Realistic morphology from neuron reconstructions

The framework of sum-over-trips was desgined for realistic morphorlogy [Abbott et al., 1991], but has not become useful in practice, because its solutions are in form of infinite sums and the computational errors cannot be well controlled due to its 'bad' convergence. Nonetheless, the method of local point matching has made accurate and efficient computation possible on complex dendritic morphologies. It will be convenient if a software could be coded up that would read data of neuron reconstructions and automatically compute the Green's functions symbolically. Later simulations will then be able to use these results directly by simply substituting in numerical values of the parameters.

Implications of stochastic cable theory

In reality, randomness can be seen everywhere in the nervous system. Whereas the dendritic morphologies are relatively static in the time scale we are working with, the input and output signals are commonly modelled as stochastic processes. Here we point out the framework of sum-over-trips is perfectly and straightforwardly compatible with the stochastic cable theory [Tuckwell, 2005], because the (deterministic) Green's function obtained by sum-over-trips will be the mean behaviour of the stochastic Green's function, and its variance can be written down directly as well accordingly, if the input as a white noise.

Threshold and non-linear neuronal activities

Threshold behaviours can be conveniently incorporated into the work, because Green's functions are linearly additive. After computing the Green's function, it is trivial to check for some active points if or not their voltages are above the thresholds. Response profiles after the occurance of threshold behaviours have to be updated succesively, but such computational procedure still saves computational

cost as no real computation is required for voltage variations between two threshold behaviours. If the threshold behaviour is a spike that induces changes in synaptic strengths, the processes of learning can be also included in the model.
An alternative approach to deal with active behaviours is to consider the non-linear system directly, e.g. the Hodgkin-Huxley model. Green's functions are originally defined for linear systems and thus they appear not to be useful in neuroscience, where non-linear properties are playing an important role. Nonetheless, it is possible to generalise the the Green's function formalism, and to understand Green's function as a description of input-output relationship. To extend Green's function for non-linear systems, we may want to use the Lippmann-Schwinger equation, which allows us to derive Green's functions functions via an iterative approach [Rotter, 2017].

Emergent behaviours of neural networks

Finally, it is always much more challenging but interesting if we study a network of neurons, especially when the number of the neurons are huge. We would be able to simulate a network of morphological realistic resonant neurons at a lower computational expense for now, and if the results of above further works can also be incorporated, the model can be more realistic in electro-physiology as well as in morphology.

Bibliography

Laurence F Abbott. Simple diagrammatic rules for solving dendritic cable problems. *Physica A: Statistical Mechanics and its Applications*, 185(1-3):343–356, 1992.

Laurence F Abbott, Edward Farhi, and Sam Gutmann. The path integral for dendritic trees. *Biological Cybernetics*, 66(1):49–60, 1991.

Milton Abramowitz and Irene A Stegun. *Handbook of mathematical functions: with formulas, graphs, and mathematical tables*, volume 55. Dover Corporation, 1964.

Giorgio A Ascoli. *Computational neuroanatomy: Principles and methods*. Springer Science & Business Media, 2002.

Giorgio A Ascoli, Duncan E Donohue, and Maryam Halavi. Neuromorpho. org: a central resource for neuronal morphologies. *Journal of Neuroscience*, 27(35): 9247–9251, 2007.

Steven M Baer and John Rinzel. Propagation of dendritic spikes mediated by excitable spines: a continuum theory. *Journal of Neurophysiology*, 65(4):874–890, 1991.

William P Bartlett and Gary A Banker. An electron microscopic study of the development of axons and dendrites by hippocampal neurons in culture. i. cells which develop without intercellular contacts. *Journal of Neuroscience*, 4(8):1944–1953, 1984.

Guo-qiang Bi and Mu-ming Poo. Synaptic modification by correlated activity: Hebb's postulate revisited. *Annual Review of Neuroscience*, 24(1):139–166, 2001.

Alex D Bird and Hermann Cuntz. Optimal current transfer in dendrites. *PLoS computational biology*, 12(5):e1004897, 2016.

Tobias Bonhoeffer and Rafael Yuste. Spine motility: phenomenology, mechanisms, and function. *Neuron*, 35(6):1019–1027, 2002.

Paul C Bressloff and Stephen Coombes. Solitary waves in a model of dendritic cable with active spines. *SIAM Journal on Applied Mathematics*, 61(2):432–453, 2000.

Lowell S Brown and Yan Zhang. Path integral for the motion of a particle in a linear potential. *American Journal of Physics*, 62(9):806–808, 1994.

Heather A Cameron and Ronald DG Mckay. Adult neurogenesis produces a large pool of new granule cells in the dentate gyrus. *Journal of Comparative Neurology*, 435(4):406–417, 2001.

Bulin J Cao and Laurence F Abbott. A new computational method for cable theory problems. *Biophysical Journal*, 64(2):303–313, 1993.

Joseph J Capowski. An automatic neuron reconstruction system. *Journal of Neuroscience Methods*, 8(4):353–364, 1983.

Joseph J Capowski. *Computer techniques in neuroanatomy*. Springer Science & Business Media, 2012.

Joseph J Capowski and Mathius J Sedivec. Accurate computer reconstruction and graphics display of complex neurons utilizing state-of-the-art interactive techniques. *Computers and Biomedical Research*, 14(6):518–532, 1981.

Nicholas T Carnevale and Michael L Hines. *The NEURON book*. Cambridge University Press, 2006.

Quentin Caudron. *Neuronal computation on complex dendritic morphologies*. PhD thesis, University of Warwick, 2012.

Quentin Caudron, Simon R Donnelly, Samuel PC Brand, and Yulia Timofeeva. Computational convergence of the path integral for real dendritic morphologies. *The Journal of Mathematical Neuroscience*, 2(1):11, 2012.

Christopher Cherniak, Mark Changizi, and Du Won Kang. Large-scale optimization of neuron arbors. *Physical Review E*, 59(5):6001, 1999.

John D Clements and Stephan J Redman. Cable properties of cat spinal motoneurones measured by combining voltage clamp, current clamp and intracellular staining. *The Journal of Physiology*, 409(1):63–87, 1989.

Susanne D Coates. Neural interfacing: Forging the human-machine connection. *Synthesis Lectures on Biomedical Engineering*, 3(1):1–112, 2008.

Stephen Coombes and Áine Byrne. Next generation neural mass models. *arXiv preprint arXiv:1607.06251*, 2016.

Stephen Coombes, Yulia Timofeeva, Carl-Magnus Svensson, Gabriel J Lord, Krešimir Josić, Steven J Cox, and Costa M Colbert. Branching dendrites with resonant membrane: a "sum-over-trips" approach. *Biological Cybernetics*, 97(2): 137–149, 2007.

Hermann Cuntz, Alexander Borst, and Idan Segev. Optimization principles of dendritic structure. *Theoretical Biology & Medical modelling*, 4:21–21, 2007.

Peter Dayan and Laurence F Abbott. *Theoretical neuroscience*, volume 806. Cambridge, MA: MIT Press, 2001.

Isha Schwaller De Lubicz. *Her-Bak, Egyptian Initiate*. Inner Traditions International, 1978.

Raymond A DeCarlo and Pen-Min Lin. *Linear circuit analysis: time domain, phasor, and Laplace transform approaches*. Prentice-Hall, Inc., 1995.

Ekrem Dere, editor. *Gap junctions in the brain: physiological and pathological roles*. Academic Press, 2012.

Nancy L Desmond and William B Levy. Dendritic caliber and the 3/2 power relationship of dentate granule cells. *Journal of Comparative Neurology*, 227(4): 589–596, 1984.

Stanley Finger. *Origins of neuroscience: a history of explorations into brain function*. Oxford University Press, USA, 2001.

Thomas S Ford-Holevinski, Todd A Dahlberg, and Bernard W Agranoff. A microcomputer-based image analyzer for quantitating neurite outgrowth. *Brain research*, 368(2):339–346, 1986.

Wolfram Gerstner and Werner Kistler. *Spiking Neuron Models Cambridge University Press*. Cambridge, 2002.

Edmund M Glaser and H F Machiel Van der Loos. A semi-automatic computer-microscope for the analysis of neuronal morphology. *IEEE Transactions on Biomedical Engineering*, (1):22–31, 1965.

Steven S Goldstein and Wilfrid Rall. Changes of action potential shape and velocity for changing core conductor geometry. *Biophysical Journal*, 14(10):731–757, 1974.

Gilbert Harman. Thought. princeton. *NJ: Princeton University*, 1973.

Donald Olding Hebb. *The organization of behavior: A neuropsychological theory*. Psychology Press, 2005.

Terry F Hoad, editor. *The concise Oxford dictionary of English etymology*. Oxford University Press Oxford, 1993.

Alan L Hodgkin and Andrew F Huxley. A quantitative description of membrane current and its application to conduction and excitation in nerve. *The Journal of Physiology*, 117(4):500–544, 1952.

John J Hopfield. Neural networks and physical systems with emergent collective computational abilities. *Proceedings of the National Academy of Sciences*, 79(8): 2554–2558, 1982.

Eugene M Izhikevich and Gerald M Edelman. Large-scale model of mammalian thalamocortical systems. *Proceedings of the National Academy of Sciences*, 105 (9):3593–3598, 2008.

James Julian Bennett Jack, Denis Noble, and Richard W Tsien. *Electric current flow in excitable cells*. Clarendon Press Oxford, 1975.

Christof Koch. Cable theory in neurons with active, linearized membranes. *Biological Cybernetics*, 50(1):15–33, 1984.

Christof Koch, Tomaso Poggio, and Vincent Torre. Nonlinear interactions in a dendritic tree: localization, timing, and role in information processing. *Proceedings of the National Academy of Sciences*, 80(9):2799–2802, 1983.

Yoshiyuki Kubota, Fuyuki Karube, Masaki Nomura, Allan T Gulledge, Atsushi Mochizuki, Andreas Schertel, and Yasuo Kawaguchi. Conserved properties of dendritic trees in four cortical interneuron subtypes. *Scientific Reports*, 1:89, 2011.

Helen C Lai and Lily Y Jan. The distribution and targeting of neuronal voltage-gated ion channels. *Nature Reviews Neuroscience*, 7(7), 2006.

Peter E Latham, BJ Richmond, PG Nelson, and S Nirenberg. Intrinsic dynamics in neuronal networks. i. theory. *Journal of Neurophysiology*, 83(2):808–827, 2000.

Kenneth A Lindsay, Jay R Rosenberg, and G Tucker. From maxwell's equations to the cable equation and beyond. *Progress in Biophysics & Molecular Biology*, 85 (1):71–116, 2004.

Graeme Lowe. Inhibition of backpropagating action potentials in mitral cell secondary dendrites. *Journal of Neurophysiology*, 88(1):64–85, 2002.

Zachary F Mainen and Terrence J Sejnowski. Influence of dendritic structure on firing pattern in model neocortical neurons. *Nature*, 382(6589):363, 1996.

Henry Markram. The blue brain project. *Nature Reviews Neuroscience*, 7(2):153–160, 2006.

Warren S McCulloch and Walter Pitts. A logical calculus of the ideas immanent in nervous activity. *The Bulletin of Mathematical Biophysics*, 5(4):115–133, 1943.

Erik Meijering. Neuron tracing in perspective. *Cytometry Part A*, 77(7):693–704, 2010.

Bartlett W Mel. Information processing in dendritic trees. *Neural Computation*, 6 (6):1031–1085, 1994.

Michele Migliore, Michael L Hines, and Gordon M Shepherd. The role of distal dendritic gap junctions in synchronization of mitral cell axonal output. *Journal of Computational Neuroscience*, 18(2):151–161, 2005.

Brian T Park and Vahe Petrosian. Fokker-planck equations of stochastic acceleration: Green's functions and boundary conditions. *The Astrophysical Journal*, 446: 699, 1995.

Hanchuan Peng, Fuhui Long, Ting Zhao, and Eugene Myers. Proof-editing is the bottleneck of 3d neuron reconstruction: the problem and solutions. *Neuroinformatics*, 9(2-3):103–105, 2011.

Roman R Poznanski. A generalized tapering equivalent cable model for dendritic neurons. *Bulletin of Mathematical Biology*, 53(3):457–467, 1991.

Wilfrid Rall. Theory of physiological properties of dendrites. *Annals of the New York Academy of Sciences*, 96(1):1071–1092, 1962.

Wilfrid Rall. Distinguishing theoretical synaptic potentials computed for different soma-dendritic distributions of synaptic input. *Journal of Neurophysiology*, 30(5): 1138–1168, 1967.

Wilfrid Rall. Distributions of potential in cylindrical coordinates and time constants for a membrane cylinder. *Biophysical Journal*, 9(12):1509–1541, 1969.

Santiago Ramón y Cajal. *Significación fisiológica de las expansiones protoplásmicas y nerviosas de las células de la sustancia gris.* 1891.

Magnus JE Richardson. Introduction to theoretical neuroscience (lecture notes). URL: `https://warwick.ac.uk/fac/sci/systemsbiology/staff/richardson/teaching/ma4g4/ITN_LN1.pdf`. Last visited on 2017/12/16.

Juan M Romero and Carlos Trenado. Analytical solution of a tapering cable equation for dendrites and conformal symmetry. *Biophysical Reviews and Letters*, 10(03): 175–185, 2015.

Tom Rother. *Green's Functions in Classical Physics*, volume 938. Springer, 2017.

Michael A Schwemmer and Timothy J Lewis. Bistability in a leaky integrate-and-fire neuron with a passive dendrite. *SIAM Journal on Applied Dynamical Systems*, 11(1):507–539, 2012.

Idan Segev, John Rinzel, and GM Shepherd, editors. *The theoretical foundation of dendritic function: selected papers of Wilfrid Rall with commentaries.* MIT press, 1995.

Dd A Sholl. Dendritic organization in the neurons of the visual and motor cortices of the cat. *Journal of Anatomy*, 87(Pt 4):387, 1953.

Goran Söhl, Stephan Maxeiner, and Klaus Willecke. Expression and functions of neuronal gap junctions. *Nature Reviews Neuroscience*, 6(3):191, 2005.

Herbert Spencer. *The Principles Of Biology, Vol. 2.* Willium And Norgate, London, 1884.

Ivar Stakgold and Michael J Holst. *Green's functions and boundary value problems*, volume 99. John Wiley & Sons, 2011.

George M Strain and William H Brockman. A modified cable model for neuron processes with non-constant diameters. *Journal of Theoretical Biology*, 51(2): 475–494, 1975.

Greg Stuart, Nelson Spruston, and Michael Häusser, editors. *Dendrites.* Oxford University Press, 2016.

Yulia Timofeeva and Stephen Coombes. *The Computing Dendrite: From Structure to Function*, chapter Network response of gap junction coupled dendrites, pages 449–464. Springer, 2014.

Yulia Timofeeva, Stephen Coombes, and Davide Michieletto. Gap junctions, dendrites and resonances: a recipe for tuning network dynamics. *The Journal of Mathematical Neuroscience*, 3(1):15, 2013.

Gin-yih Tsaur and Jyhpyng Wang. Constructing green functions of the schrödinger equation by elementary transformations. *American Journal of Physics*, 74(7): 600–606, 2006.

Henry C Tuckwell. *Introduction to theoretical neurobiology: volume 2, nonlinear and stochastic theories*, volume 8. Cambridge University Press, 2005.

Josef Turecek, Genevieve S Yuen, Victor Z Han, Xiao-Hui Zeng, K Ulrich Bayer, and John P Welsh. Nmda receptor activation strengthens weak electrical coupling in mammalian brain. *Neuron*, 81(6):1375–1388, 2014.

Olivier Vallée and Manuel Soares. *Airy functions and applications to physics*. World Scientific Publishing Company, 2010.

Philipp Vetter, Arnd Roth, and Michael Häusser. Propagation of action potentials in dendrites depends on dendritic morphology. *Journal of Neurophysiology*, 85(2): 926–937, 2001.

Alison S Walker, Guilherme Neves, Federico Grillo, Rachel E Jackson, Mark Rigby, Cian ODonnell, Andrew S Lowe, Gema Vizcay-Barrena, Roland A Fleck, and Juan Burrone. Distance-dependent gradient in nmdar-driven spine calcium signals along tapering dendrites. *Proceedings of the National Academy of Sciences*, page 201607462, 2017.

Charles J Wilson and Joseph C Callaway. Coupled oscillator model of the dopaminergic neuron of the substantia nigra. *Journal of Neurophysiology*, 83(5):3084–3100, 2000.

Lu Yihe and Yulia Timofeeva. Response functions for electrically coupled neuronal network: a method of local point matching and its applications. *Biological Cybernetics*, 110(2-3):117–133, 2016.